

AD-A147 560

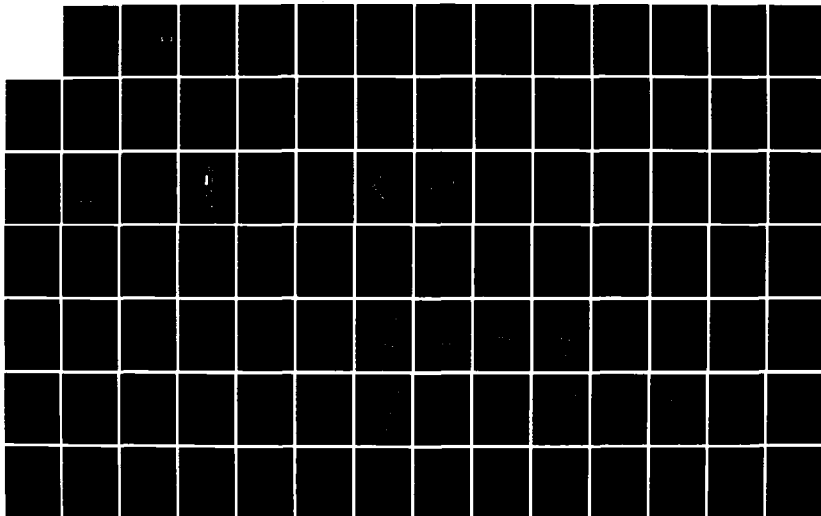
PION INELASTIC SCATTERING TO THE FIRST THREE EXCITED
STATES OF LITHIUM-6(U) AIR FORCE INST OF TECH
WRIGHT-PATTERSON AFB OH R R KIZIAH DEC 84
AFIT/CI/NR-84-85D

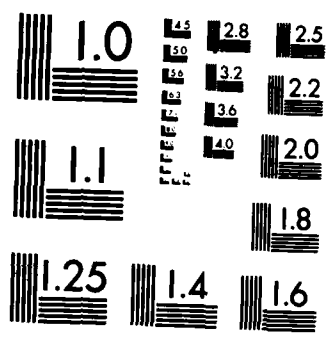
1/2

UNCLASSIFIED

F/G 20/8

NL





UNCLASS

SECURITY CLASSIFICATION OF THIS PAGE (When Data Entered)

REPORT DOCUMENTATION PAGE

READ INSTRUCTIONS
BEFORE COMPLETING FORM

1. REPORT NUMBER

2. GOVT ACCESSION NO.

3. RECIPIENT'S CATALOG NUMBER

AFIT/CI/NR 84-85D

4. TITLE (and Subtitle)

Pion Inelastic Scattering To The First
Three Excited States Of Lithium-6

5. TYPE OF REPORT & PERIOD COVERED

/THESIS/DISSERTATION

6. PERFORMING ORG. REPORT NUMBER

7. AUTHOR(s)

Rex Paymond Kiziah

8. CONTRACT OR GRANT NUMBER(s)

9. PERFORMING ORGANIZATION NAME AND ADDRESS

AFIT STUDENT AT: The University of Texas
at Austin10. PROGRAM ELEMENT, PROJECT, TASK
AREA & WORK UNIT NUMBERS

11. CONTROLLING OFFICE NAME AND ADDRESS

AFIT/NR
WPAFB OH 45433

12. REPORT DATE

Dec 1984

13. NUMBER OF PAGES

175

14. MONITORING AGENCY NAME & ADDRESS (if different from Controlling Office)

15. SECURITY CLASS. (of this report)

UNCLASS

15a. DECLASSIFICATION/DOWNGRADING
SCHEDULE

16. DISTRIBUTION STATEMENT (of this Report)

APPROVED FOR PUBLIC RELEASE; DISTRIBUTION UNLIMITED

DTIC
ELECTE
NOV 19 1984

17. DISTRIBUTION STATEMENT (of the abstract entered in Block 20, if different from Report)

B

18. SUPPLEMENTARY NOTES

APPROVED FOR PUBLIC RELEASE: IAW AFR 190-1

LYNN E. WOLAVER
Dean for Research and
Professional Development
AFIT, Wright-Patterson AFB OH

19. KEY WORDS (Continue on reverse side if necessary and identify by block number)

20. ABSTRACT (Continue on reverse side if necessary and identify by block number)

ATTACHED

84 11 14 145

DD FORM 1473

EDITION OF 1 NOV 65 IS OBSOLETE

UNCLASS

SECURITY CLASSIFICATION OF THIS PAGE (When Data Entered)

AD-A147 560

DTIC FILE COPY

adequately reproduce the measured angular distributions for the 3.563-MeV level and fail to reproduce the observed anomalous excitation function. The shape of the 3.563-MeV excitation function is similar to that previously observed for π^+ inelastic scattering to the 1^+ , T=1, 15.11-MeV state of ^{12}C . The same mechanism may be responsible for the observed excitation functions of both $\Delta S=\Delta T=1$ transitions. A possible mechanism is the direct excitation of Δ particle-nucleon hole (Δ -h) components in the final state wave functions. Within the Δ -h model interpretation, the peak of the 3.563-MeV excitation function is reproduced with an estimated probability amplitude for the Δ -h component of the 3.563-MeV state with respect to the ground state of $0.01 < B < 0.13$, a range of values of B consistent with the range estimated for the 15.11-MeV level of ^{12}C ($0.026 < B < 0.096$).



Accession For	
NTIS GRA&I	<input checked="" type="checkbox"/>
DTIC TAB	<input type="checkbox"/>
Unannounced	<input type="checkbox"/>
Justification	
By	
Distribution/	
Availability Codes	
Dist	Special
A-1	

PION INELASTIC SCATTERING TO THE FIRST THREE
EXCITED STATES OF LITHIUM-6

Publication No. _____

Rex Raymond Kiziah, Ph.D.
The University of Texas at Austin, 1984

Supervising Professor: C. Fred Moore

π^+
Using the Energetic Pion Channel and Spectrometer system at the Clinton P. Anderson Meson Physics Facility, differential cross sections were measured for π^+ inelastic scattering to the 3^+ , $T=0$, 2.185-MeV, 0^+ , $T=1$, 3.563-MeV, and 1^+ , $T=0$, 4.25-MeV states of ${}^6\text{Li}$ at incident pion energies of 120 and 180 MeV and laboratory scattering angles between 15° and 47° . Excitation functions were measured at a constant momentum transfer of approximately 109 MeV/c for incident pion energies from 100 to 260 MeV. The constant momentum transfer corresponds to the maxima of the angular distributions for π^+ inelastic scattering to the 3.563-MeV level. Microscopic calculations using the distorted-wave impulse approximation (DWIA) agree well with the measured angular distributions and excitation functions for the 2.185- and 4.25-MeV levels. However, microscopic DWIA calculations do not

AFIT RESEARCH ASSESSMENT

The purpose of this questionnaire is to ascertain the value and/or contribution of research accomplished by students or faculty of the Air Force Institute of Technology (AU). It would be greatly appreciated if you would complete the following questionnaire and return it to:

AFIT/NR
Wright-Patterson AFB OH 45433

RESEARCH TITLE: Pion Inelastic Scattering To The First Three Excited States of Lithium-6

AUTHOR: Rex Raymond Kiziah

RESEARCH ASSESSMENT QUESTIONS:

1. Did this research contribute to a current Air Force project?

☐ a. YES

☐ b. NO

2. Do you believe this research topic is significant enough that it would have been researched (or contracted) by your organization or another agency if AFIT had not?

☐ a. YES

☐ b. NO

3. The benefits of AFIT research can often be expressed by the equivalent value that your agency achieved/received by virtue of AFIT performing the research. Can you estimate what this research would have cost if it had been accomplished under contract or if it had been done in-house in terms of manpower and/or dollars?

☐ a. MAN-YEARS _____

☐ b. \$ _____

4. Often it is not possible to attach equivalent dollar values to research, although the results of the research may, in fact, be important. Whether or not you were able to establish an equivalent value for this research (3. above), what is your estimate of its significance?

☐ a. HIGHLY
SIGNIFICANT

☐ b. SIGNIFICANT

☐ c. SLIGHTLY
SIGNIFICANT

☐ d. OF NO
SIGNIFICANCE

5. AFIT welcomes any further comments you may have on the above questions, or any additional details concerning the current application, future potential, or other value of this research. Please use the bottom part of this questionnaire for your statement(s).

NAME _____ GRADE _____ POSITION _____

ORGANIZATION _____ LOCATION _____

STATEMENT(s):

PION INELASTIC SCATTERING TO THE FIRST THREE
EXCITED STATES OF LITHIUM-6

by

Rex Raymond Kiziah, B.S.

DISSERTATION

Presented to the Faculty of the Graduate School of
The University of Texas at Austin
in Partial Fulfillment
of the Requirements
for the Degree of

DOCTOR OF PHILOSOPHY

THE UNIVERSITY OF TEXAS AT AUSTIN

(December 1984)

ACKNOWLEDGEMENTS

First, I thank my advisor, Professor C. Fred Moore, for his help and support during my years as his graduate student. Special thanks go to Dr. William B. Cottingame for allowing me to use his proposed experiment for my dissertation and for his constant help and discussions throughout the taking of the data, the analysis of the data, and preparation of the paper submitted to Phys. Rev. C. Also, I thank Dr. William Cottingame for carefully reading parts of this dissertation. I thank all the collaborators on the experiment: Mark Brown, Dr. Carol Harvey, David Oakley, David Saunders, Peter Seidl, Professor C. Fred Moore, Dr. William Cottingame, Robert Garnett, Dr. Steven Greene, Dr. German Luna, Professor George Burleson, and Dr. David Holtkamp. I also thank Dr. Richard L. Boudrie and the MP10 Staff for their helpful expertise in the tuning, operation, and maintenance of the EPICS system. Special thanks go to my brother, Todd Kiziah, for helping with the fitting of many of the spectra. I deeply appreciate the many helpful and enjoyable discussions with Peter Seidl and his careful reading of this dissertation. Special thanks go to Dr. Richard Joseph and Shelly Joseph for the many enjoyable evenings spent at their home and the use of their cars on many occasions. Lastly, I thank Lt. Col. John I. Kitch for his help in convincing the Air Force to allow me the time to obtain my Ph.D. and for his help with all Air Force matters during my graduate student years.

PION INELASTIC SCATTERING TO THE FIRST THREE
EXCITED STATES OF LITHIUM-6

Publication No. _____

Rex Raymond Kiziah, Ph.D.
The University of Texas at Austin, 1984

Supervising Professor: C. Fred Moore

Using the Energetic Pion Channel and Spectrometer system at the Clinton P. Anderson Meson Physics Facility, differential cross sections were measured for π^+ inelastic scattering to the 3^+ , $T=0$, 2.185-MeV, 0^+ , $T=1$, 3.563-MeV, and 2^+ , $T=0$, 4.25-MeV states of ${}^6\text{Li}$ at incident pion energies of 120 and 180 MeV and laboratory scattering angles between 15° and 47° . Excitation functions were measured at a constant momentum transfer of approximately 109 MeV/c for incident pion energies from 100 to 260 MeV. The constant momentum transfer corresponds to the maxima of the angular distributions for π^+ inelastic scattering to the 3.563-MeV level. Microscopic calculations using the distorted-wave impulse approximation (DWIA) agree well with the measured angular distributions and excitation functions for the 2.185- and 4.25-MeV levels. However, microscopic DWIA calculations do not

adequately reproduce the measured angular distributions for the 3.563-MeV level and fail to reproduce the observed anomalous excitation function. The shape of the 3.563-MeV excitation function is similar to that previously observed for π^+ inelastic scattering to the 1^+ , $T=1$, 15.11-MeV state of ^{12}C . The same mechanism may be responsible for the observed excitation functions of both $\Delta S=\Delta T=1$ transitions. A possible mechanism is the direct excitation of Δ particle-nucleon hole (Δ -h) components in the final state wave functions. Within the Δ -h model interpretation, the peak of the 3.563-MeV excitation function is reproduced with an estimated probability amplitude for the Δ -h component of the 3.563-MeV state with respect to the ground state of $0.01 < \beta < 0.13$, a range of values of β consistent with the range estimated for the 15.11-MeV level of ^{12}C ($0.026 < \beta < 0.096$).

TABLE OF CONTENTS

LIST OF TABLES	vii
LIST OF FIGURES	viii
I. INTRODUCTION	1
II. EXPERIMENTAL APPARATUS AND PROCEDURE	13
A. EPICS system	13
B. Detector system and beam monitoring	21
C. Data acquisition and analysis system	26
D. Event analysis	30
III. DATA REDUCTION AND RESULTS	37
A. Missing mass histograms and targets	37
B. Extraction of peak areas	40
C. Cross section computation and errors	51
D. Data	56
IV. THEORY	68
A. Nonrelativistic multiple-scattering formalism	69
B. Elastic scattering	73
C. Inelastic scattering	84
V. COMPARISON OF THEORY AND DATA	95
A. Elastic scattering	95
B. Inelastic scattering	99
1. 3^+ , $T=0$, 2.185-MeV state	100
2. 2^+ , $T=0$, 4.25-MeV state	105
3. 0^+ , $T=1$, 3.563-MeV state	108
C. Discussion and results	114
VI. SUMMARY	123
APPENDIX A Data Tabulation	125
APPENDIX B Estimation of β	129
APPENDIX C Dissertation Paper	132
REFERENCES	168

LIST OF TABLES

II-1: EPICS system specifications.	17
II-2: EPICS channel beam pion flux and composition.	17

LIST OF FIGURES

I-1:	Total cross sections for π^+p , π^-p , and pp scattering as a function of lab kinetic energy T_π .	3
I-2:	Ratio of four times the differential cross sections for π^\pm inelastic scattering to the 1^+ , $T=1$, 15.11-MeV state of ^{12}C and the differential cross sections for π^\pm inelastic scattering to the 1^+ , $T=0$, 12.71-MeV state of ^{12}C .	11
II-1:	Experimental Area A of the LAMPF facility.	14
II-2:	The Energetic Pion Channel and Spectrometer (EPICS) at LAMPF.	16
II-3:	The EPICS channel and its optical mode.	19
II-4:	The EPICS spectrometer.	20
II-5:	The EPICS spectrometer optics and the detector system.	22
II-6:	Block diagram of the electronics for the EPICS data acquisition system.	28
II-7:	Sample test file.	31
III-1:	π^+ energy-loss spectrum taken at $T_\pi = 140$ MeV and $\theta_{\text{lab}} = 26^\circ$.	38
III-2:	π^+ energy-loss spectra taken at $T_\pi = 120$ MeV and $\theta_{\text{lab}} = 27^\circ$.	44
III-3:	π^+ energy-loss spectra and fits using the computer	

program LOAF.	46
III-4: Angular distributions for 100 keV wide segments of background centered about 3.563 MeV.	47
III-5: Angular distributions for 100 keV wide segments of background centered about 4.25 MeV.	48
III-6: Background yields versus incident pion energy for 100 keV wide segments of background centered about 3.563 MeV.	49
III-7: Background yields versus incident pion energy for 100 keV wide segments of background centered about 4.25 MeV.	50
III-8: Differential cross sections for π^+ elastic scattering for ${}^6\text{Li}$ for $T_\pi = 120$ and 180 MeV.	57
III-9: Differential cross sections for π^+ elastic scattering for ${}^6\text{Li}$ at a constant $q \approx 109$ MeV/c.	58
III-10: Angular distributions for π^+ inelastic scattering to the 3^+ , $T=0$, 2.185-MeV state of ${}^6\text{Li}$ for $T_\pi = 120$ and 180 MeV.	60
III-11: Differential cross sections for π^+ inelastic scattering to the 3^+ , $T=0$, 2.185-MeV state of ${}^6\text{Li}$ at a constant $q \approx 109$ MeV/c.	61
III-12: Angular distributions for π^+ inelastic scattering to the 2^+ , $T=0$, 4.25-MeV state of ${}^6\text{Li}$ for $T_\pi = 120$ and 180 MeV.	63
III-13: Differential cross sections for π^+ inelastic scattering to the 2^+ , $T=0$, 4.25-MeV state of ${}^6\text{Li}$ at $q \approx 109$ MeV/c.	64

III-14:	Angular distributions for π^+ inelastic scattering to the 0^+ , $T=1$, 3.563-MeV state of ${}^6\text{Li}$ for $T_\pi = 120$ and 180 MeV.	65
III-15:	Excitation function at a constant $q \approx 109$ MeV/c for π^+ inelastic scattering to the 0^+ , $T=1$, 3.563-MeV state of ${}^6\text{Li}$.	66
V-1:	Differential cross sections and elastic calculations for π^+ and π^- elastic scattering for ${}^6\text{Li}$ for $T_\pi = 120, 164$, and 180 MeV.	97
V-2:	Differential cross sections and elastic calculations for π^+ elastic scattering for ${}^6\text{Li}$ at a constant $q \approx 109$ MeV/c.	98
V-3:	$ F_L(q) ^2$ and calculations for the 3^+ , $T=0$, 2.185-MeV state of ${}^6\text{Li}$.	102
V-4:	Angular distributions and DWIA calculations for π^+ inelastic scattering to the 3^+ , $T=0$, 2.185-MeV state of ${}^6\text{Li}$ for $T_\pi = 120$ and 180 MeV.	103
V-5:	Differential cross sections and DWIA calculations for π^+ inelastic scattering to the 3^+ , $T=0$, 2.185-MeV state of ${}^6\text{Li}$ at a constant $q \approx 109$ MeV/c.	104
V-6:	Angular distributions and DWIA calculations for π^+ inelastic scattering to the 2^+ , $T=0$, 4.25-MeV state of ${}^6\text{Li}$ for $T_\pi = 120$ and 180 MeV.	106
V-7:	Differential cross sections and DWIA calculations for π^+ inelastic scattering to the 2^+ , $T=0$, 4.25-MeV state of ${}^6\text{Li}$ at $q \approx 109$ MeV/c.	107
V-8:	$ F_T(q) ^2$ and calculations for the 0^+ , $T=1$, 3.563-MeV state of ${}^6\text{Li}$.	110

V-9:	Angular distributions and DWIA calculations for π^+ inelastic scattering to the 0^+ , $T=1$, 3.563-MeV state of ${}^6\text{Li}$ for $T_\pi = 120$ and 180 MeV.	112
V-10:	Excitation function and DWIA calculations at a constant $q = 109$ MeV/c for π^+ inelastic scattering to the 0^+ , $T=1$, 3.563-MeV state of ${}^6\text{Li}$.	113
V-11:	Excitation functions and DWIA calculations at a constant $q = 124$ MeV/c for pion inelastic scattering to the 1^+ , $T=0$, 12.71-MeV and 1^+ , $T=1$, 15.11-MeV states of ${}^{12}\text{C}$.	116
V-12:	Ratio of the experimental differential cross sections to the calculated differential cross sections for the excitation functions of the two $\Delta S=\Delta T=1$ transitions to the 3.563-MeV state of ${}^6\text{Li}$ and the 15.11-MeV state of ${}^{12}\text{C}$.	119
V-13:	Schematic representation of the direct excitation of Δ -h components of the excited nuclear state wave function.	121

I. INTRODUCTION

Since the prediction of the pion by Yukawa [Yu-35] in 1935 and its production in the University of California Radiation Laboratory by Gardner and Lattes in 1948, there has been extensive theoretical and experimental work with the pion as a probe of nuclear structure. Such extensive work was possible and is continuing due to the construction and subsequent operation of three meson production facilities: the Los Alamos Meson Physics Facility (LAMPF) in the United States, the Swiss Institute for Nuclear Research (SIN) in Switzerland, and the Tri-University Meson Facility (TRIUMF) in Canada. LAMPF is the highest intensity meson production facility. However, all three facilities were constructed to produce high energy resolution secondary beams of pions required in the study of closely spaced (< 1 MeV separation) excited levels of nuclei with sometimes extremely small pion-induced inelastic scattering cross sections.

The pion is a pseudoscalar, $J^{\pi}=0^{-}$, isovector, $T=1$, meson and is the lightest known strongly interacting particle ($m_{\pi} = 139.6$ MeV). As a field quantum of the nuclear force, the pion is responsible for the long-range part of the hadronic potential. Many of the pion's properties make it an extremely useful hadronic probe due to resulting theoretical simplifications in the analysis of pion-nucleus scattering data, and the ability to perform experiments with the pion which complement those using other hadronic and electromagnetic probes or which cannot be done with any other probe: (1) There are three charge states of the pion, π^{+} , π^{0} ,

and π^- ; thus, one can use the pion for elastic scattering, single-charge-exchange (SCX) scattering, and double-charge-exchange (DCX) scattering. The latter process can lead to nuclear levels with T , T_z values not obtainable with a $T=1/2$ hadronic probe such as the proton. (2) The pion possesses spin zero. As a boson, it can be absorbed by clusters of nucleons in the nucleus, and pion absorption experiments may therefore provide useful information about nucleon correlations within the nucleus. Furthermore, the pion's zero spin results in a considerably simpler two-body scattering amplitude for pion-nucleon reactions than for nucleon-nucleon reactions. Also, along with the three charge states, the pion's spinlessness allows an easier parameterization of the scattering amplitude and fits to the experimental $\pi^+p \rightarrow \pi^+p$, $\pi^-p \rightarrow \pi^-p$, and $\pi^-p \rightarrow \pi^0n$ data. Thus, the most important pion-nucleon phase shifts have been determined accurately over a large incident pion energy region ($T_\pi(\text{lab}) < 500$ MeV). (3) The pion's light mass ($\sim 1/7$ of the mass of a nucleon) and its distinguishability from nucleons means that recoil effects, projectile structure, and particle exchange between the projectile and target are not as important to consider or do not need to be considered in a theoretical treatment of pion-nucleus scattering as is the case for other hadronic probes such as protons and alpha particles. (4) Lastly, the total π^+p and π^-p cross sections (see Fig. I-1) exhibit many resonances resulting in strong energy- and charge-dependent cross sections. The total cross section for $p + p$ shown in Fig. I-1 shows no resonant structure. At low to medium incident pion energies of $100 < T_\pi < 300$ MeV, the π^+p and π^-p cross sections are dominated by the

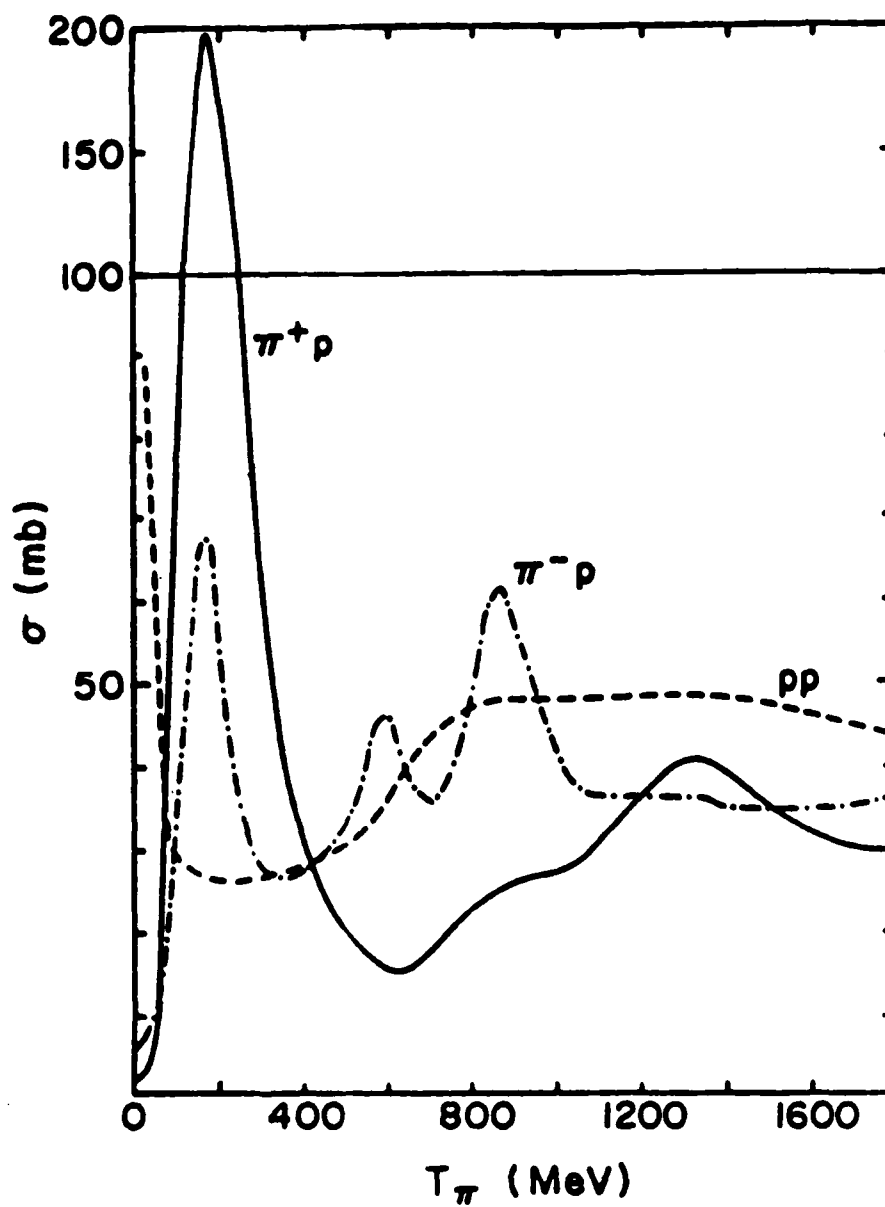


Fig. I-1: Total cross sections for π^+p (solid line) and π^-p (dot-dashed line) scattering as a function of lab kinetic energy T_π and the total pp cross section for comparison [E1-80].

$\Delta(1232)$ resonance ($\Gamma \sim 110-122$ MeV) which occurs when the phase shift of the $l=1$, $J=3/2$, $T=3/2$ partial wave rises through 90° at $T_\pi \approx 195$ MeV.

The $\Delta(1232)$ resonance is extremely important in pion-nucleus scattering. The most prevalent theoretical description of pion-nucleus inelastic scattering uses the distorted-wave impulse approximation (DWIA), treating nuclear transitions in the Born approximation. Such a description involves the basic pion-nucleon interaction; therefore, the energy, spin, and isospin dependences of the pion-nucleus interaction result from the energy, spin, and isospin dependences of the pion-nucleon interaction, which is dominated by formation of the $\Delta(1232)$ resonance. Thus, to understand the utility of the pion as a probe of nuclear structure, one needs to look at pion-nucleon scattering in the energy region of the $\Delta(1232)$ resonance.

The center-of-mass differential cross section for the elastic scattering of two particles with spin s_1 and s_2 is [Ta-72]

$$d\sigma/d\Omega_{c.m.}(\vec{p}', \chi' \rightarrow \vec{p}, \chi) = |\langle \chi' | F(\vec{p}' + \vec{p}) | \chi \rangle|^2, \quad (I-1)$$

where \vec{p} , \vec{p}' are the initial and final relative momenta, $|\chi\rangle$, $|\chi'\rangle$ are the general initial and final spin states of the two particle system ($|\chi\rangle = \sum_{\xi} \chi_{\xi} |\xi\rangle$), and $F(\vec{p}' + \vec{p})$ is the scattering amplitude matrix consisting of the $[(2s_1 + 1)(2s_2 + 1)]^2$ individual scattering amplitudes $f_{\xi'\xi}(\vec{p}' + \vec{p})$. $|\xi\rangle$ labels the basis vector $|m_1 m_2\rangle$ or $|s, m\rangle = \sum_{m_1, m_2} |m_1, m_2\rangle \langle s_1 s_2 m_1 m_2 | s m \rangle$. For the case of pion-nucleon scattering ($s_1=0$, $s_2=1/2$), $F(\vec{p}' + \vec{p})$ is a (2×2) matrix and its most general form which is compatible with invariance under rotations and parity is [Ta-72]

$$F(\vec{p}' + \vec{p}) = a(E_p, \theta)I + ib(E_p, \theta)\hat{n} \cdot \vec{\sigma} , \quad (I-2)$$

where θ is the scattering angle, E_p is the center-of-mass energy, I is the unit (2×2) matrix, $\vec{\sigma}$ denotes the Pauli spin matrices, and \hat{n} is the unit normal to the scattering plane ($\hat{n} = (\vec{p} \times \vec{p}')/(|\vec{p} \times \vec{p}'|)$). With this form for $F(\vec{p}' + \vec{p})$, the unpolarized center-of-mass differential cross section for elastic pion-nucleon scattering is

$$d\sigma/d\Omega_{c.m.}(\vec{p}' + \vec{p}) = |a(E_p, \theta)|^2 + |b(E_p, \theta)|^2 . \quad (I-3)$$

Both orbital and total angular momentum are conserved as well as the total isospin in pion-nucleon scattering. One can thus expand $F(\vec{p}' + \vec{p})$ in partial waves according to

$$F(\vec{p}' + \vec{p}) = \sum_T Q_T \sum_{\ell} (2\ell + 1) \sum_J P_{\ell, J} \alpha_{2T, 2J}^{\ell}(p) P_{\ell}(\cos \theta) , \quad (I-4)$$

where Q_T and $P_{\ell, J}$ project onto states of definite total isospin T and total angular momentum J , respectively, and the partial-wave amplitudes $\alpha_{2T, 2J}^{\ell}$ are expressed in terms of the phase shifts according to

$$\alpha_{2T, 2J}^{\ell}(p) = \frac{e^{i\delta_{2T, 2J}^{\ell}(p)} \sin[\delta_{2T, 2J}^{\ell}(p)]}{p} . \quad (I-5)$$

The total isospin is $T=1/2$ or $3/2$ and the total angular momentum is $J=\ell+1/2$ or $\ell-1/2$. The projection operators are

$$Q_{1/2} = 1/3(1 - \vec{I} \cdot \vec{\tau}) \quad Q_{3/2} = 1/3(2 + \vec{I} \cdot \vec{\tau}) , \quad (I-6a)$$

$$P_{\ell, J=\ell-1/2} = \frac{\ell - \vec{\sigma} \cdot \vec{L}}{2\ell + 1} \quad P_{\ell, J=\ell+1/2} = \frac{\ell + 1 + \vec{\sigma} \cdot \vec{L}}{2\ell + 1} , \quad (I-6b)$$

with \vec{I} the pion isospin operator and $\vec{\tau}$ the nucleon Pauli isospin operator. Substituting these expressions into Eq. (I-4), keeping only the $\ell=0$ (s wave) and $\ell=1$ (p wave) terms (since these are the most important partial-wave amplitudes in the energy range $0 < T_\pi < 345$ MeV [Ei-80]), and comparing to Eq. (I-2),

$$F(\vec{p}' + \vec{p}) = (a_0 + a_1 \vec{I} \cdot \vec{\tau})I + i(b_0 + b_1 \vec{I} \cdot \vec{\tau})\hat{n} \cdot \vec{\sigma} , \quad (I-7a)$$

with

$$a_0 = 1/3(\alpha_{1,1}^0 + 2\alpha_{3,1}^0) + 1/3(\alpha_{1,1}^1 + 2\alpha_{3,1}^1 + 2\alpha_{1,3}^1 + 4\alpha_{3,3}^1)\cos\theta , \quad (I-7b)$$

$$a_1 = 1/3(-\alpha_{1,1}^0 + \alpha_{3,1}^0) + 1/3(-\alpha_{1,1}^1 + \alpha_{3,1}^1 - 2\alpha_{1,3}^1 + 2\alpha_{3,3}^1)\cos\theta , \quad (I-7c)$$

$$b_0 = 1/3(\alpha_{1,3}^1 - \alpha_{1,1}^1 + 2\alpha_{3,3}^1 - 2\alpha_{3,1}^1)\sin\theta , \quad (I-7d)$$

$$b_1 = 1/3(-\alpha_{1,3}^1 + \alpha_{1,1}^1 + \alpha_{3,3}^1 - \alpha_{3,1}^1)\sin\theta . \quad (I-7e)$$

a_0 and b_0 are the isoscalar terms, a_1 and b_1 the isovector terms, and b_0 and b_1 the spin-flip terms.

As mentioned previously, for $100 < T_\pi < 300$ MeV, pion-nucleon scattering is dominated by the $\Delta(1232)$ resonance. Therefore, the largest phase shift in this energy range is $\delta_{3,3}^1$. With Eqs. (I-3) and (I-7) and

using only the $\alpha_{3,3}^1$ partial-wave amplitude, the unpolarized center-of-mass differential cross sections for $\pi^\pm p$ elastic and SCX scattering are

$$d\sigma/d\Omega(\pi^+p \rightarrow \pi^+p) = (4\cos^2\theta + \sin^2\theta)|\alpha_{3,3}^1|^2, \quad (\text{I-8a})$$

$$d\sigma/d\Omega(\pi^-p \rightarrow \pi^-p) = 1/9(4\cos^2\theta + \sin^2\theta)|\alpha_{3,3}^1|^2, \quad (\text{I-8b})$$

$$d\sigma/d\Omega(\pi^-p \rightarrow \pi^0n) = 2/9(4\cos^2\theta + \sin^2\theta)|\alpha_{3,3}^1|^2. \quad (\text{I-8c})$$

Since the total cross section for π^-p scattering below the threshold for pion-nucleon inelastic scattering ($T_\pi \approx 173$ MeV, but inelastic processes are not important for $T_\pi < 400$ MeV) is the sum of the elastic and SCX scattering, from Eq. (I-8)

$$\sigma_T(\pi^+p)/\sigma_T(\pi^-p) = 3, \quad (\text{I-9})$$

in agreement with the experimental total cross sections shown in Fig. I-1. Also from Eq. (I-8),

$$\sigma(\pi^+p)/\sigma(\pi^-p) = 9, \quad (\text{I-10a})$$

$$\sigma(\pi^+p)/\sigma(\text{SCX}) = 9/2. \quad (\text{I-10b})$$

Experimental pion-nucleon data taken at energies near the peak of the $\Delta(1232)$ resonance confirm these ratios. Thus, assuming that only the $\alpha_{3,3}^1$ (P_{33}) partial-wave amplitude contributes to pion-nucleon scattering (in the energy range $100 < T_\pi < 300$ MeV) introduces little error. Consequently, using $P_{3,3}$ dominance and the impulse approximation, one can obtain simple, transparent expressions for pion-nucleus scattering.

For example, keeping only the P_{33} partial-wave amplitude, Eq. (I-7) is

$$F(\vec{p}' + \vec{p}) = 1/3 \alpha_{1,3} (2 + \vec{I} \cdot \vec{\tau}) [2 \cos \theta + i \hat{n} \cdot \vec{\sigma} \sin \theta] . \quad (\text{I-11})$$

Siciliano and Walker [Si-81], following the approach of Gupta and Walker [Gu-76] and using a single-step, impulse-approximation mechanism, showed that the differential cross section for pion-nucleus inelastic scattering retains the same basic energy, isospin, and spin dependence. For unnatural-parity transitions ($\Delta\pi = (-1)^{J+1}$, where $\Delta\pi$ is the parity change and J is the total angular momentum transfer) the spin transfer is $\Delta S = 1$, and such transitions must proceed through the $\hat{n} \cdot \vec{\sigma}$ operator of Eq. (I-11). As a result, the constant-momentum-transfer (q) excitation functions should decrease with increasing incident pion energy according to $\sin^2 \theta$. Such an energy dependence was first observed [Co-79] for unnatural-parity transitions to the 4^- , 19.25-MeV state and 2^- structure at ≈ 18.4 MeV in ^{12}C and later [Se-81] to the $9/2^+$, 9.5-MeV state in ^{13}C . Microscopic DWIA calculations, using harmonic oscillator forms for the spin transition densities, reproduce well both the excitation functions and the shapes of the angular distributions for the 4^- state of ^{12}C [Co-84] and the $9/2^+$ state of ^{13}C [Se-81a, Se-82].

Transitions to states of stretched configuration, $(j_p j_h^{-1})^{J_s}$ with $j_p = l_p + 1/2$, $j_h = l_h + 1/2$, and $J_s = j_p + j_h$, are an important subclass of unnatural-parity transitions. For these transitions only the $L = J_s - 1$ (L is the orbital angular momentum transfer) spin transition density is involved in the (e, e') , (p, p') , and (π, π') reactions [Mo-74].

Using harmonic oscillator forms for the spin transition densities with the size and strength parameters fixed from (e, e') and (p, p') data, Carr, et al. [Ca-83] obtained good agreement between DWIA calculations and the (π, π') data for the 4^- , 17.79-, 18.98-, and 19.80-MeV states of ^{16}O and the 6^- , T=0 and T=1 states at 11.58 and 14.36 MeV in ^{28}Si .

The above examples illustrate that, in the energy range of the $\Delta(1232)$ resonance, calculations using the DWIA and well-known transition densities are adequate for describing the pion-induced excitation of nuclear states that are strongly excited. However, for pion-induced excitation of nuclear states which are weakly excited by a one-step, impulse-approximation mechanism, nuclear medium effects and multistep processes may be important and there may not even be qualitative agreement between pion inelastic scattering data and DWIA calculations. This is indeed the case for the T=1 member of the weakly excited 1^+ doublet, 12.71 MeV (T=0) and 15.11 (T=1), of ^{12}C [Mo-82]. As can be seen from Eq. (I-11), the ratio of cross sections for $\Delta S=1$ transitions should be $\sigma(\Delta T=0)/\sigma(\Delta T=1) = 4/1$, provided that the form factors for the two transitions are the same [Gu-76]. Furthermore, this ratio is approximately correct in DWIA calculations which include all s- and p-wave partial amplitudes. Cohen-Kurath p-shell wave functions [Co-65] describe the 12.71- and 15.11-MeV states as near analogs (i.e., the space-spin pieces of the wave functions are approximately the same), and this description for the spin densities is supported by (e, e') data [Co-84]. Nonetheless, although both the experimental excitation function and the angular distributions for the 12.71-MeV state are well reproduced by DWIA calculations, the measured ratio of four times the averaged π^+

and π^- differential cross sections for the 15.11-MeV state to the averaged π^+ and π^- differential cross sections for the 12.71-MeV state (see Fig. I-2) deviates significantly from one, especially at energies near 180 MeV ($\Delta(1232)$ dominance), and displays a rapidly varying energy dependence. (Averaging the π^+ and π^- differential cross sections removes the effect of isospin mixing between the two states on the ratio to better than 1% [Mo-82].) Also, DWIA calculations do not agree with the 15.11-MeV angular distributions at energies near the $\Delta(1232)$ resonance [Co-84].

Uncertainties in the spin transition density or the spin-dependent piece of the effective pion-nucleus interaction do not seem to be a plausible explanation [Mo-82] for the anomalous excitation function for the $\Delta S=\Delta T=1$ transition to the 15.11-MeV level of ^{12}C . Rather, a more likely explanation considers another process, in addition to a one-step, impulse-approximation mechanism, contributing to the isovector transition. A possible mechanism is the previously proposed [Mo-82] direct excitation of Δ particle-nucleon hole (Δ -h) components in the final state wave function. Thus, to further investigate pion-induced excitation of nuclear states which are weakly excited, where the DWIA may be inadequate and the direct excitation of Δ -h components may be an important piece of the scattering amplitude, this dissertation is concerned with the $\Delta S=\Delta T=1$ transition from the 1^+ , $T=0$, ground state of ^6Li to the 0^+ , $T=1$, 3.563-MeV level. As for the 15.11-MeV level of ^{12}C , the DWIA analysis of this unnatural-parity transition is particularly simple, involving only the spin-dependent piece of the effective pion-nucleus interaction and the spin transition density.

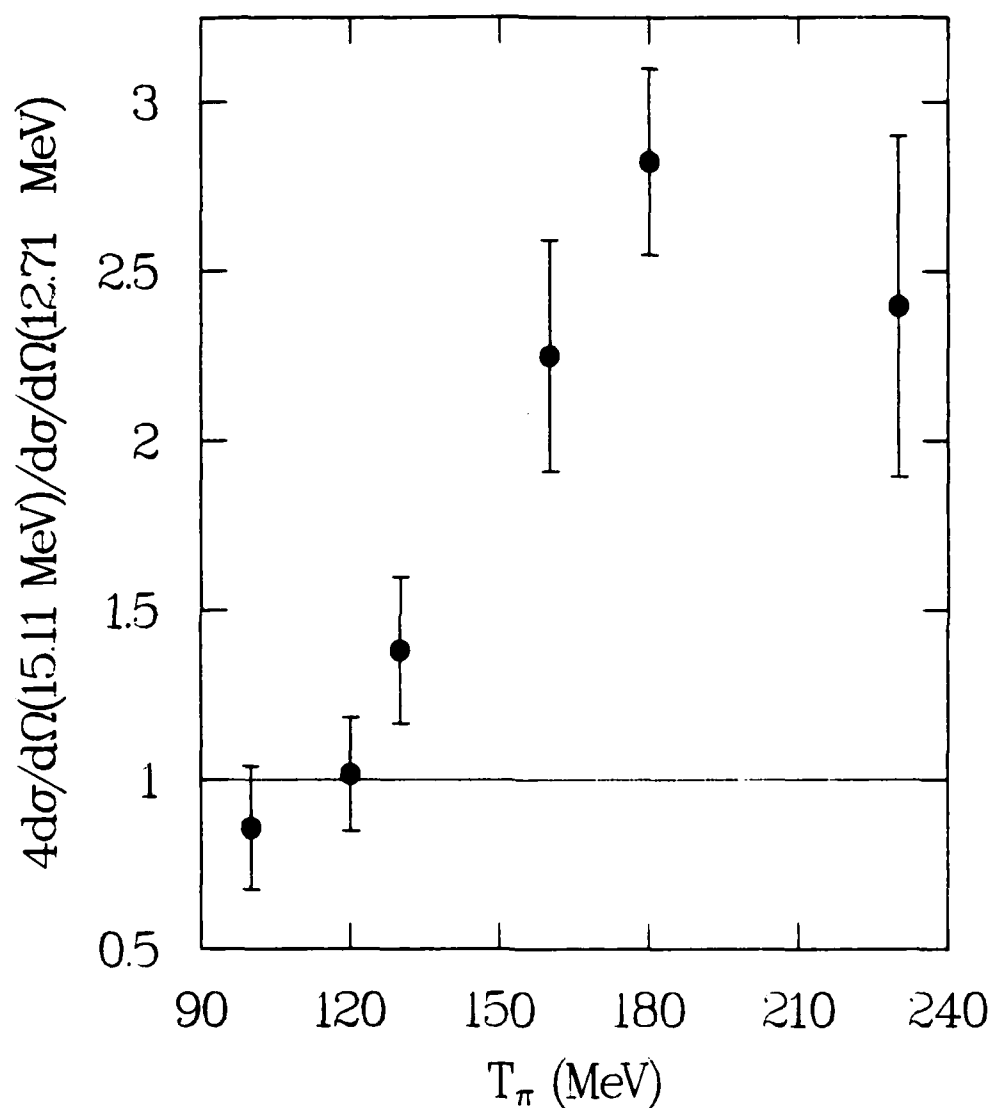


Fig. 1-2: Ratio of four times the differential cross sections (averaged π^+ and π^-) for π^+ inelastic scattering to the 1^+ , $T=1$, 15.11-MeV state of ^{12}C and the differential cross sections (averaged π^+ and π^-) for π^+ inelastic scattering to the 1^+ , $T=0$, 12.71-MeV state of ^{12}C [Mo-82].

Chapter II of this dissertation describes the experimental facility used to acquire the data. Chapter III describes the extraction of differential cross sections from the various (π^+, π^+) Q-value spectra. Also in this chapter is the presentation of the data, which consist of: (1) the first detailed measurement of a constant q , $q \approx 109$ MeV/c, excitation function for π^+ inelastic scattering to the weakly excited 3.563-MeV state of ${}^6\text{Li}$ at incident pion energies from 100 to 260 MeV, (2) partial angular distributions at $T_\pi = 120$ and 180 MeV for π^+ inelastic scattering to the 3.563-MeV level, and (3) differential cross sections for π^+ elastic scattering and for π^+ inelastic scattering to the 2.185-MeV (3^+ , $T=0$) and 4.25-MeV (2^+ , $T=0$) states. A discussion of non-relativistic multiple-scattering theory and its application to pion-nucleus scattering is given in Chapter IV. Chapter V presents the DWIA calculations performed for the three low-lying excited states of ${}^6\text{Li}$ and includes discussion of the data and calculations. Appendix C is a copy of the paper resulting from this dissertation experiment, which was received by Physical Review C in August 1984.

II. EXPERIMENTAL APPARATUS AND PROCEDURE

The data presented in this dissertation were collected using the Energetic Pion Channel and Spectrometer (EPICS) system at the Clinton P. Anderson Meson Physics Facility in Los Alamos, New Mexico (LAMPF). LAMPF is described in various Los Alamos Scientific Laboratory Reports [Li-72, Al-77, Li-77]. Briefly, LAMPF consists of an 800-MeV proton linear accelerator, capable of accelerating simultaneously H^+ ions and H^- ions (or polarized H^- ions), and several experimental areas for nuclear structure and chemistry studies. LAMPF was designed to produce a proton beam with an average current of 1 mA at a duty factor of 6-12%. However, during the experiment (June and November 1982) which provided the data for this dissertation, the average current was ≈ 700 -750 μA at a 7.5% duty factor. The H^+ beam enters Experimental Area A and impinges on the first graphite target (the A-1 target), producing pions (and other secondary particles) which the EPICS channel accepts at an angle of 35° from the H^+ beam direction. Experimental Area A is shown in Fig. II-1.

A. EPICS system

The EPICS system [Th-70] was designed to provide good energy resolution and good angular resolution studies of pion-induced excitation of nuclear levels, with cross sections as low as several nb/sr, from low incident pion energies of ~ 70 MeV to energies above the $\Delta(1232)$ resonance, ~ 300 MeV. EPICS consists of a high intensity, high resolution

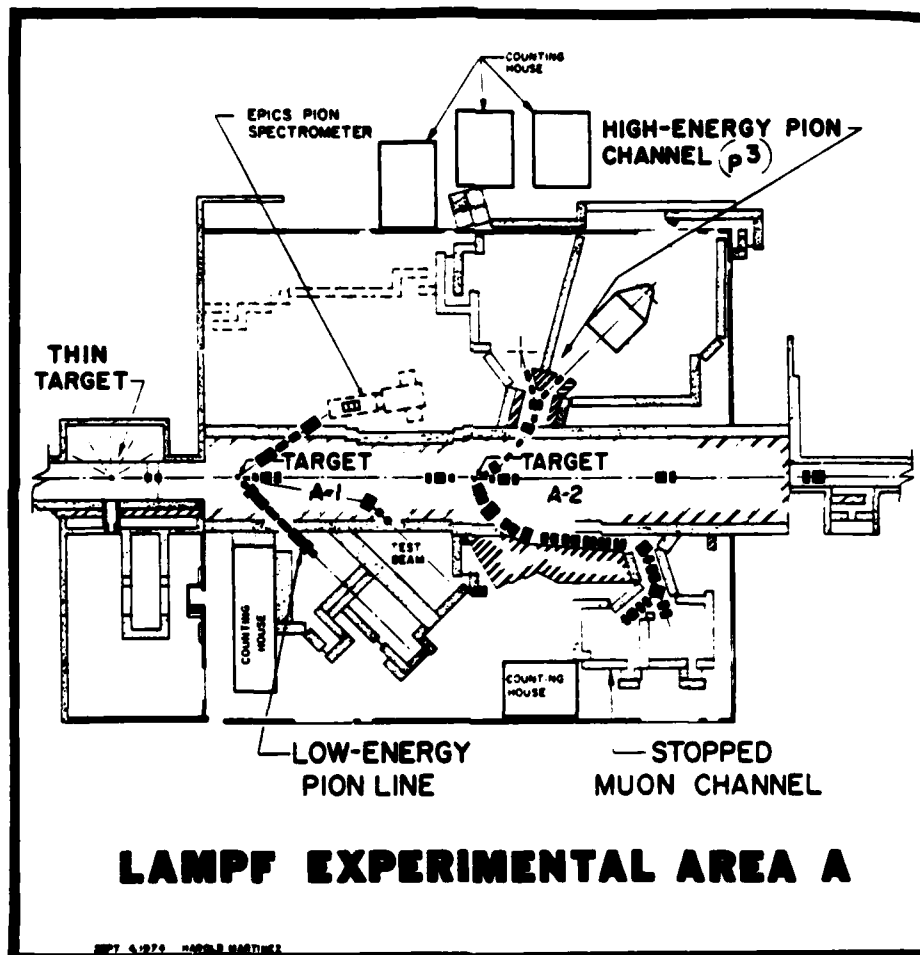


Fig. II-1: Experimental Area A of the LAMPF facility [L1-77].

pion beam channel, a scattering chamber, and a high resolution spectrometer. A diagram of the EPICS channel, scattering chamber, and spectrometer is shown in Fig. II-2. Table II-1 lists the specifications of the EPICS system.

The EPICS channel, shown in Fig. II-3, consists of four dipole magnets (BM01-BM04), three multipole focusing magnets (FM01-FM03), and four adjustable collimating jaws (FJ01-FJ04). The channel's length of 15.24 m was chosen in order to momentum select pions of maximum kinetic energy of 300 MeV, but be short enough to maintain a reasonable flux of 70 MeV pions even after pion decay through the channel. The four bending magnets provide charge and momentum selection and momentum dispersion of the channel beam. (In such a dispersed beam, the momentum of a particle is correlated with its position in the beam.) The optical mode is point to point to point to point in the vertical direction and point to parallel to point to parallel in the horizontal direction. FM01-FM03 each have three windings, quadrupole, half-sextupole (top), and half-sextupole (bottom), and are used for removing higher-order aberrations of the channel optics. The four adjustable collimating jaws determine the phase space and flux of the channel beam. FJ01 has only vertical jaws (disabled), and along with a fixed collimator, defines the channel acceptance. When FJ01 is operative, regulation of the channel beam intensity and vertical divergence is accomplished with FJ01. FJ02-FJ04 each have two pairs of jaws, one horizontal and one vertical. The vertical jaws of FJ04 define the channel momentum acceptance and, hence, the vertical size of the channel beam at the scattering target, while the horizontal jaws define the horizontal divergence of the beam. With all

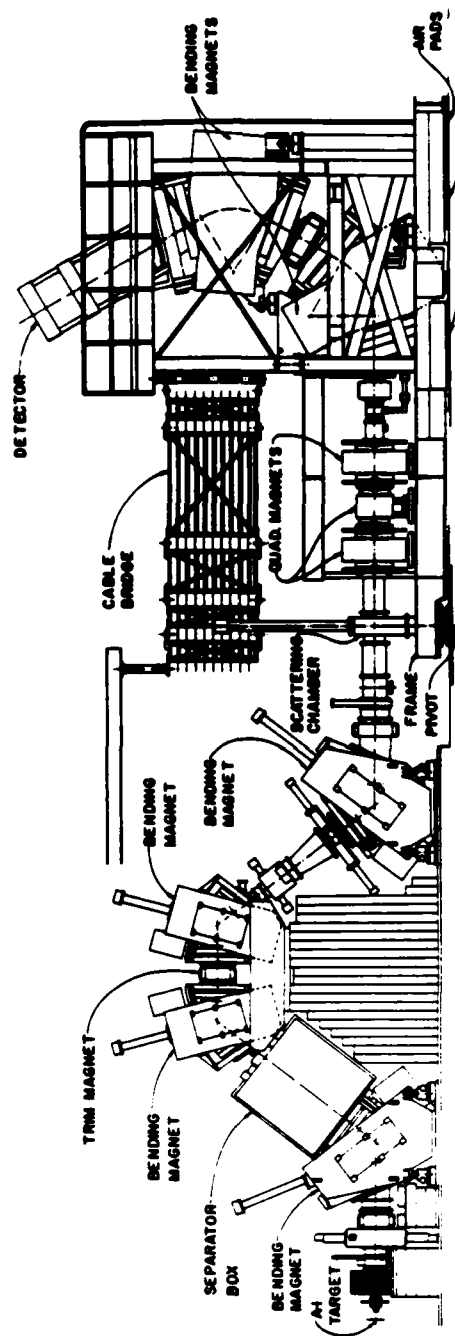


Fig. II-2: The Energetic Pion Channel and Spectrometer (EPICS) at LAMPF.

TABLE II-1: EPICS system specifications.^a

CHANNEL		SPECTROMETER	
Solid angle	3.4 msr	Solid angle	≈10 msr
$\Delta p/p$	2%	$\Delta p/p$	14%
Beam size (horizontal)	8 cm	Momentum range	100-750 MeV/c
Beam size (vertical)	20 cm	Flight path	≈125 cm
Beam divergence (horizontal)	<10 mrad	Dispersion	4 cm/%
Beam divergence (vertical)	100 mrad		
Energy range	70-300 MeV		

^aRef. [LA-80].

TABLE II-2: EPICS channel beam pion flux and composition.

T_{π} (MeV)	Pion Flux ^a			Beam Content ^b		
	π^+	π^-	π	p	μ	e
	($\times 10^7 \pi/s$)					
100	6.7	1.8	100	~35	15	50
200	22.0	4.7	100	~400	5	8
300	26.0	4.5	100	~650	2	2

^aNormalized to a primary proton beam average current of 1 mA [LA-80].^bThe relative beam contaminant numbers are normalized to the pion numbers [Bo-84].

jaws fully open, the channel beam at the scattering target has a vertical dispersion of 10 cm/%, a momentum bite of $\pm 1\%$, and a divergence of 100 mrad. In the horizontal plane, the divergence is < 10 mrad. The resultant beam spot is 20 cm (vertical) by 8 cm (horizontal) [LA-80], and the channel beam pion flux and composition are presented in Table II-2.

At the center of the scattering chamber, located at the focal plane of the channel, is the target ladder containing up to four full-size targets (22.9 cm \times 15.2 cm). Different targets are selected by moving the target ladder vertically. Also, the target ladder can be rotated relative to the channel beam. The normal procedure is to bisect the scattering angle, thus minimizing the path length traversed through the target. Minimum beam travel through the target minimizes straggling which, in turn, helps to maximize the resolution. To balance acceptable resolution against count rates, target areal densities for pion elastic and inelastic scattering experiments range from 100 to 300 mg/cm².

The EPICS spectrometer (see Fig. II-4) consists of a quadrupole triplet (QM01-QM03), two dipole magnets (BM05-BM06), and front and rear focal plane detector systems. The spectrometer rotates about its pivot, situated at the focal plane of the channel, through an angular range of -10° to 120° . The optical mode from the scattering target, through the quadrupole triplet, to the front focal plane (located just before the two dipole magnets) is point to point in the vertical direction and parallel to point in the horizontal direction. A magnification of -1 is provided by the quadrupole triplet, forming an inverted image of the scattering target in which x is proportional to x at the scattering target and y is proportional to the scattering angle at the scattering target. The two

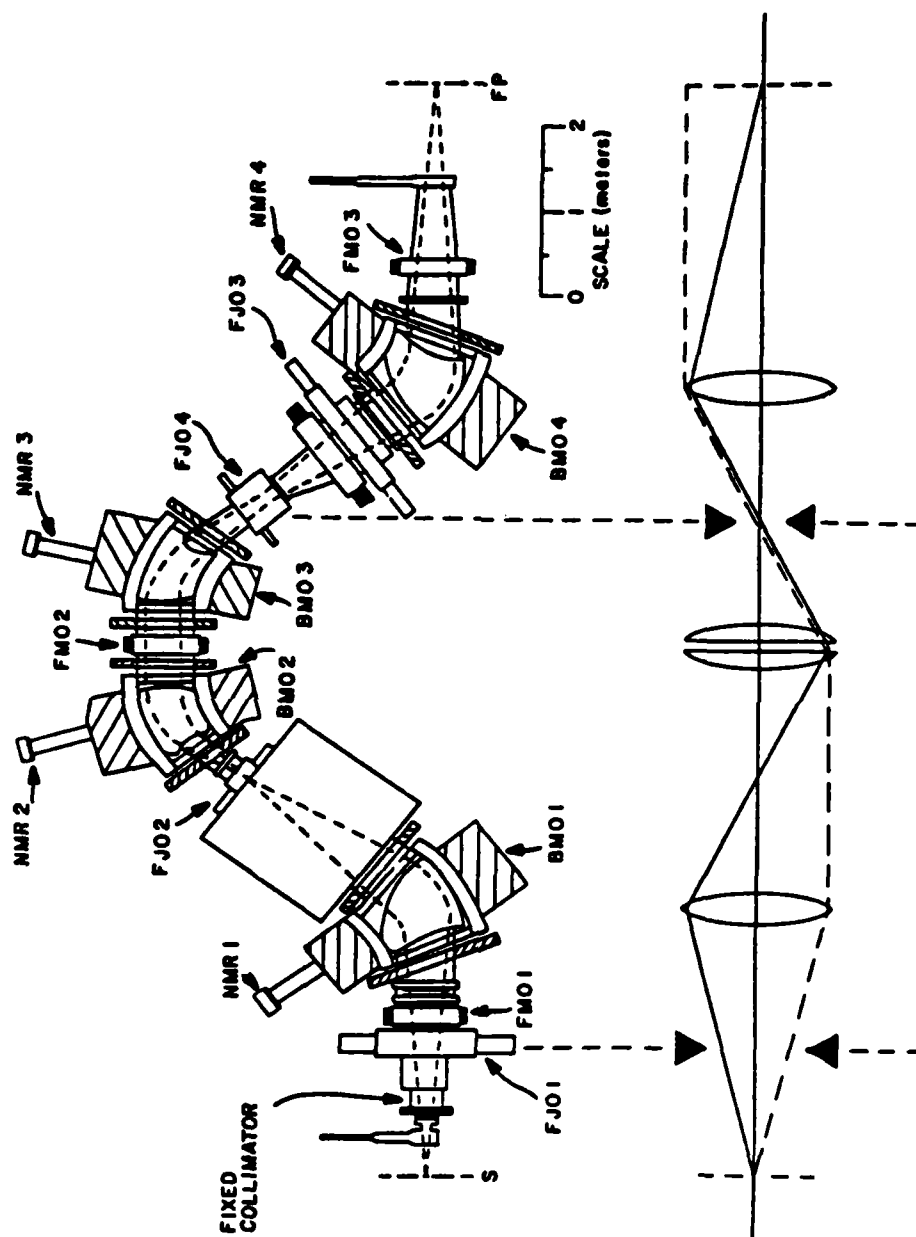


Fig. II-3: The EPICS channel and its optical mode. The solid (dashed) line illustrates the optics for the vertical (horizontal) plane [Th-77].

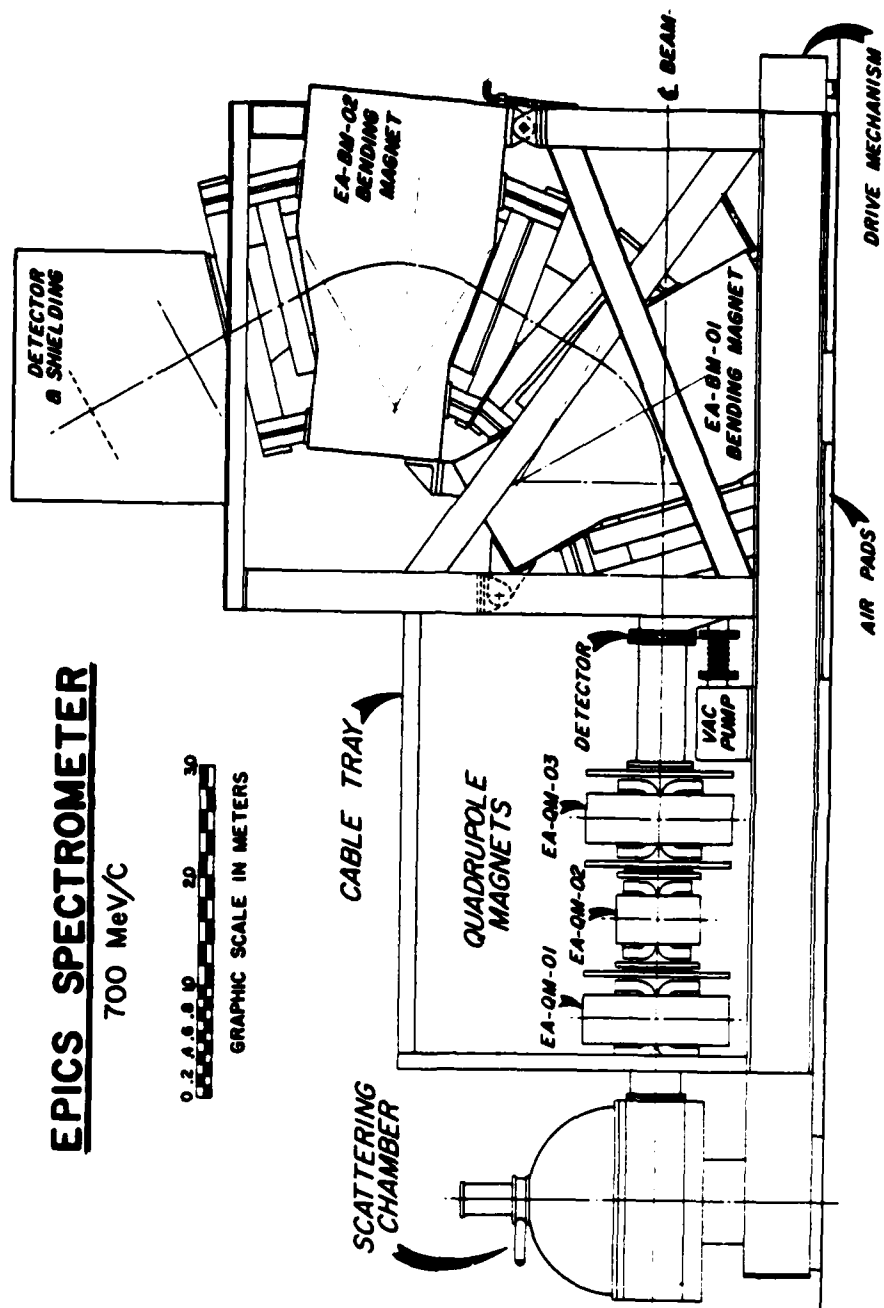


Fig. II-4: The EPICS spectrometer [L1-77].

dipole magnets vertically disperse the beam, 4 cm/%, and the useful momentum bite of the spectrometer is $\pm 6\%$. Their optical mode is point to point in the vertical direction and point to parallel in the horizontal direction. Fig. II-5 illustrates the optics of the spectrometer and the coordinate system used in defining particle trajectories. Also shown are the front and rear focal plane detector systems. The front focal plane detector system is a set of four multiwire proportional drift chambers (F1-F4) with F4 located at the focal plane of the quadrupole triplet. The rear focal plane detector system consists of four multiwire proportional drift chambers (R5-R6, R9-R10), with R5 located at the rear focal plane, a scintillator (S2), a slab of Lucite used to range out protons, a scintillator (S3), and a muon rejector.

B. Detector system and beam monitoring

Since the spectrometer is not dispersion matched to the channel, the detector systems at the front and rear focal planes must measure both particle positions and angles in order to determine the incident particles' momenta and the scattered particles' momenta. These two quantities allow determination of the reaction kinematics. Thus, in order to obtain good momentum resolution, the multiwire proportional drift chambers must provide good position resolution. The multiwire proportional drift chambers used in the EPICS spectrometer [At-81, Mo-82a] provide position resolutions of 125 μm (FWHM) and may operate at count rates up to 10^6 Hz. The set of four multiwire proportional drift chambers (F1-F4) at the front focal plane are packaged in one chamber

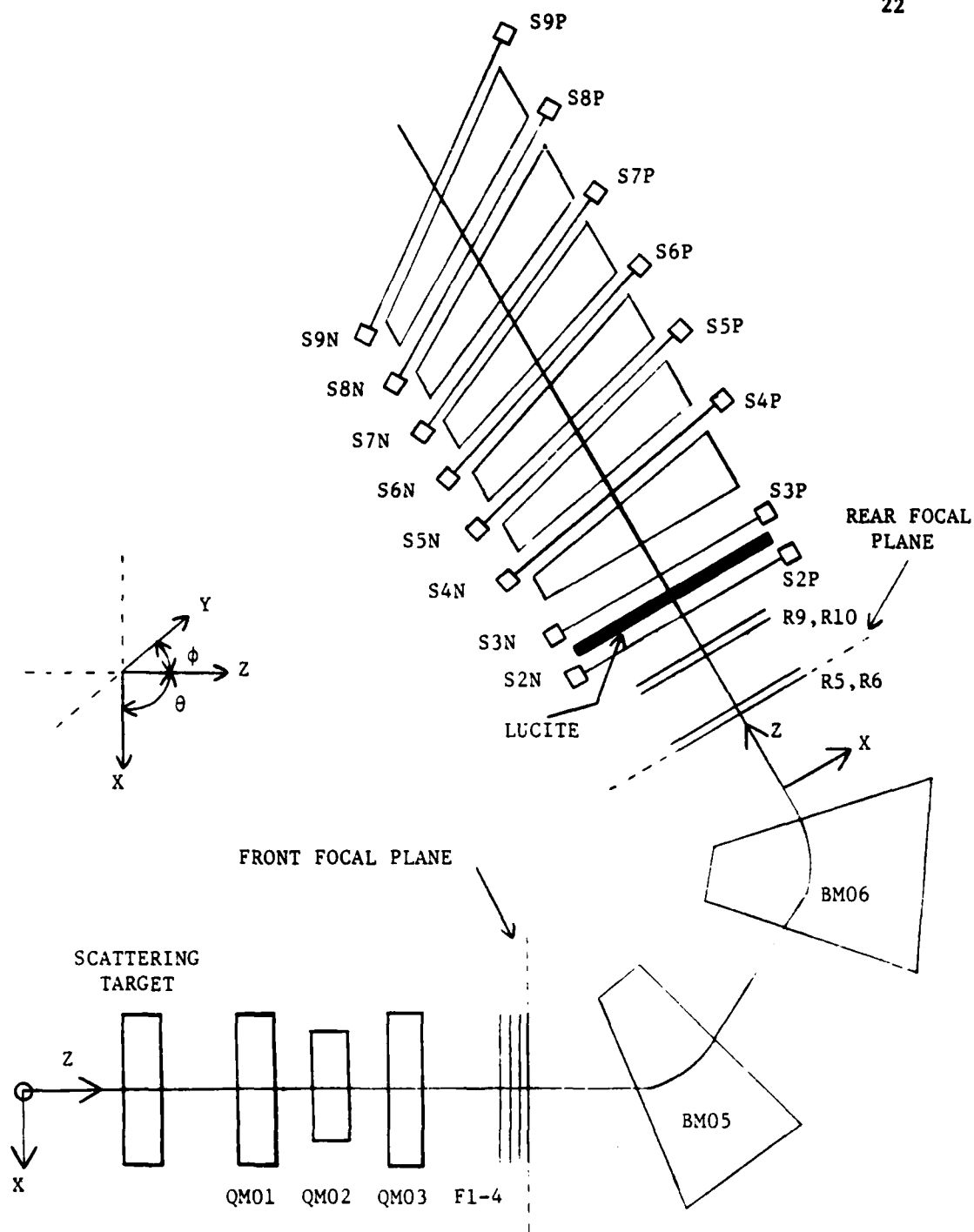


Fig. II-5: The EPICS spectrometer optics and the detector system.

assembly. This chamber assembly consists of eight signal planes, two orthogonal sets of four planes each in order to obtain vertical and horizontal position (x,y) and angle (θ,ϕ) information, with each signal plane separated by grounded foil planes. Each set of four signal planes with the signal wires in the same direction are arranged as two sets of two signal planes. The two sets of signal planes are separated by 10 cm. Within each set of two signal planes, the two signal planes are separated by 1 cm and offset with respect to each other by one-half of a wire spacing. The set of four multiwire proportional drift chambers (R5-R6, R9-R10) at the rear focal plane are packaged in two chamber assemblies, each consisting of four signal planes, two orthogonal sets of two planes each. Their construction is the same as the front chamber assembly. All signal planes are of an alternating gradient design, with the anode wires at positive high voltage (typically 2150 V) and a wire spacing of 8 mm, and cathode wires at -200 V centered between the anode wires. The anode wires are directly coupled into a fast (2.5 ns/cm) delay line, thus giving two anode signals per signal plane, while alternate cathode wires are bussed together, thus giving two cathode signals per signal plane. Presently, only the two anode signals per plane are used to calculate positions and angles. Calculation of position is as follows. A time difference and time sum from the two anode signals are formed. The time difference is directly related to the position of the wire closest to the ionizing event, determining the position of an event to ± 4 mm. Further position resolution is obtained from the time sum, which is equal to twice the drift time to the event wire plus a constant offset. However, one must decide whether to add to or subtract from the drift distance the

anode wire position. This left-right ambiguity can be solved with four signal planes, hence, the need for eight signal planes at the two focal planes, and is described in [At-81, Mo-82a, Iv-79]. Angles are determined from the spacing (10 cm) of the two sets of two signal planes which comprise a set of four signal planes whose anode and cathode wires are in the same direction in conjunction with the positions measured in each set of two signal planes. Thus, the information provided by the multiwire proportional drift chambers located at the front and rear focal planes of the EPICS spectrometer consists of the eight quantities x_f , y_f , θ_f (dx_f/dz), ϕ_f (dy_f/dz), x_r , y_r , θ_r , ϕ_r .

Two scintillators (S2, S3) were the only scintillators used as part of the EPICS detector system during this experiment. They are located just after the rear set of multiwire proportional drift chambers and are separated by a slab of Lucite. Photomultiplier tubes are optically connected to each end of the scintillators. The purpose of the scintillators was twofold. They were used as part of the logic defining a hardware trigger signal for events and for particle identification. For particle identification, the signals from S2 and S3 are used to measure a time of flight between S2 and S3 and pulse heights, which are linearly proportional [Me-66] to the energy loss in the scintillators. Since time of flight is proportional to E/pc^2 and energy loss is proportional to $(ZeE/pc^2)^2$ [Me-66] (E is the total energy of the particle, p is the momentum, and Ze is the charge), these two measurements aid in distinguishing particles of different masses and charges.

Following scintillators S2 and S3 is a series of scintillators (S4-S9) separated by carbon wedges of varying thicknesses. (The wedge shape is needed to account for the variation of momentum across the rear focal plane.) This arrangement of six scintillators and six carbon wedges is known as the muon rejector [Mo-84]. The muon rejector is designed to eliminate the muon background from in-flight decay of pions before the front set of multiwire proportional drift chambers and elastic scattering of channel beam muons. The operation of the muon rejector is as follows. Since muons and pions both have a single unit of charge, muons and pions of the same momentum are transported to the rear focal plane. For the same momentum, the total energy of a pion is greater than a muon and thus the pion's range in matter is less than that of the muon ($-dE/dx \propto (ZeE/pc^2)^2 n_e$, where n_e is the electron density of the ranging material [Ja-75]). Furthermore, pions also lose energy due to nuclear collisions. The first carbon wedge is of the correct thickness to remove pions of 100 MeV kinetic energy but not muons. The second carbon wedge removes pions of 140 MeV kinetic energy but not muons, and so on. To remove pions of intermediate energies, there is space between S3 and the muon rejector to place varying thicknesses of aluminum. The signals from the scintillator following the carbon wedge of the desired pion energy are then used to veto muons (usually in the software). During this experiment, the muon rejector rejected most of the muon background (90-95%), while rejecting only 2-5% of the pions.

To obtain the normalization required in the calculation of pion elastic and inelastic differential scattering cross sections, three beam monitors are used. Several beam monitors provide cross checks on the

stability of each monitor. An ionization chamber (IC1) located downstream of the scattering target monitors the EPICS channel beam current. The primary beam current is monitored by an ionization chamber (BOT) located within the pion production target cell and a charge integrating toroidal coil (IACM02) located upstream of the pion production target. Both the BOT and IACM02 signals are gated by a RUN gate so that the primary beam current is monitored only during data acquisition. BOT and IACM02 are reliable indirect measures of the EPICS channel beam current provided the proton beam is always properly steered and strikes the A-1 target. For portions of this experiment, both BOT and IACM02 were used for normalization, because IC1 partially blocks the spectrometer entrance for $\theta_{\text{LAB}} < 25^\circ$ and is not used, and BOT was not operational near the end of the experiment. A careful check of the ratios IC1/BOT and IC1/IACM02 ($< 2\%$ fluctuations) for $\theta_{\text{LAB}} > 25^\circ$ proved the reliability of BOT and IACM02.

C. Data acquisition and analysis system

The data acquisition and analysis system for EPICS consists of an on-line PDP-11/45 computer which runs under DEC'S RSX11-D operating system, several CAMAC crates containing CAMAC electronic modules, a Microprogrammable Branch Driver (MBD) interfacing the PDP-11/45 and CAMAC crates, computer peripherals (tape drive, two graphics terminals, disk drive system, and a printer/plotter), and the LAMPF standard data acquisition software package "Q" for managing the data acquisition and display of the experimental data [Am-79]. The scintillator signals and

chamber signals are passed via coaxial cables from the focal planes to the counting house and fed into NIM modules, discriminators, Meantimers, ADC's, and TDC's for the scintillator signals and discriminators and TDC's for the chamber signals (see Fig. II-6). The logical "and" of the meantimed signals from S2 and S3 and at least two signals from both the four x planes and four y planes of the front multiwire proportional drift chambers define a trigger signal ($\text{trigger signal} = (S2 \cdot S3) \cdot (F1 \text{ or } F2) \cdot (F3 \text{ or } F4)$). This signal along with a logical "and" of the not-busy signal issued by the PDP-11/45 computer when it is ready to accept data constitutes the hardware trigger ($\text{hardware trigger} = (\text{trigger signal}) \cdot (\text{not-busy signal})$). The hardware trigger signal initiates the reading of the data words (20-100) for that event. The "Q" software [Ke-78] controls this reading, the writing of the data words for each event to magnetic tape, and processing of the events if time is available (MAY PROCESS mode of on-line data acquisition). Both the trigger signals and the hardware trigger signals are scaled along with other quantities such as $S2 \cdot S3$, $(F1 \text{ or } F2) \cdot (F3 \text{ or } F4)$, ICI, BOT, IACMO2, etc. The "Q" software reads the scalers at fixed time intervals and stores all quantities in a scaler file. The ratio of the number of hardware trigger signals ($\text{EVENT} \cdot \overline{\text{BUSY}}$) to the number of trigger signals (EVENT) is a measure of the computer's rate of data taking, the computer live time ($\text{CLT} = \text{EVENT} \cdot \overline{\text{BUSY}} / \text{EVENT}$).

An important part of the EPICS electronics not shown in Fig. II-6, but used during the experiment, is a fast clear circuit used to eliminate the majority of the hardware trigger signals corresponding to elastic scattering events [Se-81a]. The fast clear circuit aids in the

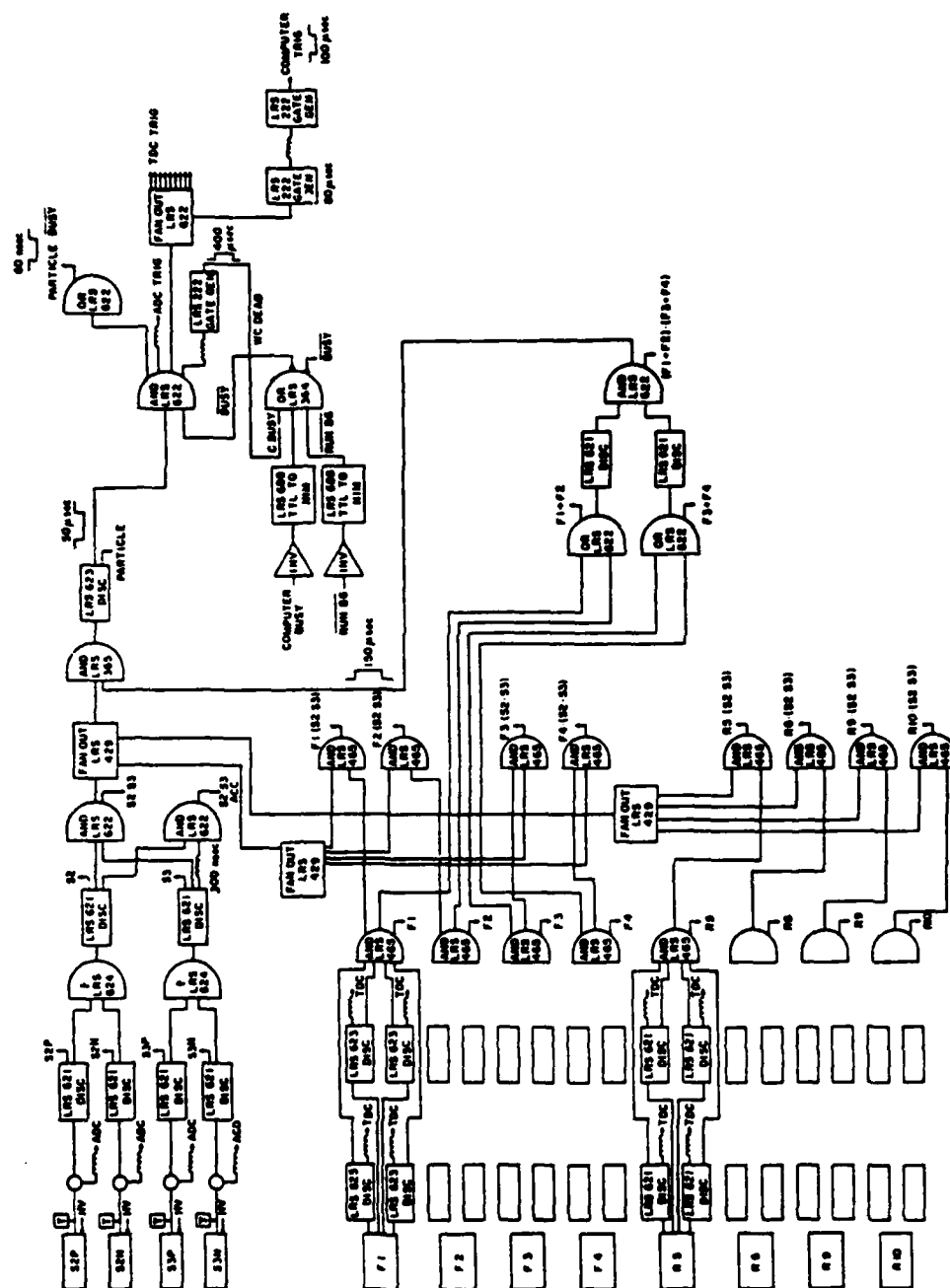


Fig. II-6: Block diagram of the electronics for the EPICS data acquisition system.

measurement of small inelastic scattering cross sections relative to elastic scattering. This circuit produces a signal which is used to veto 9 out of 10 or 99 out of 100 hardware trigger signals; thus, the data words for only one of 10 or one of 100 elastic scattering events are read into the computer, written to magnetic tape, and processed (if time is available). The number of vetoed hardware trigger signals (FAST CLEAR) are scaled.

Once the data words for an event are read into the computer, the processing of the data is done on an event by event basis with the standard analyzer task for EPICS data-taking (QEPX) in conjunction with a test file (experiment-specific) and a display package (experiment-specific). The goal of the data processing is to determine which events are good pion events and calculate the excitation energy given to the target nucleus by these pions. This goal is accomplished through the main program of the analyzer (PROC06). PROC06 examines each event and calls subroutines to calculate all chamber and scintillator quantities from the outputs of the TDC's and ADC's, calculate trajectory information, use the test file to test the various quantities, compute the missing mass associated with each event, and arrange the data in bins for storage in histograms determined by the display package.

The test file [Am-78] consists of the user-specified tests to be performed on each event. The test file is structured into loops, and the loops are called separately and in order by the analyzer. Each loop may contain two types of tests, microtests and macrotests. The microtests are tests on the data words, and the macrotests are tests on logical combinations of previous microtests or macrotests. Microtests can be a

BIT test which is true if a specified bit is set in a specified data word, a GATE (DIRECT or INDIRECT) test which is true if the specified integerized data word is greater than a given lower limit and less than or equal to a given upper limit, and a BOX test which is a combination of two INDIRECT GATE tests. Macrotests are logical "and's", "inclusive or's", or "exclusive or's" on specified microtests or macrotests.

The display package (DSP) is used to construct and display both one-dimensional histograms and two-dimensional dot plots. Histograms and dot plots are defined by the data words to be histogrammed or plotted, lower and upper limits of display, a binning factor, and the tests defined in the test file which the event must pass. Both histograms and dot plots can be viewed on a graphics terminal during on-line data acquisition. However, only histograms can be saved for later data analysis. In addition to saving histograms, scaled quantities, the results of the test file, and the relevant kinematic information for each experimental run (period of data acquisition, ~ 155,000 taped events) are saved for off-line data analysis.

D. Event analysis

The following paragraphs describe in more detail the various steps in the data analysis, leading to a missing mass histogram of good pion events which can be used to calculate scattering cross sections. Fig. II-7 is a test file used during the experiment for this dissertation. The first calculation for an event performed by the analyzer is the particle identification test (PID) (see test #11 in Fig.

```

RUN 485
12-APR-63 12:01:30 EVENT 6 FILE C 135,303JDP.TST

49991. = GAT,259,10000,12000.. :1 :S1 DE/DX :DEV.TST
49991. = GAT,251,10000,12000.. :2 :S2 DE/DX PRODUCT :LARGE JMS
49991. = GAT,252,10000,12000.. :3 :S3 DE/DX PRODUCT
7843. = 01.2.0. :4 :S4 MUON
374. = 01.2.1. :5 :S5
240. = 01.2.2. :6 :S6
179. = 01.2.3. :7 :S7
104. = 01.2.4. :8 :S8
360. = 01.2.5. :9 :S9
0. = GAT,3.1,32000. :10 :FAST CLEAR (1/10 OR 1/100)
46459. = BOX,1. :11 :BOX 1 ==> PID
7843. = AND,2.3.4. :12 :GOOD DE/DX
924. = TOR,6.7.8.9. :13 :BIT TEST
340. = AND,11.5. :14 :PID=CERENKOV
46119. = AND,11.-5. :15 :PID=NOT(CERENKOV)
49991. = TOR,1.-1. :16 :LOOP1 COUNTER
45702. = GAT,141,9990,10140. :17 :1A DRFTMA :CHAMBER LOOP 2
45821. = GAT,142,9990,10140. :18 :2A DRFTMA
45870. = GAT,143,9990,10140. :19 :3A DRFTMA
45809. = GAT,144,9990,10140. :20 :4A DRFTMA
45816. = GAT,145,9990,10140. :21 :5A DRFTMA
45824. = GAT,146,9990,10140. :22 :6A DRFTMA
44893. = GAT,149,9990,10140. :23 :9A DRFTMA
45669. = GAT,150,9990,10140. :24 :10A DRFTMA
45977. = GAT,201,9990,10140. :25 :1C DRFTMC
45909. = GAT,202,9990,10140. :26 :2C DRFTMC
45968. = GAT,203,9990,10140. :27 :3C DRFTMC
45955. = GAT,204,9990,10140. :28 :4C DRFTMC
46100. = GAT,205,9990,10140. :29 :5C DRFTMC
46173. = GAT,206,9990,10140. :30 :6C DRFTMC
46074. = GAT,209,9990,10140. :31 :9C DRFTMC
46179. = GAT,210,9990,10140. :32 :10C DRFTMC
0. = GAT,147,9926,9902. :33 :7 CHECKSUM (QUAD)
0. = GAT,140,9949,10002. :34 :8 CHECKSUM (QUAD)
42005. = GAT,272,9990,10015. :35 :FRONT DRF DIF PLANE A
43340. = GAT,273,9990,10015. :36 :FRONT DRF DIF PLANE C
40349. = GAT,274,9990,10015. :37 : REAR DRF DIF PLANE A
41739. = GAT,275,9990,10015. :38 : REAR DRF DIF PLANE C
33590. = AND,11,35,36,37,38. :39 :DRF DIFF TST*PID ==> DRF
44900. = AND,11,25,26,27,28. :40 :FRONT C CHAMBERS OK*PID
44640. = AND,11,17,18,19,20. :41 :FRONT A CHAMBERS OK*PID
45313. = AND,11,29,30,31,32. :42 :REAR C CHAMBERS OK*PID
43751. = AND,11,21,22,23,24. :43 :REAR A CHAMBERS OK*PID
43530. = AND,40,41. :44 :FRONT OK
42097. = AND,42,43. :45 :REAR OK
40299. = AND,44,45. :46 :ALL EXCEPT QUAD *PID ==> CHMRS
0. = TOR,33,34. :47 :QUAD OK
0. = AND,46,47. :48 :ALL OK
40549. = AND,17,19,20,40,45. :49 :ALL BUT 1A CHAMBERS EFFICIENCY TEST
40536. = AND,17,18,20,40,45. :50 :ALLBUT 2A
40543. = AND,17,18,19,40,45. :51 :ALLBUT 3A
40540. = AND,22,23,24,42,44. :52 :ALLBUT 4A
40525. = AND,21,23,24,42,44. :53 :ALLBUT 5A
41346. = AND,21,22,24,42,44. :54 :ALLBUT 6A
40603. = AND,21,22,23,42,44. :55 :ALLBUT 9A
40529. = AND,26,27,20,41,45. :56 :ALLBUT 10A
40527. = AND,25,27,20,41,45. :57 :ALLBUT 1C
40561. = AND,25,26,20,41,45. :58 :ALLBUT 2C
40562. = AND,25,26,27,41,45. :59 :ALLBUT 3C
40519. = AND,30,31,32,43,44. :60 :ALLBUT 4C
40460. = AND,29,31,32,43,44. :61 :ALLBUT 5C
40537. = AND,29,30,32,43,44. :62 :ALLBUT 6C
40450. = AND,29,30,31,43,44. :63 :ALLBUT 9C
:64 :ALLBUT 10C

```

Fig. II-7: Sample test file.

42597.	• GAT,233,9354,10715.	:65	:XTGT :BACKGROUND REJECTION LOOP 3
43760.	• GAT,234,8700,11200.	:66	:THTTGT
42000.	• GAT,235,9630,10400.	:67	:YTGT
44026.	• GAT,236,9500,10600.	:68	:PHITGT
31590.	• GAT,237,9900,10100.	:69	:THTCHK
35170.	• GAT,238,9900,10100.	:70	:PHICMK
41101.	• GAT,163,9990,11400.	:71	:FLR1 CUT
41349.	• GAT,166,9990,11400.	:72	:FLR2 CUT
45260.	• GAT,221,9095,10740.	:73	:XFRONT PHASE SPACE CUTS
41476.	• GAT,222,9137,10951.	:74	:THETA FRONT
36032.	• GAT,223,9649,10501.	:75	:Y FRONT
43710.	• GAT,224,9660,10401.	:76	:PHI FRONT
0.	• BOX,2.	:77	:BOX 2
0.	• BOX,3.	:78	:BOX 3
117.	• BOX,4.	:79	:BOX 4
0.	• IGAT,6.	:80	:GATE 6 ==> ELASTIC PEAK
0.	• IGAT,1.	:81	:ROD 1
0.	• IGAT,2.	:82	:ROD 2 OR CTDF PIONS
0.	• IGAT,3.	:83	:ROD 3 OR CTDF MUONS
0.	• IGAT,4.	:84	:ROD 4
0.	• IGAT,5.	:85	:ROD 5
23119.	• AND,39,46,73,74,75,76.	:86	:PHASE SPACE CUTS-FRONT
0.	• AND,39,46,69,70,80.	:87	:THETACHECK=PHICHECK*DRF=GATE6
0.	• AND,39,46,47.	:88	:GOOD CHMBS. QUAD OK
40344.	• AND,71,72.	:89	:FLANGE CUTS
30430.	• AND,39,46,65,66,67,68.	:90	:TARGET TESTS=GOOD CHMBS ==> (TGT)
25931.	• AND,39,46,69,70.	:91	:THTCHK AND PHICMK=GOOD CHMBS==>(ANG CHK)
32166.	• AND,39,46.	:92	:DRF=CHKSUM ==> (GOOD CHMBS)
24766.	• AND,90,91.	:93	:TGT=ANG CHK ==> (GOOD EVENT)
0.	• AND,80,92.	:94	:ELASTIC. GOOD CHMBS
0.	• AND,80,93.	:95	:ELASTIC. GOOD EVENT
0.	• AND,47,94.	:96	:ELASTIC. GOOD EVENT. QUAD
11029.	• GAT,236,9739,9913.	:97	: -1.0 DEG
10042.	• GAT,236,9913,10007.	:98	: 0.0 DEG
9193.	• GAT,236,10007,10261.	:99	: 1.0 DEG
6293.	• B1,2,0.	:100	:MUON
0.	• GATE,1,1,-1.	:101	:SPARE
0.	• GATE,1,1,-1.	:102	:SPARE
0.	• GAT,1,1,-1.	:103	:SPARE
0.	• GAT,1,1,-1.	:104	:SPARE
0.	• GAT,1,1,-1.	:105	:SPARE
22077.	• AND,93,-100.	:106	:GOOD EVENT,PION
23034.	• AND,93,09.	:107	:GOOD EVENT,FLANGE
22020.	• AND,93,-100,09.	:108	:GOOD EVENT,FLANGE,PION==>(PION EVENT)
2746.	• AND,93,-100.	:109	:GOOD EVENT GARBAGE
0.	• AND,95,100.	:110	:ELASTIC,PION EVENT
22020.	• AND,100,-10.	:111	:PION EVENT -1/10
0.	• AND,100,10.	:112	:PION EVENT 1/10
5006.	• AND,111,97.	:113	:PION EVENT,-1/10,-1DEG
5620.	• AND,111,90.	:114	:PION EVENT -1/10 0DEG
4446.	• AND,111,99.	:115	:PION EVENT -1/10 +1DEG
0.	• AND,100,77.	:116	:PION EVENT AND BOX2
0.	• AND,100,70.	:117	:PION EVENT AND BOX3
66.	• AND,100,79.	:118	:PION EVENT AND BOX4
30541.	• AND,39,46,09.	:119	:GOOD CHMBS.FLSNGE
1009.	• AND,93,100.	:120	:MUON
0.	• AND,1,-1.	:121	:SPARE
0.	• AND,1,-1.	:122	:SPARE
0.	• AND,1,-1.	:123	:SPARE
0.	• AND,1,-1.	:124	:SPARE
0.	• AND,1,-1.	:125	:SPARE
0.	• AND,01,46	:126	:GATE FOR CH CAL
46459.	• IDR,1,-1.	:127	:LOOP 4 COUNTER (WHOOPEE WERE DONE)

Fig. II-7: (cont.)

II-7). The PID box consists of two indirect gates, one on the mean energy loss in scintillators S2 and S3, and one on the time of flight between S2 and S3. The PID test eliminates protons but not muons. The PID test constitutes the first loop of the test file.

If an event passes the PID test, the analyzer proceeds to calculate the positions in the front and rear multiwire proportional drift chambers from the time difference and time sum of the chamber signals. At this point, a number of chamber tests are performed (second loop of the test file). The tests consist of drift-time tests and drift-difference tests. The drift-time tests are gates (100 ns) on the drift times from the eight front and eight rear chamber planes (see test #'s 17-32 in Fig. II-7). The drift-time tests eliminate events which did not produce signals in one or more chamber planes. The drift-difference tests are applied to groups of four chamber planes, the front x planes, the front y planes, the rear x planes, and the rear y planes. These tests compare the positions calculated for the four chamber planes to a straight line trajectory. From this comparison, the drift-difference tests eliminate events for which two particles passed through the chambers simultaneously and pion events which created knock-on electrons with the group of four chamber planes. At this stage, an event has passed the PID test and chamber tests, and the analyzer has computed x_f , y_f , θ_f , ϕ_f , x_r , y_r , θ_r , ϕ_r .

The next step is the calculation of the quantities x_{tgt} , y_{tgt} , θ_{tgt} , ϕ_{tgt} , the incident momentum, the scattered momentum, and the scattering angle. The quantities at the scattering target are calculated using the measured positions and angles at the front chambers in

conjunction with the transport matrix of the spectrometer quadrupoles.
To first order

$$x_{tgt} = -x_f . \quad (II-1)$$

However, due to aberrations in the quadrupole fields, within the analyzer x_{tgt} , y_{tgt} , θ_{tgt} , and ϕ_{tgt} are calculated as polynomials of up to fourth order in the front chamber positions and angles [Bo-79]. From x_{tgt} , one can obtain the incident momentum.

$$x_{tgt} = D_c \cdot \delta_c , \quad (II-2)$$

where D_c is the dispersion of the channel (10 cm/%) and δ_c is the percent difference between the incident momentum for the event ($P_1(\text{event})$) and the central momentum of the channel (P_c , determined from the channel magnetic field settings).

$$\delta_c = \frac{P_1(\text{event}) - P_c}{P_c} . \quad (II-3)$$

The scattered momentum is determined, to first order, from the relation

$$x_r = -x_f + D_{sp} \cdot \delta_{sp} , \quad (II-4)$$

where D_{sp} is the dispersion of the spectrometer (4 cm/%) and δ_{sp} is the percent difference between the scattered momentum of the event

($P_f(\text{event})$) and the central momentum of the spectrometer (P_{sp} , determined from the spectrometer magnetic field settings).

$$\delta_{sp} = \frac{P_f(\text{event}) - P_{sp}}{P_{sp}} . \quad (\text{II-5})$$

After calculating the above quantities, the analyzer calls CALKIN, a subroutine to compute the missing mass of the event. Missing mass is the difference between the mass of the recoil nucleus and the mass of the nucleus before the collision (i.e., the excitation energy given to the nucleus). Thus,

$$Q = [(E_i(\text{event}) - E_f(\text{event}) + M)^2 - p^2]^{1/2} - M , \quad (\text{II-6})$$

where Q is the missing mass, M is the ground state mass of the target nucleus, p is the recoil momentum of the target nucleus, and $E_i(\text{event})$ ($E_f(\text{event})$) is the total energy of the incident (outgoing) event.

The final step of the analyzer is background rejection tests and passing the binned data to DSP for use in background rejection histograms and missing mass histograms. Four of the background rejection tests are gates on the calculated quantities x_{tgt} , y_{tgt} , θ_{tgt} , and ϕ_{tgt} . Histograms of these quantities aid in determining the lower and upper limits of the gates. Other background rejection tests include gates on the calculated quantities θ_{check} and ϕ_{check} . θ_{check} and ϕ_{check} are the difference between the angles measured at the front chambers and the angles calculated at the front focal plane from the information measured

at the rear chambers. Once again, histograms of θ_{check} and ϕ_{check} help to set the gate limits. The θ_{check} and ϕ_{check} tests eliminate $\sim 99\%$ of the muons resulting from the decay of pions after the front chambers. However, these tests will not eliminate muons due to pion decay before the front chambers or elastically scattered channel beam muons. The muon rejector (muon rejection test #100 in Fig. II-7) is used to eliminate $\approx 96\%$ of these muons. The missing mass histograms consist of the good pion events (test #108), the good events (test #93), and the one out of 10 or 100 fast cleared good pion events (test #112). The fast cleared missing mass histogram is used to monitor the fast clear system in order to prevent rejection of events from excited states.

III. DATA REDUCTION AND RESULTS

A. Missing mass histograms and targets

Pion elastic and inelastic scattering cross sections are calculated from the peak areas (counts) extracted from the missing mass histograms of good pion events. These histograms contain only those events which have passed test #108 of the test file (see Fig. II-7). Thus, the good pion events have passed the particle identification tests, the chamber tests, and the background rejection tests. Each missing mass histogram contains good pion events for the full angular acceptance of the spectrometer, $\theta_{\text{spect}} \pm \sim 1.5^\circ$, where θ_{spect} is the scattering angle for which the spectrometer has been set. Fig. III-1 shows a missing mass histogram for ${}^6\text{Li}(\pi^+, \pi^+)$ using a 205 mg/cm², 20 cm \times 10 cm sheet of enriched lithium metal ($> 98\%$ ${}^6\text{Li}$) for $T_\pi = 140$ MeV and $\theta_{\text{lab}} = 26^\circ$. Although the experimental resolution was not the best for the 205 mg/cm² target (240 keV full width at half maximum (FWHM)), the 0^+ , $T=1$, 3.563-MeV level is clearly resolved from the broad 2^+ , $T=0$, 4.25-MeV level and the large background due to the continuum of final states in the alpha-deuteron breakup of ${}^6\text{Li}$. Also clearly evident in the Q-value spectrum is the 3^+ , $T=0$, 2.185-MeV level. There is no indication of the 2^+ , $T=1$, 5.37-MeV or 1^+ , $T=0$, 5.65-MeV levels. (The 5.65-MeV level has never been observed in electron scattering [Be-82].) The discontinuity in the Q-value spectrum between the ground state and 2.185-MeV state is an artifact of the fast clear system used to veto 99 out of 100 events with

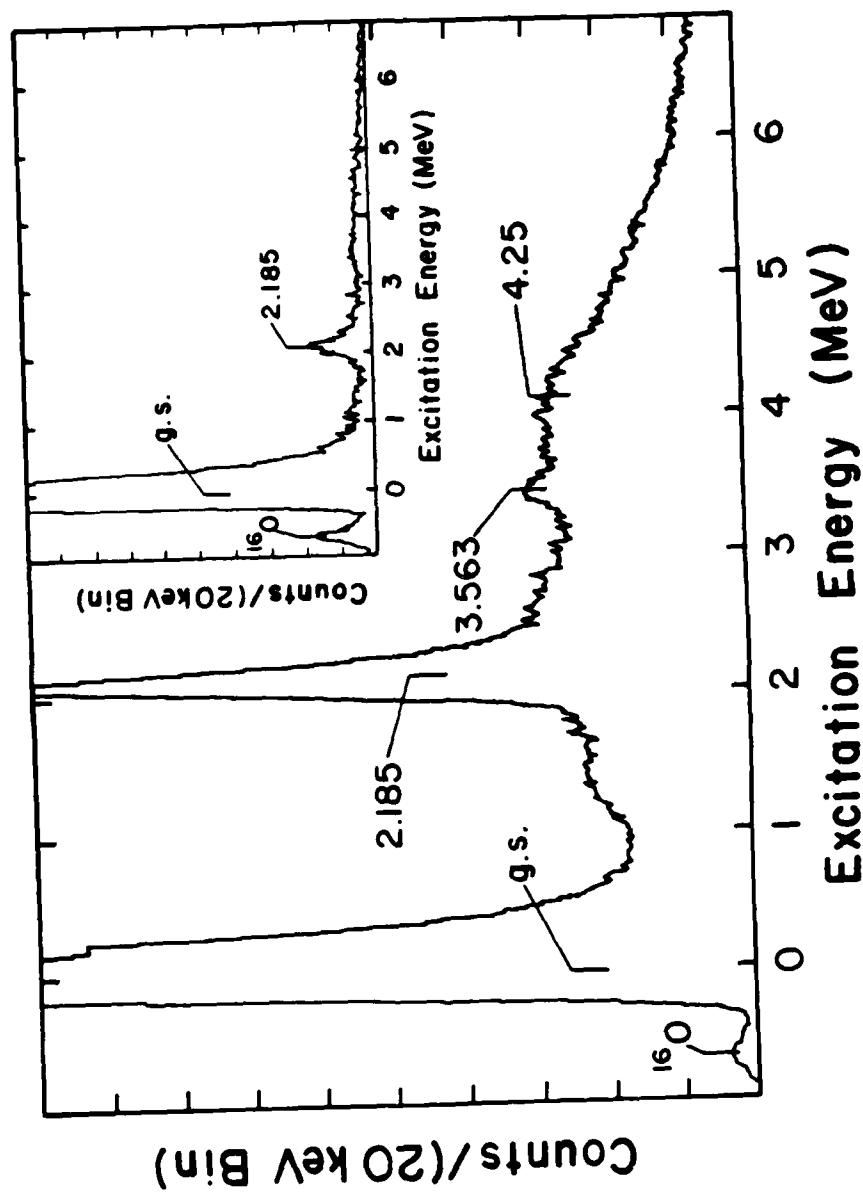


Fig. III-1: A π^+ energy-loss spectrum taken at $T_\pi = 140$ MeV and $\theta_{lab} = 26^\circ$ for which the fast clear system was used. The insert is the π^+ energy-loss spectrum without the use of the fast clear system.

a Q value below ≈ 1.2 MeV. The insert of Fig. III-1 shows the same missing mass histogram acquired without the use of the fast clear system and for a shorter period of data acquisition.

Four separate targets consisting of sheets of enriched lithium metal ($> 98\% \text{ } ^6\text{Li}$) fabricated by the Oak Ridge National Laboratory were used during the experiment. Two of the targets, with dimensions of $22.9 \text{ cm} \times 15.2 \text{ cm}$ and areal densities of 202 mg/cm^2 and 100 mg/cm^2 , were used for approximately one-half of the total data acquisition and contained no discernible contamination. The remaining two targets, with dimensions of $20 \text{ cm} \times 10 \text{ cm}$ and areal densities of 205 mg/cm^2 and 95 mg/cm^2 , were contaminated by exposure to the air during shipping. (Further contamination was prevented by handling the targets in a sealed glove bag filled with argon. Also, when not in use, the targets were stored in an evacuated canister.) Since lithium metal exposed to the air will form the compounds lithium hydroxide (LiOH) and lithium nitride (Li_3N), possible contaminants were oxygen, nitrogen, and hydrogen. The areal densities for the $20 \text{ cm} \times 10 \text{ cm}$ targets include corrections for these contaminants, as described in Sec. III-B.

Full-size targets for the target ladder are $22.9 \text{ cm} \times 15.2 \text{ cm}$. Two of the targets ($20 \text{ cm} \times 10 \text{ cm}$) were not full-size targets and care was taken to ensure proper normalization of the cross sections. The CH_2 targets used for absolute normalization (see Sec. III-C) were of the same dimensions as the ^6Li targets, and both the ^6Li and CH_2 targets were mounted in the target ladder in the same configuration. Furthermore, due to possible misalignment of the targets in the target ladder and the variation of the target area intercepted by the channel beam as

$\cos(\theta_{\text{target}})$ (θ_{target} is the angle between a perpendicular plane to the beam and the plane of the target), θ_{target} was set to bisect the central angle of the angular distributions acquired with the 20 cm \times 10 cm targets. For example, at $T_{\pi} = 120$ MeV the thick and thin 20 cm \times 10 cm targets were used for $\theta_{\text{lab}} = 21^{\circ}$ to 42° . Thus, θ_{target} was set to 16° (bisects the central angle of 32°) for each θ_{lab} . Such a procedure eliminated possible errors which could result from differing target areas intercepted by the beam as the target angle varied. Also, the central angle of the angular distribution was chosen to minimize straggling for the set of angles. For the two full-size targets, the target area was much greater than the channel beam area and the above precautions were not needed.

B. Extraction of peak areas

Peak areas for the elastic peak of ${}^6\text{Li}$, the first three excited states of ${}^6\text{Li}$, and the elastic peaks of the contaminants were extracted from the ${}^6\text{Li}(\pi^+, \pi^+)$ Q-value spectra using a lineshape oriented fitting program LOAF [Sm-78]. LOAF allows simultaneous fitting of a maximum of ten peaks, each with a separate lineshape. The peaks can be fit as "free" peaks (centroid of each peak is allowed to move independently) or as "delta" peaks (centroids of a group of peaks are constrained to have fixed separations but the position of the group of peaks may vary). Lineshapes are taken from a user-specified peak in the spectrum to be fitted. LOAF automatically determines the background as a polynomial of order zero to ten (the polynomial order is specified by the user) from

the displayed region of the histogram, or the user may fix the background by specifying a number of background points which LOAF then fits with a spline curve. For a displayed region of a Q-value spectrum, LOAF determines the best fit background and then subtracts this best fit background from the spectrum. The remaining spectrum is assumed to be peaks and is fitted with the user-specified lineshapes, where only the area and centroid of each peak are variable parameters. A disadvantage of this peak fitting procedure is that uncertainties for peak areas extracted from peaks strongly correlated with the background may be underestimated. Due to the relative ease of use and constant user interaction with the program LOAF, LOAF was used for the extraction of all peak areas, even though the weakly excited 3.563-MeV state lies on top of a large continuum background. However, to ensure that LOAF provided realistic uncertainties for the peak areas, one spectrum at each incident pion energy was fitted with another peak fitting routine [B1-84]. This alternate fitting program optimizes the background polynomial and peak parameters simultaneously; thus, the peak area errors contain any correlations between the background and peak parameters. Both fitting programs returned consistent peak areas and errors.

Due to the differences in recoil energies of different nuclei, contaminants in the ${}^6\text{Li}$ targets appear as separate peaks in the ${}^6\text{Li}(\pi^+, \pi^+')$ Q-value spectra. The centroids of these peaks allow determination of the types of contaminants, whereas the areas determine the quantity and thus the correct ${}^6\text{Li}$ target areal density. As a result of its light mass, the hydrogen contamination was easy to calculate. For both the thick and thin 20 cm \times 10 cm targets, the hydrogen peak was

fitted for all spectra where it was clearly resolvable from the ${}^6\text{Li}$ inelastic peaks. These hydrogen peak areas were used in conjunction with the $\pi^+ + p$ cross sections generated by the computer program CROSS [Bu-n.d.] to calculate an average target areal density due to hydrogen. The result was $< 1\%$ (by areal density) hydrogen contamination for the thick $20\text{ cm} \times 10\text{ cm}$ target and $\approx 5\%$ for the thin $20\text{ cm} \times 10\text{ cm}$ target. The elastic peaks of ${}^{16}\text{O}$ and ${}^{14}\text{N}$ were not separable within the elastic impurity peak appearing at the low excitation energy side of the ${}^6\text{Li}$ elastic peak (see Fig. III-1). However, since in some Q-value spectra the 6.13- and 6.92-MeV states of ${}^{16}\text{O}$ but no inelastic peaks of ${}^{14}\text{N}$ were observed, the heavy elastic impurity peak was assumed to be ${}^{16}\text{O}$. With this assumption, the extracted yields for the heavy impurity elastic peak resulted in smooth 120- and 180-MeV angular distributions whose shapes were in rough agreement with predicted $\pi^+ + {}^{16}\text{O}$ angular distributions. As for hydrogen, the ${}^{16}\text{O}$ elastic peak areas were used in conjunction with theoretical $\pi^+ + {}^{16}\text{O}$ cross sections (tested against the data of [Ho-80]) to calculate an average target areal density due to oxygen. The ${}^{16}\text{O}$ target areal density and the hydrogen target areal density resulted in total impurities of 2.3% and 18% for the thick and thin $20\text{ cm} \times 10\text{ cm}$ targets. Similar calculations assuming the heavy elastic impurity peak to be all nitrogen resulted in the same amount of total impurities to within $\pm 10\%$. In addition, a small amount of nitrogen contamination would negligibly affect the ${}^6\text{Li}$ inelastic cross sections ($< 1\%$) since all the (π^+, π^+') cross sections of ${}^{14}\text{N}$ are a factor of 100 to 1000 less than the elastic cross sections [Ge-83]. As a further check on the contaminant correction to the ${}^6\text{Li}$ target areal density, the differential

cross sections for the elastic scattering from ${}^6\text{Li}$ extracted from the contaminated and uncontaminated targets at the same incident pion energy and scattering angle were compared and found to agree within 2%. Fig. III-2 shows the fits from the program LOAF for two spectra acquired at $T_\pi = 120$ MeV and $\theta_{\text{lab}} = 27^\circ$, one with the contaminated thin $20\text{ cm} \times 10\text{ cm}$ target and the other with the thin $22.9\text{ cm} \times 15.2\text{ cm}$ target. Due to the large amount of contamination in the thin $20\text{ cm} \times 10\text{ cm}$ target (particularly, the broad hydrogen peak), this target was used only for the elastic and 2.185-MeV states of ${}^6\text{Li}$ at $T_\pi = 120$ MeV and $\theta_{\text{lab}} = 21^\circ$, 27° , 29° , and 32° , where the oxygen elastic was clearly resolved from the ${}^6\text{Li}$ elastic and the oxygen inelastics and hydrogen elastic appeared at 2.77 MeV and above in the Q-value spectra. No ${}^7\text{Li}$ impurity was observed in the spectra for any of the four targets.

To determine the areas for the elastic peak of ${}^6\text{Li}$ and the 3^+ peak, the Q-value spectra acquired without the fast clear system were fitted in the region between -1.5 MeV and 3.0 MeV with a first-order polynomial background and two peaks constrained to be at 0.0 and 2.185 MeV [Aj-84] (see Fig. III-2). Both the elastic and 3^+ peaks were fitted at each incident pion energy with their own lineshapes. To obtain areas for the 0^+ and 2^+ peaks, the Q-value spectra acquired with the fast clear system were fitted in the region between 1.4 MeV and 6.0 MeV with a third-order polynomial background and three peaks constrained to be at 2.185 MeV, 3.563 MeV [Aj-84], and 4.25 MeV. The lineshapes used for the 2.185- and 3.563-MeV peaks were extracted from the 3^+ in spectra acquired without the use of the fast clear system. Lineshapes were determined at each incident pion energy because the resolution varied with energy from

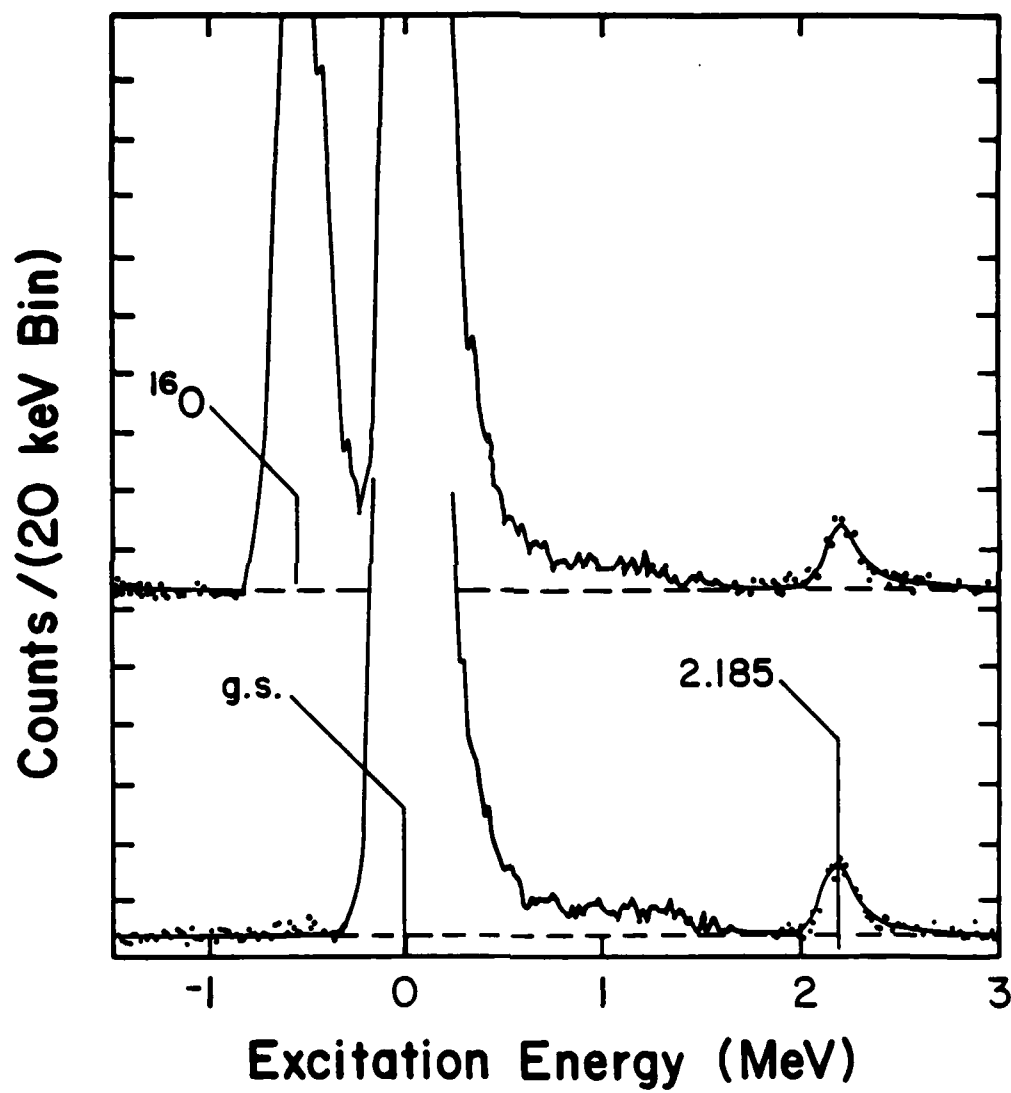


Fig. III-2: π^+ energy-loss spectra taken at $T_\pi = 120$ MeV and $\theta_{\text{lab}} = 27^\circ$. The top spectrum is from the contaminated 95 mg/cm^2 , $20 \text{ cm} \times 10 \text{ cm}$ target. The bottom spectrum is from the 100 mg/cm^2 , $22.9 \text{ cm} \times 15.2 \text{ cm}$ target. LOAF was used to fit the spectra.

200 keV (220 keV) FWHM at $T_\pi = 100$ MeV to 260 keV (260 keV) FWHM at $T_\pi = 260$ MeV for the thin (thick) targets. The lineshape used for the 2^+ state was constructed by folding the instrumental lineshape taken from the 3^+ with a Lorentzian of 680 keV FWHM. Both the position and natural width of the 2^+ level, 4.25 ± 0.02 MeV and 680 ± 20 keV, were determined from fits to several spectra where this state was predominant. Previous determinations from other experiments are 4.27 ± 0.04 MeV and 690 ± 120 keV (${}^6\text{Li}(e,e')$) [E1-69], 4.29 ± 0.02 MeV and 850 ± 50 keV (${}^9\text{Be}(p,\alpha)$) [De-83], 4.30 ± 0.1 MeV and 480 ± 80 keV (${}^9\text{Be}(p,\alpha)$) [De-83], and 4.3 ± 0.1 MeV and 600 ± 100 keV (${}^7\text{Li}({}^3\text{He},\alpha)$) [Sc-75]. Fig. III-3 shows the fits to several spectra taken at different incident pion energies and scattering angles.

The consistency of the fits to the various Q-value spectra was checked by extracting areas for 100 keV wide segments of background (automatically determined by the program LOAF) centered about 3.563 and 4.25 MeV. Plots of the background yields for both the 3.563- and 4.25-MeV segments result in smooth and continuous angular distributions at $T_\pi = 120$ and 180 MeV (see Figs. III-4 and III-5). Also, the background yields versus incident pion energy are smooth and continually increasing (see Figs. III-6 and III-7). Therefore, there is indication that the extraction of the peak areas from the large continuum background is consistent for different incident pion energies and scattering angles. However, this background check does not eliminate the possibility of an overall underestimation or overestimation of the background underneath the 3.563- and 4.25-MeV peaks.

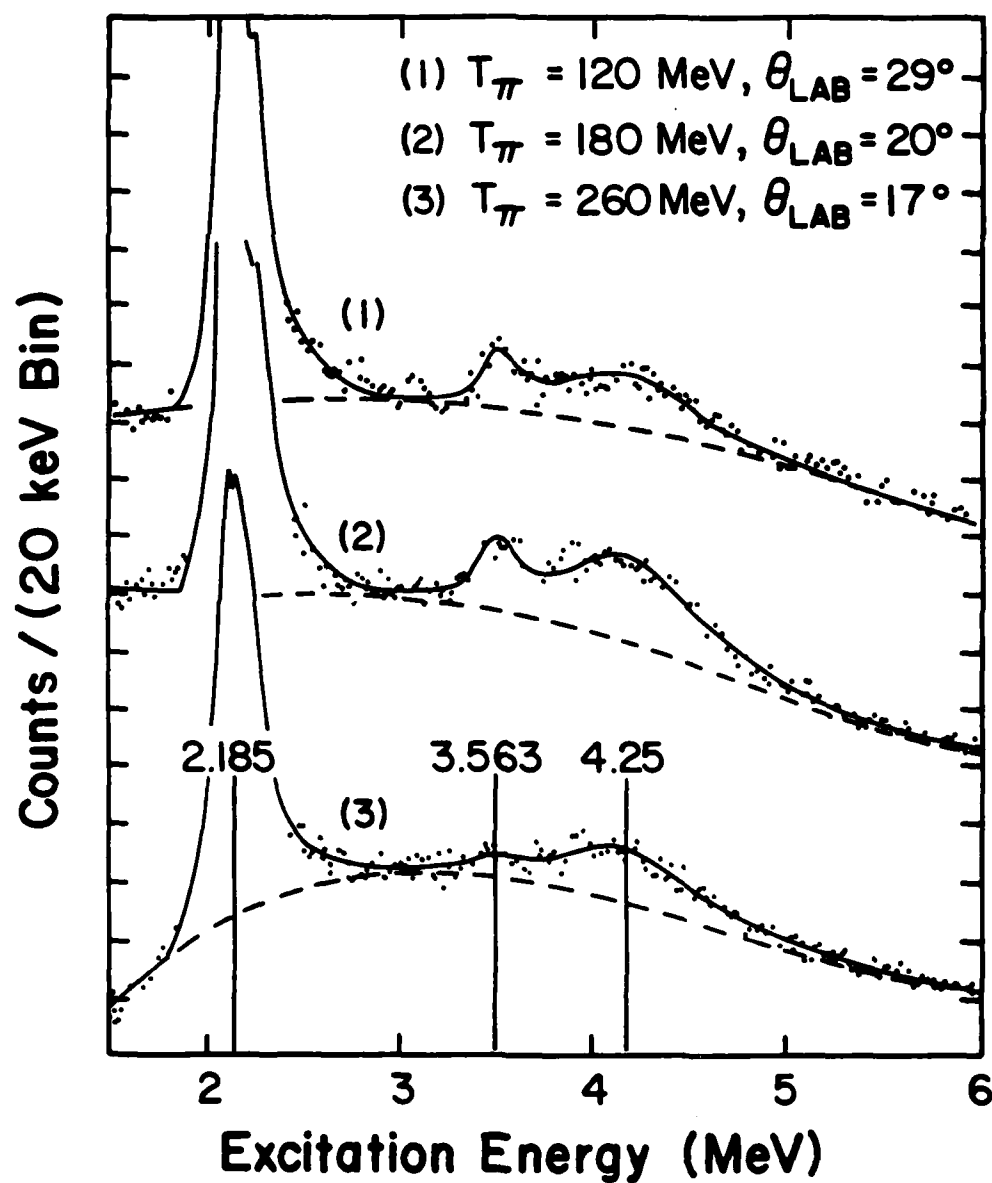


Fig. III-3: π^{+} energy-loss spectra and fits using the computer program LOAF.

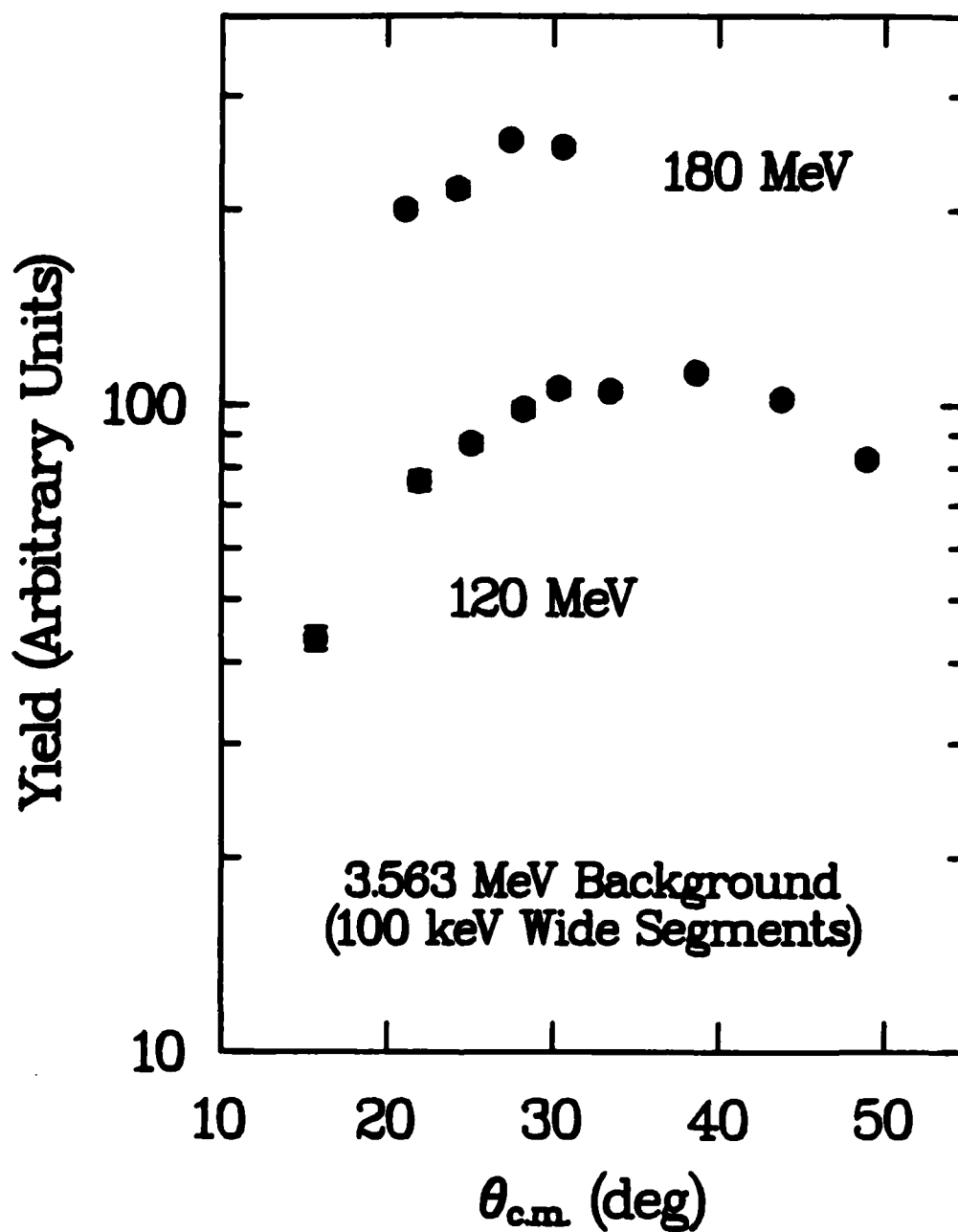


Fig. III-4: Angular distributions for 100 keV wide segments of background centered about 3.563 MeV.

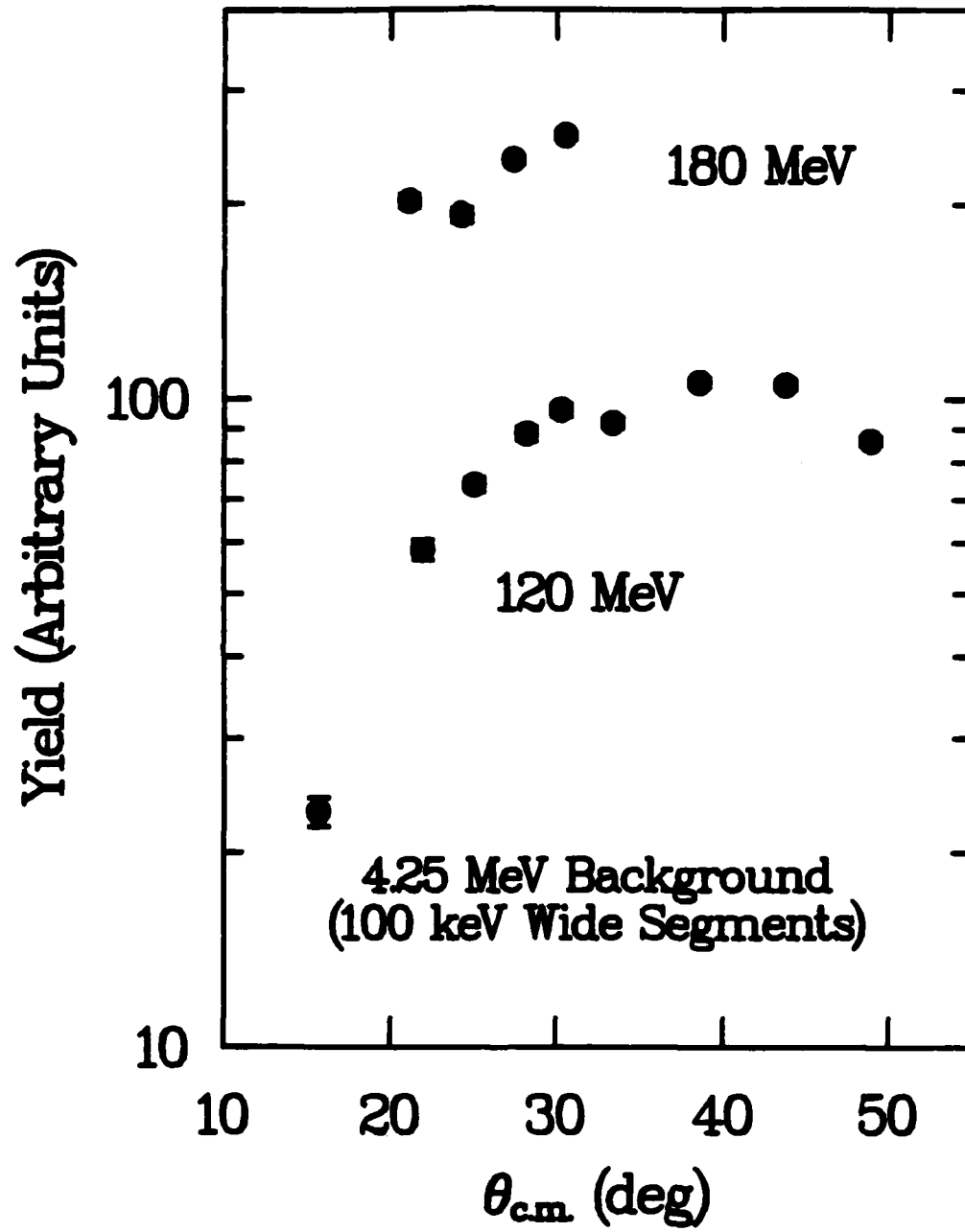


Fig. III-5: Angular distributions for 100 keV wide segments of background centered about 4.25 MeV.

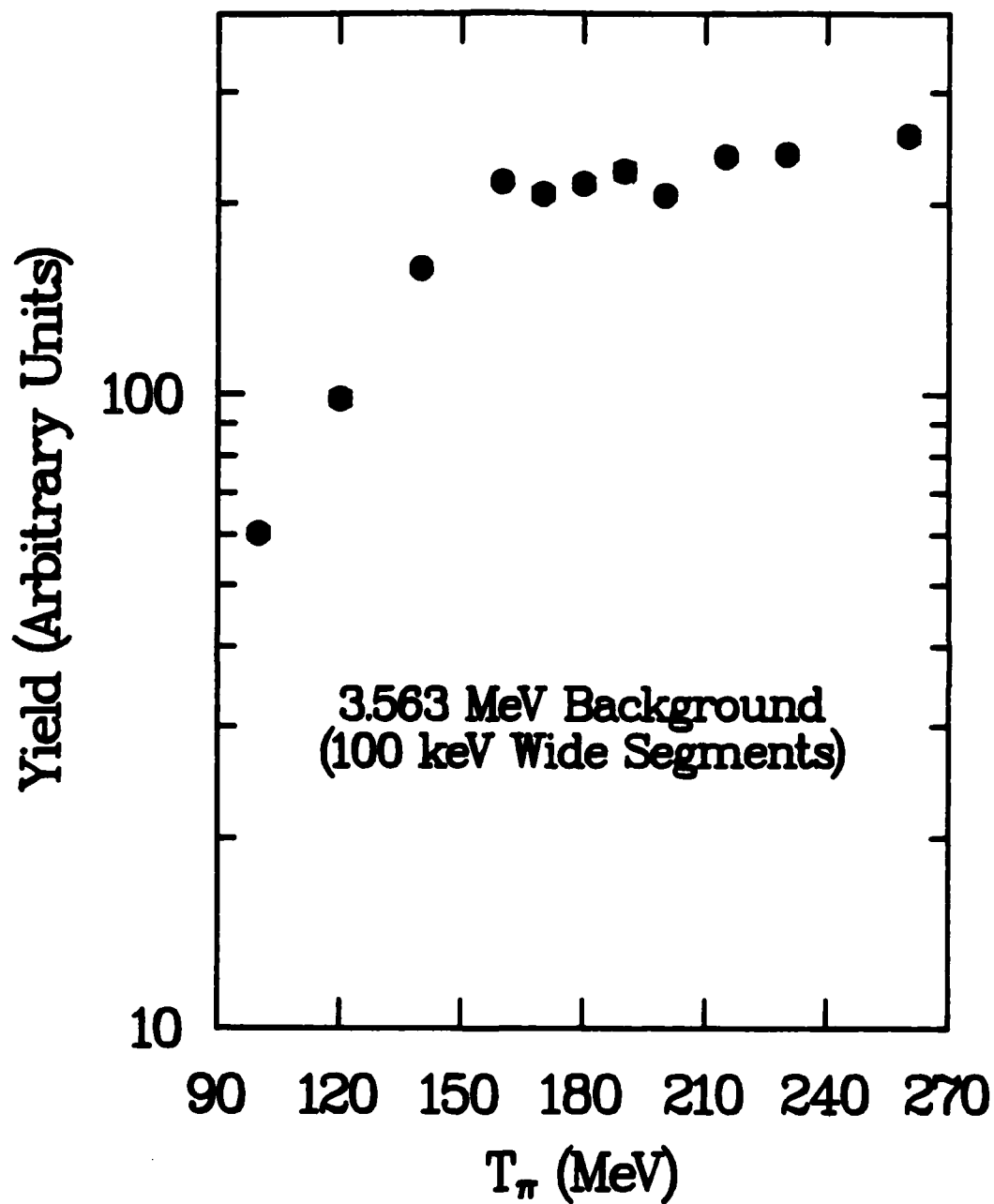


Fig. III-6: Background yields versus incident pion energy for 100 keV wide segments of background centered about 3.563 MeV. The data points correspond to a constant momentum transfer $q \approx 109$ MeV/c.

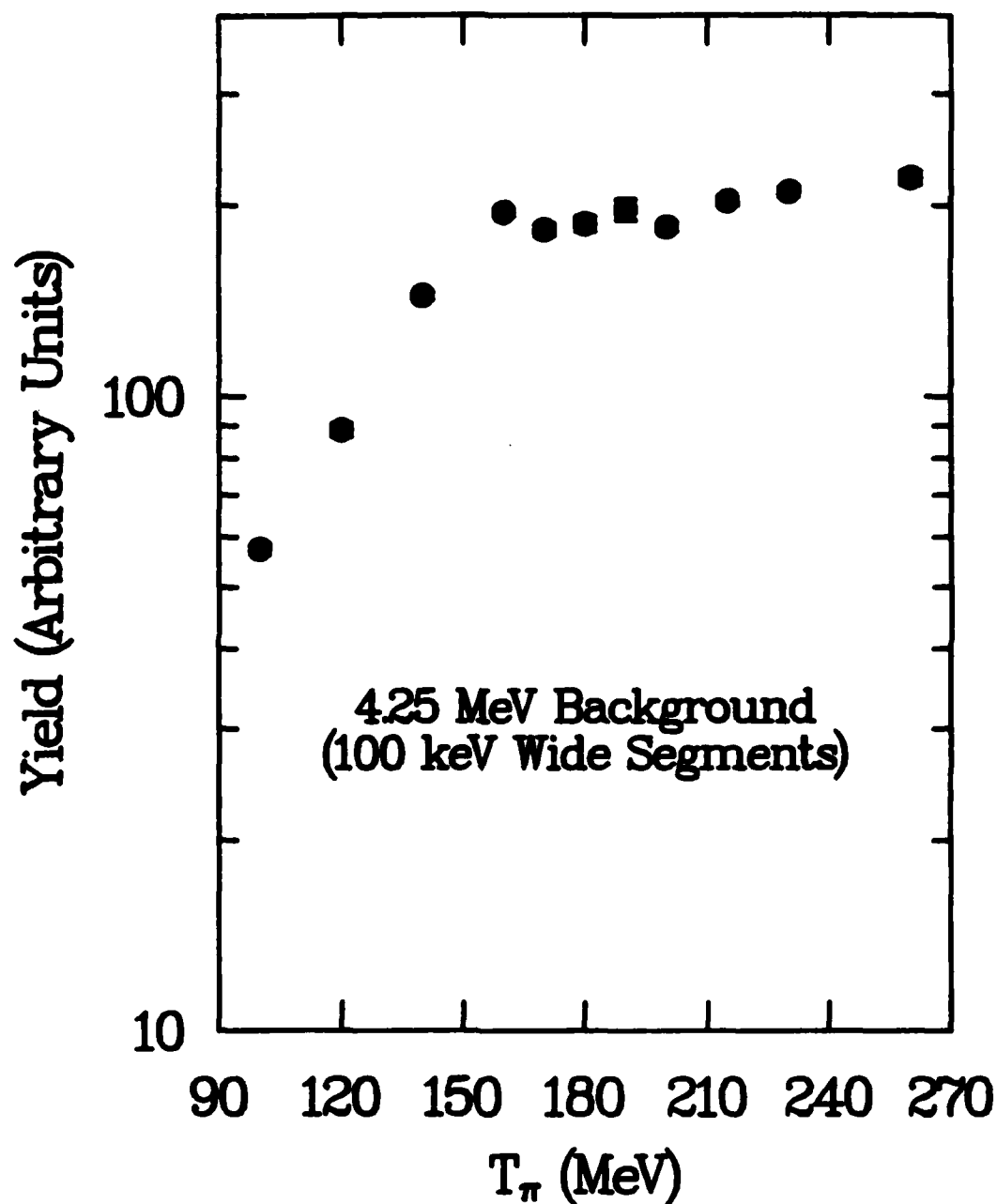


Fig. III-7: Background yields versus incident pion energy for 100 keV wide segments of background centered about 4.25 MeV. The data points correspond to a constant momentum transfer $q \approx 109$ MeV/c.

C. Cross section computation and errors

The differential scattering cross section in the center-of-mass system is given by

$$\frac{d\sigma}{d\Omega} = \frac{dNdt}{FdtNd\Omega} G, \quad (\text{III-1})$$

where $dNdt$ is the number of pions scattered at an angle θ into the solid angle $d\Omega$ in the time interval dt , Fdt is the number of pions crossing a unit area perpendicular to the channel beam in the time interval dt , N is the number of independent scattering centers in the target which are intercepted by the beam, and G is the Jacobian of the transformation from the laboratory to the center-of-mass system. $dNdt$ is given by the extracted peak area from a Q -value spectrum corrected for the inefficiencies of the EPICS data acquisition system.

$$dNdt = (\text{Peak Area}) \cdot CF, \quad (\text{III-2a})$$

where

$$CF = \frac{1}{CLT} \times \frac{1}{DREFF} \times \frac{1}{CHEFF} \times \frac{1}{LE} \times \frac{1}{SF} \times \frac{1}{SACORR}. \quad (\text{III-2b})$$

CLT is the computer live time as discussed in Sec. II-C. $DREFF$ is the drift efficiency of the multiwire proportional drift chambers and corrects for those events producing signals in all chamber planes but not

passing the drift-difference tests. CHEFF is the chamber efficiency and is the product of the sixteen individual chamber efficiencies, each given by

$$\text{CHEFF}_i = \frac{\text{All Chambers OK}}{\text{All Chambers but } i \text{ OK}} \quad (\text{III-3})$$

LE is the fraction of analyzed events. For on-line data acquisition in the MAY PROCESS mode, $LE < 1.0$. However, all data tapes are replayed in the MUST PROCESS mode so that $LE = 1.0$ provided there are no input/output tape errors. SF corrects for the pions that decay after the scattering target and before scintillator S3.

$$SF = \exp(-t/\tau') \quad (\text{III-4a})$$

where

$$t = \frac{\gamma L m_\pi}{p_\pi} \quad (\text{III-4b})$$

$$\tau' = \gamma \tau_\pi \quad (\text{III-4c})$$

p_π is the relativistic momentum of the pion, m_π is the rest mass of the pion, τ_π is the mean lifetime of the pion, $\gamma = 1/(1-v^2/c^2)^{1/2}$, and L is the path length from the scattering target to S3 which is corrected to first order in δ_{sp} for varying path lengths, $L = (12.28 - 0.035 \cdot \delta_{sp})$ meters. SACORR is a correction factor for the variation of the spectrometer's solid angle as a function of δ_{sp} . This correction factor

is determined by measuring the yield of a state (usually an elastic peak) for $-6\% < \delta_{sp} < 6\%$. δ_{sp} is varied by varying the spectrometer field settings. For all of the experimental runs, the spectrometer quadrupole and dipole magnetic fields were set to values such that pions exciting the 3.563-MeV level had the same δ_{sp} , where δ_{sp} was chosen to correspond to the flat region of the spectrometer's solid angle variation versus δ_{sp} curve (acceptance curve). This procedure minimized solid angle correction errors. Fdt is given by the relation

$$Fdt = \frac{\text{Monitor} \cdot \cos(\theta_{\text{target}}) \cdot \xi}{a}, \quad (\text{III-5})$$

where Monitor indicates the number of scaled ICl, BOT, or IACM02 pulses, $\cos(\theta_{\text{target}})$ corrects for the scattering target not being perpendicular to the channel beam, a is the target area intercepted by the beam, and ξ is a proportionality factor since the beam monitors are only relative monitors of the pion current. Lastly,

$$N = a \cdot n \cdot d, \quad (\text{III-6a})$$

with a the target area intercepted by the beam, d the target thickness, and n the number of scattering centers per unit volume,

$$n = \frac{N_o \rho}{A}. \quad (\text{III-6b})$$

N_0 is Avagadro's number, ρ is the target density, and A is the mass of the target in grams/mole. Combining Eqs. (III-1 to III-6),

$$\frac{d\sigma}{d\Omega} = \frac{G \cdot (\text{Peak Area}) \cdot \text{NORM} \cdot A}{N_0 \cdot \text{areal density} \cdot \xi \cdot d\Omega}, \quad (\text{III-7})$$

where $\text{NORM} = \text{CF}/(\text{Monitor} \cdot \cos(\theta_{\text{target}}))$ and the areal density is $d \cdot \rho$. Since neither ξ nor $d\Omega$ are known, the normal procedure is to determine the absolute magnitude of the differential scattering cross section by measuring a known differential scattering cross section. Thus, for each incident pion energy, spectra were accumulated for $\pi^+ + p$ scattering with CH_2 targets of the same dimensions as the ${}^6\text{Li}$ targets. Using the Coulomb-corrected phase-shift predictions from the computer code CROSS [Bu-n.d.], which uses the phase shifts of Rowe, Salomon, and Landau [Ro-78], to determine $d\sigma/d\Omega_H$, from Eq. (III-7)

$$\xi d\Omega = \frac{G_H \cdot (\text{Peak Area})_H \cdot \text{NORM}_H \cdot A_H}{N_0 \cdot (\text{areal density})_{\text{CH}_2} \cdot d\sigma/d\Omega_H} \times \frac{14}{2}, \quad (\text{III-8})$$

where the $14/2$ corrects for one mole of CH_2 containing two grams of hydrogen and twelve grams of carbon. Inserting Eq. (III-8) into Eq. (III-7) yields the expression for the absolute differential scattering cross section

$$\left(\frac{d\sigma}{d\Omega}\right)_{6\text{Li}} = \frac{G_{6\text{Li}}}{G_H} \times \frac{(\text{Peak Area})_{6\text{Li}}}{(\text{Peak Area})_H} \times \frac{(\text{NORM})_{6\text{Li}}}{(\text{NORM})_H} \times$$

$$\frac{(\text{areal density})_{\text{CH}_2}}{(\text{areal density})_{\text{Li}}} \times \left(\frac{d\sigma}{d\Omega}\right)_H \times \frac{12}{14} . \quad (\text{III-9})$$

Eq. (III-9) reveals the possible sources of error in the differential scattering cross sections. The error bars presented in the figures and table are errors due only to the statistical and fitting errors in the extracted peak areas estimated by the computer program LOAF. Additional total uncertainties are estimated to be $\pm 7\%$ due to uncertainties of $\pm 3\%$ in chamber efficiencies, $\pm 3\%$ in pion survival fraction (from the path length corrections), $\pm 2\%$ in the spectrometer's solid angle variation with momentum in the spectrometer (probably overestimated since the pion events of the elastic and inelastic peaks in the ${}^6\text{Li}$ Q-value spectra had δ_{sp} 's corresponding to the flat region of the spectrometer's acceptance curve), $\pm 3\%$ in channel beam monitoring, and $\pm 3\%$ in the normalization to π^+ elastic scattering from hydrogen. Furthermore, the data for the 3.563- and 4.25-MeV states contain systematic errors of $\pm 15\%$ and $\pm 10\%$, respectively, due to the uncertainty in the fitting of the large continuum background and the uncertainty in the position and width of the 2^+ state. These systematic errors were inferred from the fitting program LOAF by varying the order of the polynomial fit to the background, and by varying the position and width of the 2^+ state from 4.23 to 4.27 MeV and 660 to 700 keV.

D. Data

The data are presented in Tables A-1 through A-4 in Appendix A and in Figs. III-8 through III-15. For all figures, the results of multiple measurements at a given pion energy and scattering angle are plotted as a single data point which is the weighted average of the multiple measurements. The incident pion energies and scattering angles at which the data were acquired are the result of the main goal of the experiment--the measurement of a detailed constant- q excitation function for π^+ inelastic scattering to the 3.563-MeV state of ${}^6\text{Li}$. The incident pion energies range from 100 MeV to 260 MeV, thus covering the lower energy region through the upper energy region of the $\Delta(1232)$ resonance. $T_\pi = 100$ MeV is also the lowest pion energy normally used for most experiments at EPICS due to the decreased incident pion flux, decreased pion survival fraction in the spectrometer and experimental time limitations. $T_\pi = 260$ MeV is also not the highest usable pion energy, but higher energies were not feasible for this experiment because of the rapidly decreasing scattering cross section for the 3.563-MeV state at $T_\pi > 230$ MeV. Except for $T_\pi = 120$ and 180 MeV, there are data at only one scattering angle for each incident pion energy. The scattering angles correspond to a constant momentum transfer of $q \approx 109$ MeV/c, with an error in q of $\leq 7\%$. This momentum transfer was determined during on-line data acquisition from the apparent maximum of the angular distribution at $T_\pi = 120$ MeV for π^+ inelastic scattering to the 3.563-MeV level. However, after subsequent off-line data analysis, the maximum of the 120 MeV angular distribution occurs at $\theta_{\text{lab}} \approx 27^\circ$ (the midpoint of

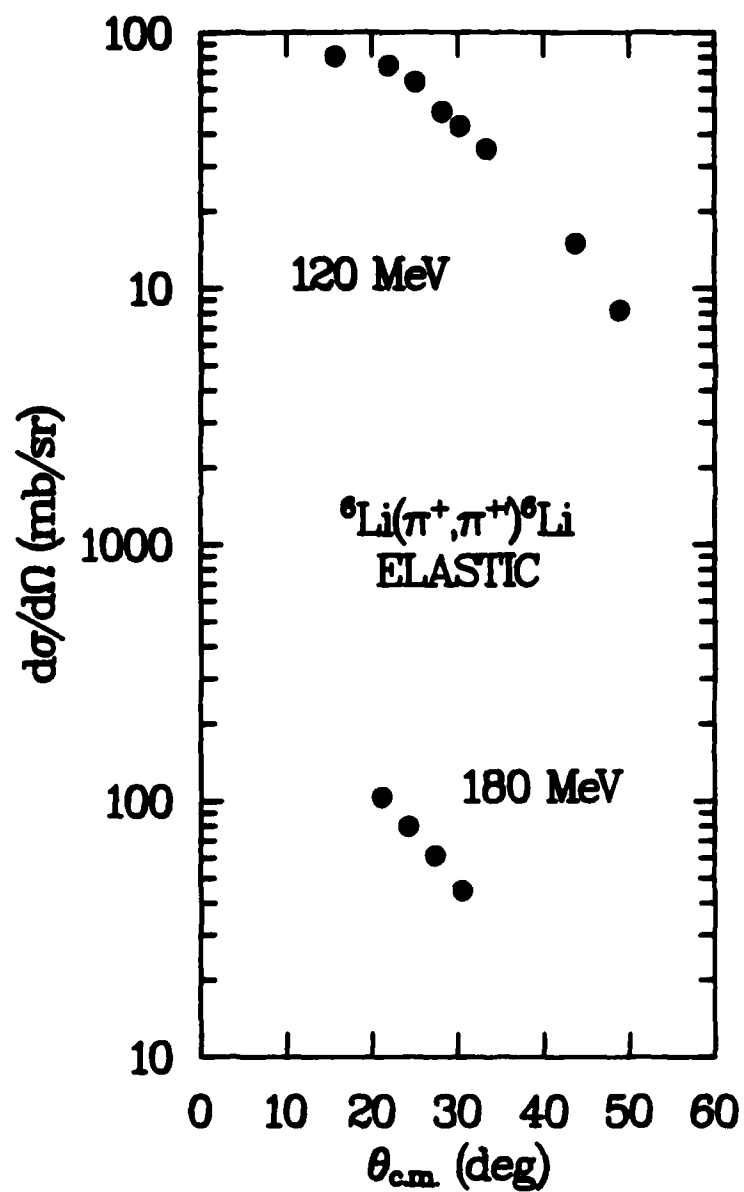


Fig. III-8: Differential cross sections for π^+ elastic scattering for ${}^6\text{Li}$ for $T_\pi = 120$ and 180 MeV.

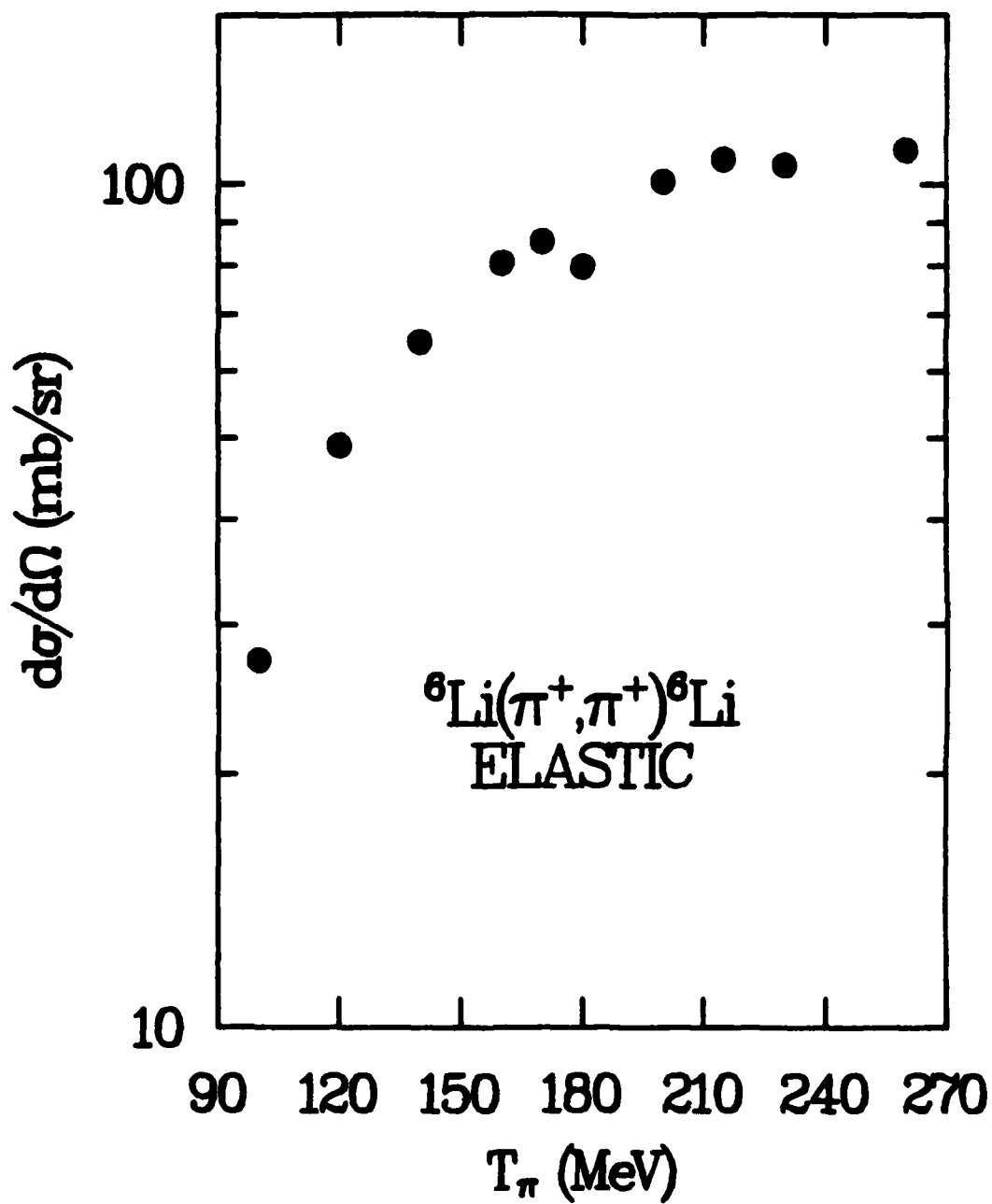


Fig. III-9: Differential cross sections for π^+ elastic scattering for ${}^6\text{Li}$ at a constant $q \approx 109 \text{ MeV/c}$.

the three highest data points in Fig. III-14), yielding a $q \approx 101$ MeV/c. No corrections have been made to the data for the variations in q . Such corrections result in small changes in the differential scattering cross sections for the 3.563-MeV state, but not for the elastic and 2.185- and 4.25-MeV states (discussed below). $T_\pi = 120$ and 180 MeV were chosen as the incident pion energies for the partial angular distributions in order to have angular distributions off and on the peak of the $\Delta(1232)$ resonance.

Fig. III-8 shows the differential cross sections for π^+ elastic scattering from ${}^6\text{Li}$ at $T_\pi = 120$ and 180 MeV. Fig. III-9 shows differential cross sections for $100 < T_\pi < 260$ MeV and $q \approx 109$ MeV/c. The excitation function continually increases with increasing incident pion energy, a characteristic feature for elastic scattering of a strongly absorbed probe [Bl-66]. The dip in the data curve at $T_\pi = 180$ MeV is partially a result of the momentum transfer being approximately 5% too high ($q \approx 114$ MeV/c). Extrapolation to $q \approx 109$ MeV/c moves the $T_\pi = 180$ MeV data point from 80 mb/sr to 90 mb/sr.

The differential cross sections for π^+ inelastic scattering to the 3^+ , $T=0$, 2.185-MeV level at $T_\pi = 120$ and 180 MeV are shown in Fig. III-10. Within the angular range measured, the angular distributions have the shape expected for a strong transition in the 1p shell in which the dominant transition amplitude is for $J=2$, $L=2$, $S=0$ (J is the total angular momentum transfer, L is the orbital angular momentum transfer, and S is the spin angular momentum transfer) [Le-80]. Fig. III-11 presents the differential cross sections for $100 < T_\pi < 260$ MeV and $q \approx 109$ MeV/c. The excitation function continually increases with

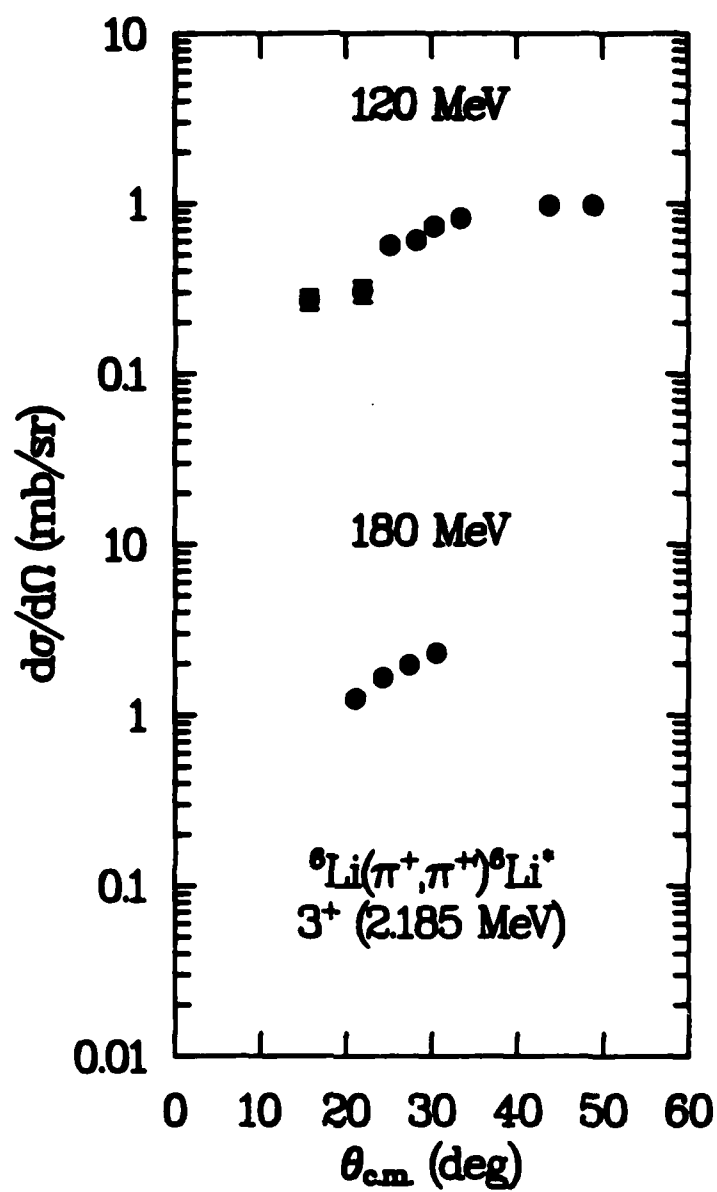


Fig. III-10: Angular distributions for π^+ inelastic scattering to the 3^+ , $T=0$, 2.185-MeV state of ${}^6\text{Li}$ for $T_\pi = 120$ and 180 MeV.

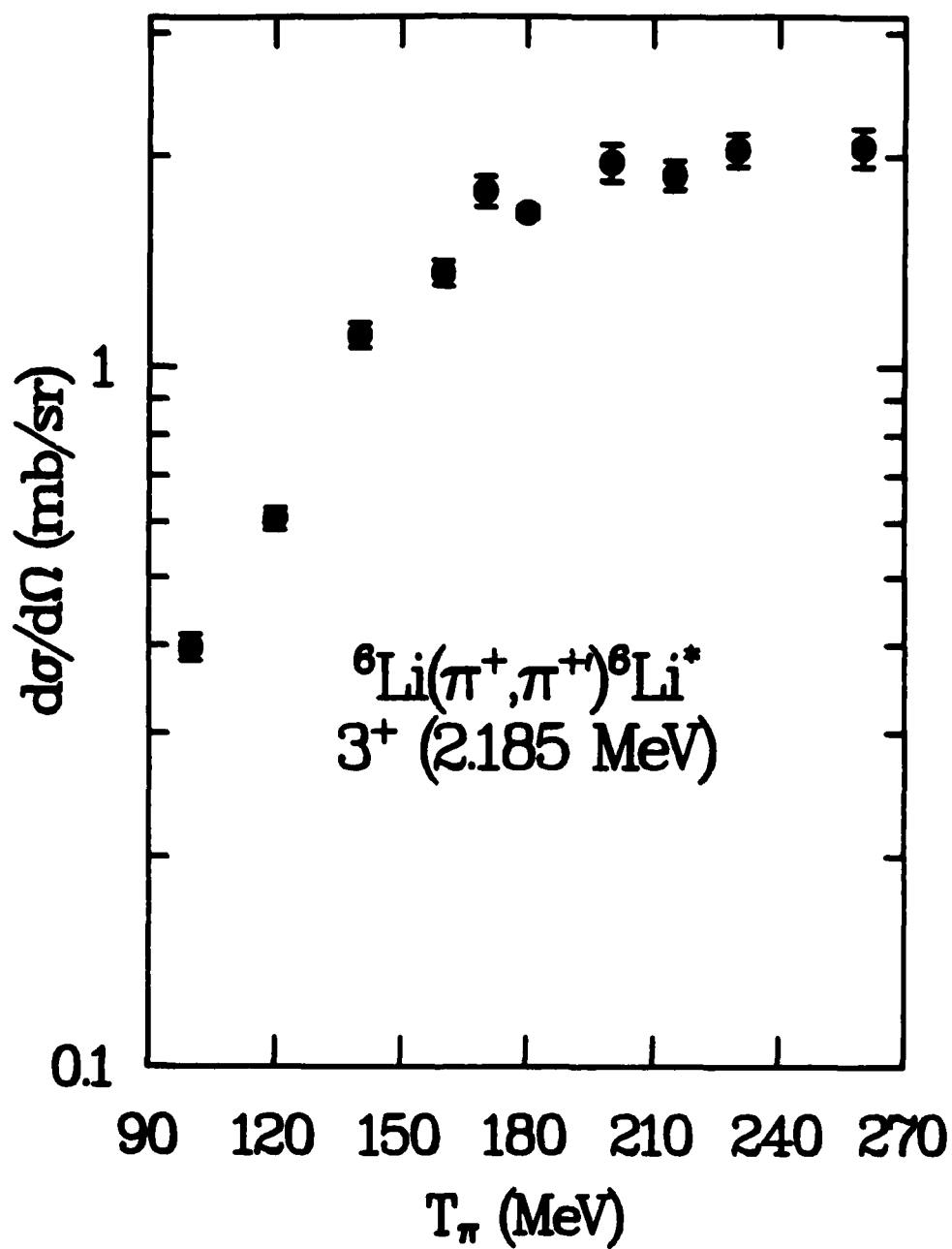


Fig. III-11: Differential cross sections for π^+ inelastic scattering to the 3^+ , $T=0$, 2.185-MeV state of ${}^6\text{Li}$ at a constant $q \approx 109 \text{ MeV/c}$.

increasing incident pion energy as expected for this natural-parity, $\Delta S=0$, transition (see Chap. 1).

Fig. III-12 shows the differential cross sections for π^+ inelastic scattering to the 2^+ , $T=0$, 4.25-MeV level at $T_\pi = 120$ and 180 MeV. The shape of the angular distributions are the same as for the inelastic transition to the 2.185-MeV state, consistent with the predictions of Lee and Kurath [Le-80]. This is also consistent with the electron scattering form factors for both natural-parity transitions to the 2.185- and 4.25-MeV levels. The form factors have the same dependences on the momentum transfer [Be-63]. Fig. III-13 presents the excitation function taken at $q \approx 109$ MeV/c. As for the 2.185-MeV state, the energy dependence is an increasing function of the incident pion energy. The fluctuations in the data curve are partially the result of variations in q . For example, the $T_\pi = 180$ MeV data point corresponds to $q \approx 113$ MeV/c. Extrapolation to $q \approx 109$ MeV/c moves the data point from 0.7 mb/sr to 0.6 mb/sr. Also, the fluctuations are not as great as they appear in Fig. III-13 when one accounts for the uncertainties discussed in Sec. III-C.

The differential cross sections for π^+ inelastic scattering to the 0^+ , $T=1$, 3.563-MeV state are presented in Figs. III-14 and III-15. The 120-MeV angular distribution peaks at an angle ($\theta_{c.m.} \approx 28^\circ$) smaller than the peaks ($\theta_{c.m.} > 45^\circ$) of the 120-MeV angular distributions for the 2.185- and 4.25-MeV states. Such a result is expected for this $J=1$, $L=0$, $S=1$ transition [Le-80]. The excitation function increases from $T_\pi = 100$ to 190 MeV and then decreases. A direct comparison to the excitation function for π^\pm inelastic scattering to the 15.11-MeV state of ^{12}C or to

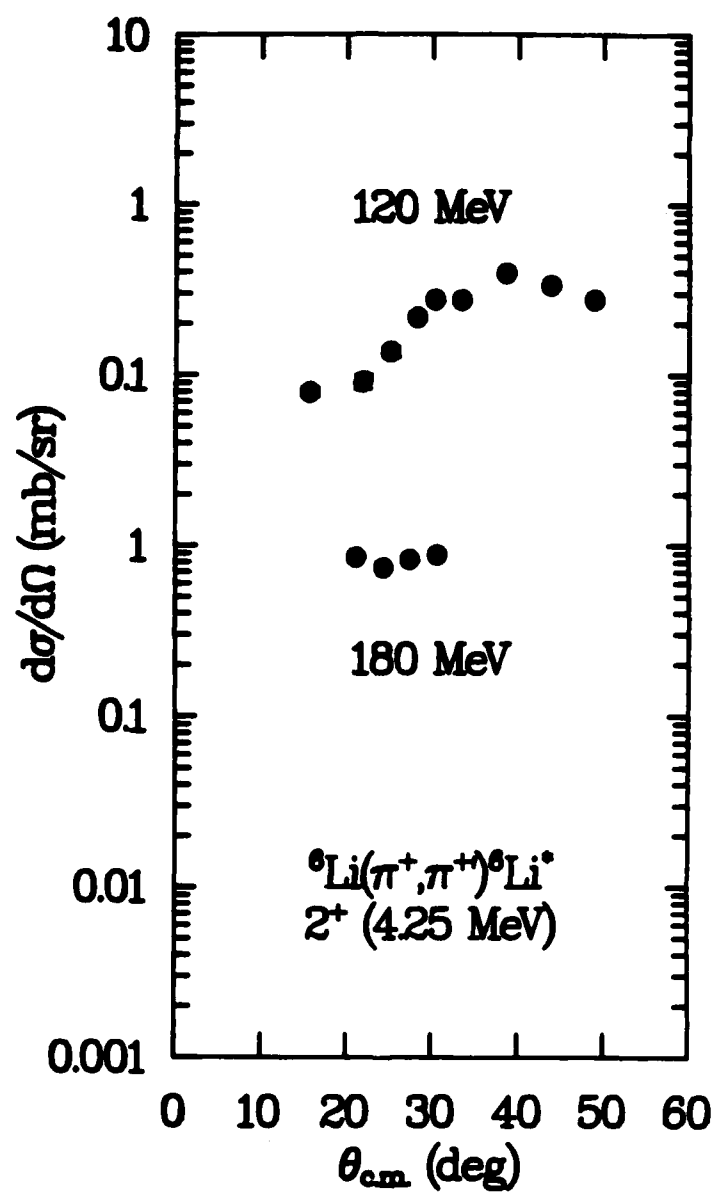


Fig. III-12: Angular distributions for π^+ inelastic scattering to the 2^+ , $T=0$, 4.25-MeV state of ${}^6\text{Li}$ for $T_\pi = 120$ and 180 MeV.

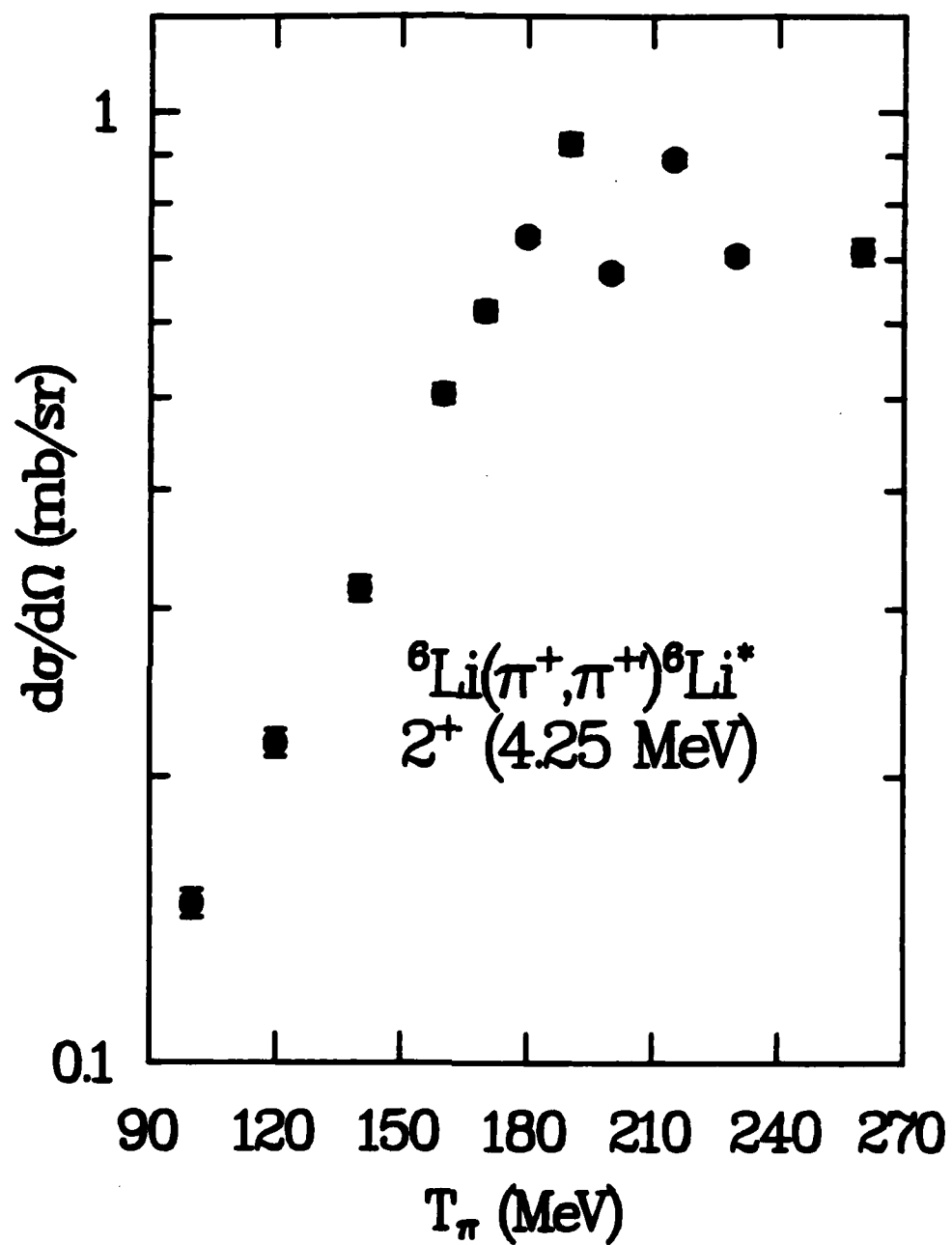


Fig. III-13: Differential cross sections for π^+ inelastic scattering to the 2^+ , $T=0$, 4.25-MeV state of ${}^6\text{Li}$ at $q \approx 109 \text{ MeV/c}$.

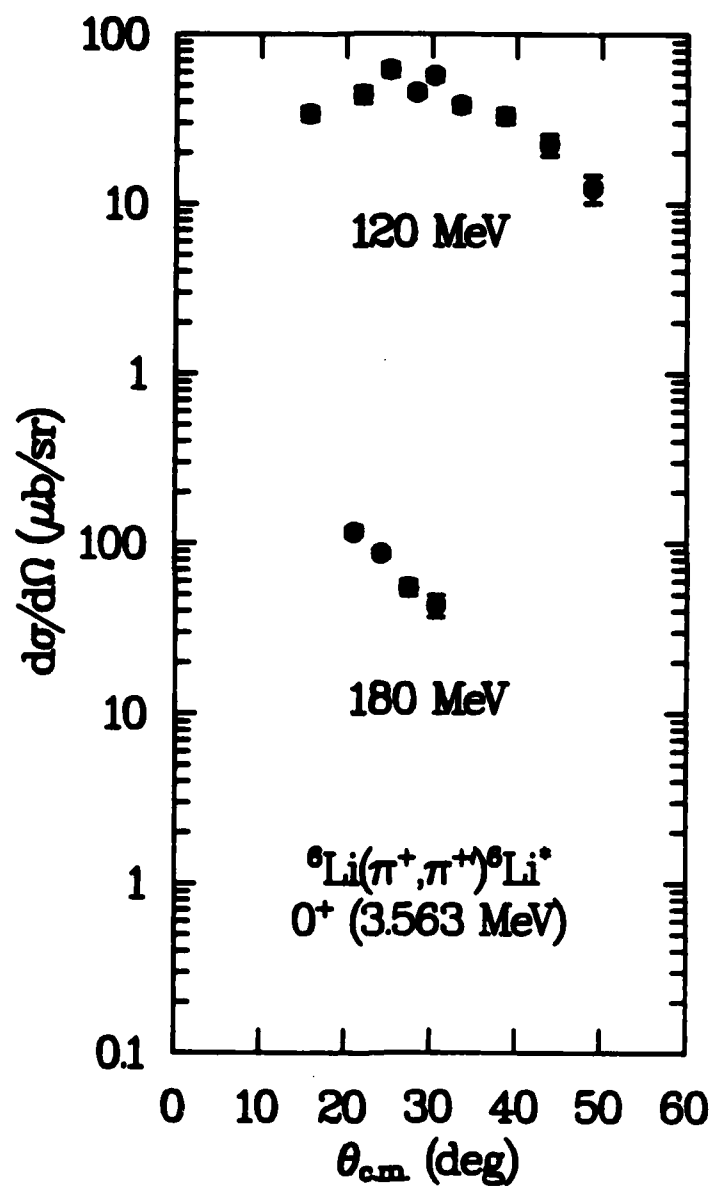


Fig. III-14: Angular distributions for π^+ inelastic scattering to the 0^+ , $T=1$, 3.563-MeV state of ${}^6\text{Li}$ for $T_\pi = 120$ and 180 MeV.

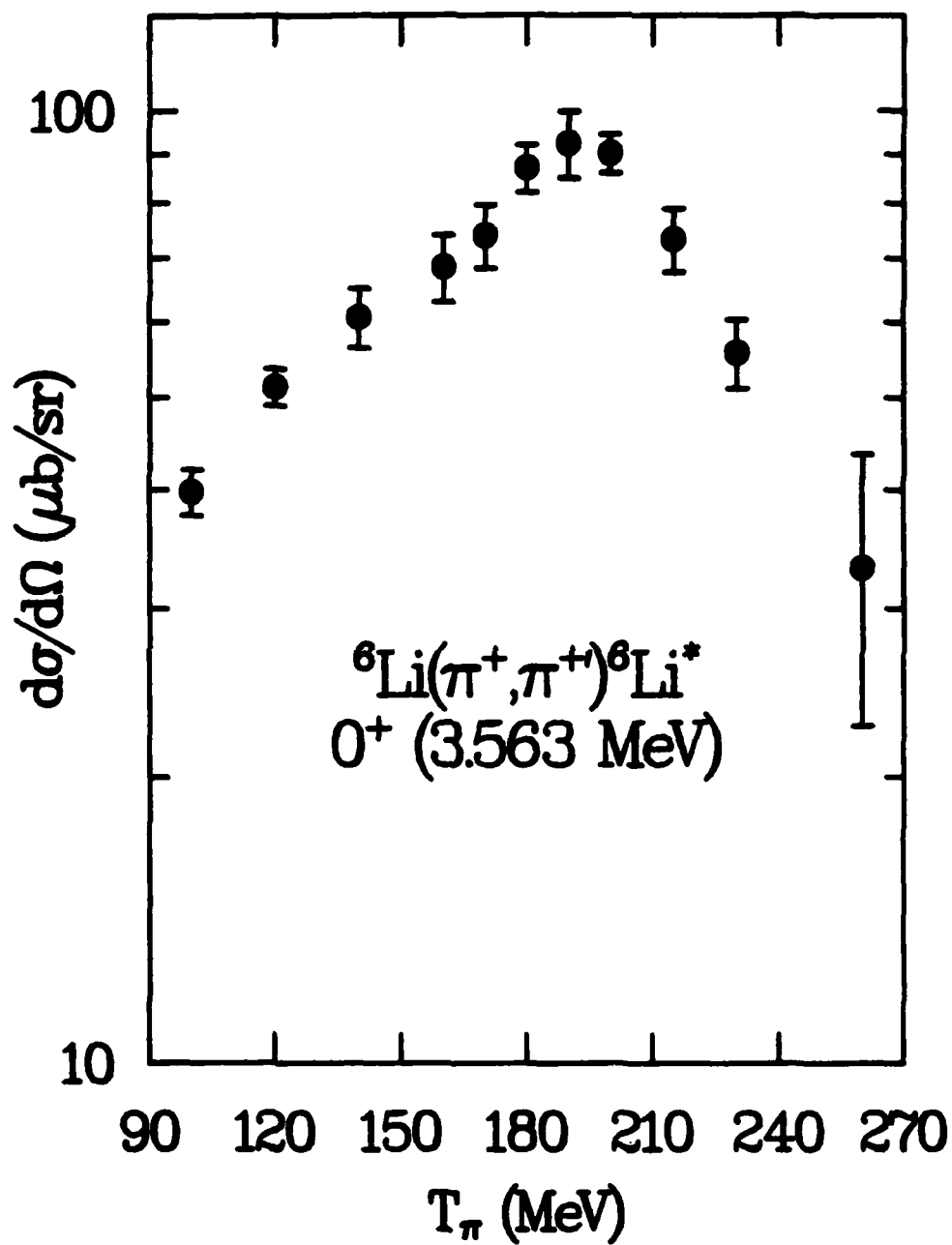


Fig. III-15: Excitation function at a constant $q \approx 109 \text{ MeV/c}$ for π^+ inelastic scattering to the 0^+ , $T=1$, 3.563-MeV state of ${}^6\text{Li}$.

$\sin^2\theta$ (see Chap. I) is not meaningful because of distortion effects of the incident pion wave function. Further discussion of the excitation function is given in Chap. V.

IV. THEORY

A proper understanding of pion-nucleus (πA) scattering data would require theoretical methods incorporating relativistic scattering techniques, since πA interactions involve both the absorption and production of pions. However, at present, there are almost no systematic relativistic theories available. The best theoretical tool is the non-relativistic multiple-scattering formalism developed by Watson and others in the 1950's [Fr-53,Fr-56,Wa-57,Wa-58], along with corrections for relativistic kinematics. The nonrelativistic multiple-scattering formalism leads quite clearly to the lowest-order result for the optical potential for πA elastic scattering and the transition amplitude for πA inelastic scattering. (An optical potential is a potential involving the projectile (pion) variables only and, when used in a one-particle Schrödinger equation for the projectile (Klein-Gordon equation for the pion), yields the solution to the multiple-scattering problem for projectile-nucleus (πA) elastic scattering.) The lowest-order results for the optical potential and transition amplitude involve the basic pion-nucleon (πN) T matrix and the nuclear ground state and transition densities, respectively, and have been successful as lowest-order approximations to the physics of πA elastic and inelastic scattering in the medium-energy range ($100 < T_\pi < 300$ MeV).

A. Nonrelativistic multiple-scattering formalism

For a pion incident on a nucleus of A nucleons, the Hamiltonian is

$$H = H_0(\vec{r}_1, \vec{r}_2, \dots, \vec{r}_A; \vec{r}) + V(\vec{r}_1, \vec{r}_2, \dots, \vec{r}_A; \vec{r}) , \quad (\text{IV-1a})$$

with

$$H_0 = H_N(\vec{r}_1, \vec{r}_2, \dots, \vec{r}_A) + K_\pi(\vec{r}) , \quad V = \sum_{i=1}^A v_i(\vec{r}, \vec{r}_i) . \quad (\text{IV-1b})$$

H_N is the nuclear Hamiltonian for A nucleons including the nuclear recoil (spin and isospin degrees of freedom are not shown explicitly), K_π is the kinetic energy operator for the pion, and v_i is the potential interaction operator between the pion and the i th nucleon. The variables $\vec{r}_1, \dots, \vec{r}_A$ refer to the nucleon coordinates and \vec{r} refers to the pion coordinate. The Lippmann-Schwinger equation for the πA transition operator T , is

$$T = V + V G_0 T = \sum_{i=1}^A v_i + \sum_{i=1}^A v_i G_0 T , \quad (\text{IV-2a})$$

where

$$G_0 = \frac{1}{E - H_N - K_\pi + i\eta} \quad \eta \rightarrow 0^+ . \quad (\text{IV-2b})$$

G_0 is the free Green's operator of the Hamiltonian H_0 and E is the collision energy in the πA center-of-mass system,

$$E = (k_0^2 + m_\pi^2)^{1/2} + (k_0^2 + M^2)^{1/2} + E_0^{\text{nucl}} . \quad (\text{IV-3})$$

\vec{k}_0 is the pion-nucleus relative momentum, M is the mass of the nucleus ($M \approx Am$), m_π is the pion mass, and E_0^{nucl} is the nuclear ground state energy (taken to be zero, see Eq. (IV-21)). T as defined in Eq. (IV-2) is a many-body operator involving both nucleon coordinates and pion coordinates. Since the free πN T matrix is well parameterized from experimental data (see Chap. I), the objective of multiple-scattering theory is to express the πA T matrix in terms of the free πN T matrix. This objective is accomplished by first rewriting Eq. (IV-2) in a form which allows the exact summing of all the pion rescatterings from a given nucleon within the nucleus [Ei-80]--

$$T = \sum_{i=1}^A T_i , \quad (\text{IV-4a})$$

with T_i defined as

$$T_i \equiv v_i + v_i G_0 T . \quad (\text{IV-4b})$$

Using Eq. (IV-4a) in Eq. (IV-4b),

$$T_i = v_i + v_i G_0 \sum_{j=1}^A T_j . \quad (\text{IV-5})$$

Subtract from both sides of Eq. (IV-5) the quantity $v_i G_0 T_i$, thus obtaining

$$(1 - v_1 G_0) T_1 = v_1 + v_1 G_0 \sum_{j \neq 1} T_j . \quad (\text{IV-6})$$

Dividing both sides of Eq. (IV-6) by $(1 - v_1 G_0)$ and defining

$$\tau_1 \equiv (1 - v_1 G_0)^{-1} v_1 , \quad (\text{IV-7})$$

Eq. (IV-6) becomes

$$T_1 = \tau_1 + \tau_1 G_0 \sum_{j \neq 1} T_j . \quad (\text{IV-8})$$

Substituting this result into Eq. (IV-4a), the Lippman-Schwinger equation for the πA transition operator is

$$T = \sum_{i=1}^A \tau_i + \sum_{i=1}^A \tau_i G_0 \sum_{j \neq i} T_j . \quad (\text{IV-9})$$

Iterating Eq. (IV-9) yields the Watson series for the πA (more generally, projectile-nucleus) transition operator--

$$T = \sum_{i=1}^A \tau_i + \sum_{i=1}^A \tau_i G_0 \sum_{j \neq i} \tau_j + \sum_{i=1}^A \tau_i G_0 \sum_{j \neq i} \tau_j G_0 \sum_{k \neq j} \tau_k + \dots . \quad (\text{IV-10})$$

Eq. (IV-10) is a general result for any form of the Green's operator G_0 , and can be applied to inelastic as well as to elastic scattering processes. The physics of Eq. (IV-10) is clear after interpretation of the τ 's. Multiplying by $(1 - v_1 G_0)$ and adding $v_1 G_0 \tau_1$ to both sides of Eq. (IV-7) gives

$$\tau_1 = v_1 + v_1 G_0 \tau_1 . \quad (\text{IV-11})$$

Eq. (IV-11) is the Lippmann-Schwinger equation for the scattering of a pion from a nucleon which is in interaction with the other $A-1$ nucleons of the nucleus. τ is a complicated many-body operator involving the nuclear Hamiltonian H_N . Returning to Eq. (IV-10), one sees that πA scattering is expressed as an infinite series of πN scattering terms (in the presence of other nucleons) for single, double, triple, etc. scatterings, with successive scatterings on the same nucleon excluded to avoid double counting.

To solve Eq. (IV-10) for the πA T matrix, one must be able to obtain an expression for the τ 's. This is a very difficult problem since the τ 's involve the nuclear Hamiltonian H_N . One can relate the τ_1 to the free πN transition operator, t_1 ,

$$t_1 = v_1 + v_1 g_0 t_1, \quad (\text{IV-12a})$$

where

$$g_0 = \frac{1}{\omega - K_\pi - K_N + i\eta} \quad \eta \rightarrow 0^+. \quad (\text{IV-12b})$$

K_N is the kinetic energy operator for the nucleon and ω is a suitable choice for the πN collision energy in the πA center-of-mass system. The relation between τ_1 and t_1 is

$$\tau_1 = t_1 + t_1 (G_0 - g_0) \tau_1. \quad (\text{IV-13})$$

With this expression for τ in Eq. (IV-10), the πA transition operator is

expressed in terms of the free πN transition operators plus nuclear medium corrections. If the difference between G_0 and g_0 is small, one can approximate $\tau_1 \approx t_1$ (impulse approximation) and the Watson series for the πA T matrix is greatly simplified, since the πA T matrix then involves the experimentally well-determined πN phase shifts. The impulse approximation is based on the assumption that the energy of the pion is sufficiently high compared to the binding energy of a single nucleon, and thus one may ignore the nuclear medium. However, the impulse approximation does not include ignoring the momentum of the bound nucleon. With $\tau_1 \approx t_1$, Eq. (IV-9) becomes

$$T = \sum_{i=1}^A t_i + \sum_{i=1}^A t_i G_0 \sum_{j \neq i} T_j . \quad (\text{IV-14})$$

Eq. (IV-14) is the starting point for deriving the lowest-order optical potential for πA elastic scattering and also the transition amplitude for πA inelastic scattering.

B. Elastic scattering

Eq. (IV-14) restricts the summation of scattering terms such that there are no successive scatterings on the same nucleon. If this restriction is dropped (large nucleus approximation), then one extra term is included, introducing an error of order $1/A$, which for large nuclei is small [St-74]. With this approximation, Eq. (IV-14) is replaced by

$$T = \sum_{i=1}^A t_i + \sum_{i=1}^A t_i G_0 \sum_j T_j . \quad (\text{IV-15})$$

Rewriting,

$$T = T + TG_0 T, \quad (\text{IV-16a})$$

where

$$T = \sum_{i=1}^A t_i. \quad (\text{IV-16b})$$

For elastic scattering, in which the nucleus remains in its ground state, one must take nuclear ground state matrix elements of the πA transition operator. For this purpose, introduce

$$|0\rangle = |\phi_0(\vec{r}_1, \vec{r}_2, \dots, \vec{r}_A)\rangle, \quad |\alpha\rangle = |\phi_\alpha(\vec{r}_1, \vec{r}_2, \dots, \vec{r}_A)\rangle \quad (\text{IV-17})$$

for the nuclear ground state and excited state wave functions, respectively. The nuclear ground state matrix element of T is

$$\begin{aligned} \langle 0|T|0\rangle &= \langle 0|T|0\rangle + \langle 0|TG_0T|0\rangle \\ &= \langle 0|T|0\rangle + \sum_{\epsilon\epsilon'} \langle 0|T|\epsilon'\rangle \langle \epsilon'|G_0|\epsilon\rangle \langle \epsilon|T|0\rangle. \end{aligned} \quad (\text{IV-18})$$

Noticing that

$$\langle \epsilon'|G_0|\epsilon\rangle = \frac{1}{E - E_\epsilon^{\text{nuc}} - K_\pi + i\eta} \langle \epsilon'|\epsilon\rangle = G_0(\epsilon)\delta_{\epsilon'\epsilon}, \quad (\text{IV-19})$$

Eq. (IV-18) can be written

$$\langle 0|T|0\rangle = \langle 0|T|0\rangle + \sum_{\epsilon} \langle 0|T|\epsilon\rangle G_0(\epsilon) \langle \epsilon|T|0\rangle . \quad (\text{IV-20})$$

In the second term of Eq. (IV-20), there are both diagonal, $\epsilon=0$, and nondiagonal, $\epsilon \neq 0$, matrix elements. The diagonal matrix elements should be larger than the nondiagonal matrix elements due to the expected good overlap of the nuclear ground state wave function with itself (especially for small momentum transfers) [Ei-80]. The diagonal terms are usually called the coherent terms since they correspond to the elastic case where the pion wavelets from different nucleon scattering centers add coherently. Exhibiting the coherent terms explicitly, Eq. (IV-20) is

$$\begin{aligned} \langle 0|T|0\rangle = & \langle 0|T|0\rangle + \langle 0|T|0\rangle \frac{1}{E - K_{\pi} + i\eta} \langle 0|T|0\rangle + \\ & \left[\sum_{\epsilon \neq 0} \langle 0|T|\epsilon\rangle G_0(\epsilon) \langle \epsilon|T|0\rangle \right] , \end{aligned} \quad (\text{IV-21})$$

where the term in brackets is small and the arbitrary zero of energy has been determined by letting the nuclear ground state energy vanish, $E_0^{\text{nuc}} = 0$. Taking only the coherent terms (the coherent approximation),

$$\langle 0|T|0\rangle = \langle 0|T|0\rangle + \langle 0|T|0\rangle \frac{1}{E - K_{\pi} + i\eta} \langle 0|T|0\rangle . \quad (\text{IV-22})$$

This equation can be rewritten as

$$\langle 0|T|0\rangle = V_{op} + V_{op} \frac{1}{E - K_{\pi} + i\eta} \langle 0|T|0\rangle , \quad (\text{IV-23a})$$

where

$$V_{op} = \langle 0 | T | 0 \rangle = \langle 0 | \sum_{i=1}^A t_i | 0 \rangle . \quad (IV-23b)$$

Eq. (IV-23) is the desired Lippmann-Schwinger equation for πA elastic scattering (compare to Eq. (IV-2)) with the nucleus represented by the lowest-order optical potential, V_{op} , which is a function of the pion coordinate \vec{r} , and energy only. V_{op} is complex, with the imaginary part representing all inelastic processes allowed by conservation of energy and by the selection rules for strong interactions.

Using the momentum representation of the one-particle Klein-Gordon equation, one must calculate the matrix elements of V_{op} in the momentum space of the pion. Denoting initial and final pion momenta in the πA center-of-mass system as \vec{k} and \vec{k}' ($|\vec{k}|$, $|\vec{k}'|$, $|\vec{k}_0|$ are not necessarily equal) and letting $|\vec{k}\rangle$ represent the pion state including its isospin,

$$\langle \vec{k}' | V_{op} | \vec{k} \rangle = \sum_{i=1}^A \langle \vec{k}' | t_i(\omega) | \vec{k} \rangle . \quad (IV-24)$$

Inserting

$$1 = \int \frac{d^3 p_1}{(2\pi)^3} \cdots \int \frac{d^3 p_A}{(2\pi)^3} |\vec{p}_1\rangle \langle \vec{p}_1| \cdots |\vec{p}_A\rangle \langle \vec{p}_A| =$$

$$\int \frac{d^3 p_1}{(2\pi)^3} \cdots \int \frac{d^3 p_A}{(2\pi)^3} |\vec{p}_1\rangle \langle \vec{p}_1| \cdots |\vec{p}_A\rangle \langle \vec{p}_A| , \quad (IV-25)$$

where $\vec{p}_1, \dots, \vec{p}_A$, $\vec{p}_1, \dots, \vec{p}_A$ are the momenta of the individual nucleons, Eq. (IV-24) can be written as

$$\begin{aligned} \langle \vec{k}^- | v_{op} | \vec{k} \rangle &= \frac{A}{\sum_{i=1}} \int \frac{d^3 p_1}{(2\pi)^3} \frac{d^3 p_2}{(2\pi)^3} \dots \frac{d^3 p_i}{(2\pi)^3} \frac{d^3 p_{i+1}}{(2\pi)^3} \dots \frac{d^3 p_A}{(2\pi)^3} \times \\ &\quad \Phi_0^*(\vec{p}_1 \vec{p}_2 \dots \vec{p}_i \dots \vec{p}_A) \times \\ &\quad \langle \vec{k}^- \vec{p}_i | t_i(\omega) | \vec{k} \vec{p}_i \rangle \Phi_0(\vec{p}_1 \vec{p}_2 \dots \vec{p}_i \dots \vec{p}_A) . \end{aligned} \quad (IV-26)$$

$\langle \vec{k}^- \vec{p}_i | t_i(\omega) | \vec{k} \vec{p}_i \rangle$ contains a momentum conserving delta function. Thus, define a reduced $\pi N T$ matrix as [Er-80]

$$\langle \vec{k}^- \vec{p}_i | t_i(\omega) | \vec{k} \vec{p}_i \rangle = \langle \vec{k}^- \vec{p}_i | | t_i(\omega) | | \vec{k} \vec{p}_i \rangle (2\pi)^3 \delta(\vec{p}_i - \vec{p}_i + \vec{q}) , \quad (IV-27)$$

where $\vec{q} = \vec{k}^- - \vec{k}$ is the three-momentum transferred to the pion. Substituting Eq. (IV-27) into Eq. (IV-26), the pion momentum space representation of the optical potential is

$$\langle \vec{k}^- | v_{op} | \vec{k} \rangle = \int \frac{d^3 p}{(2\pi)^3} \langle \vec{k}^- \vec{p} - \vec{q} | | t(\omega) | | \vec{k} \vec{p} \rangle \rho(\vec{p} - \vec{q}, \vec{p}) , \quad (IV-28a)$$

where $\rho(\vec{p} - \vec{q}, \vec{p})$ is the single-nucleon density and is given by

$$\begin{aligned} \rho(\vec{p} - \vec{q}, \vec{p}) &= \frac{A}{\sum_{i=1}} \int \frac{d^3 p_1}{(2\pi)^3} \frac{d^3 p_2}{(2\pi)^3} \dots \frac{d^3 p_{i-1}}{(2\pi)^3} \frac{d^3 p_{i+1}}{(2\pi)^3} \dots \frac{d^3 p_A}{(2\pi)^3} \times \\ &\quad \delta(\vec{p} + \sum_j^{A-1} \vec{p}_j + \vec{k}_0) \Phi_0^*(\vec{p}_1 \vec{p}_2 \dots \vec{p}_{i-1} \vec{p} - \vec{q} \vec{p}_{i+1} \dots \vec{p}_A) \times \\ &\quad \Phi_0(\vec{p}_1 \vec{p}_2 \dots \vec{p}_{i-1} \vec{p} \vec{p}_{i+1} \dots \vec{p}_A) . \end{aligned} \quad (IV-28b)$$

The single-nucleon density contains a momentum conserving delta function which ensures that the nucleus has a total momentum of $-\vec{k}_0$ in the πA center-of-mass system (see Eq. (IV-3)). $\langle \vec{k} - \vec{p} - \vec{q} | | t(\omega) | | \vec{k} \vec{p} \rangle$ possesses both spin and isospin degrees of freedom and may be written in terms of spin and isospin operators [La-73, E1-80]--

$$\begin{aligned}
 \langle \vec{k} - \vec{p} - \vec{q} | | t(\omega) | | \vec{k} \vec{p} \rangle &= \langle \vec{k} - \vec{p} - \vec{q} | | t^{ss}(\omega) | | \vec{k} \vec{p} \rangle + \\
 &\quad \langle \vec{k} - \vec{p} - \vec{q} | | t^{vs}(\omega) | | \vec{k} \vec{p} \rangle \vec{\sigma} \cdot \vec{n} + \\
 &\quad \langle \vec{k} - \vec{p} - \vec{q} | | t^{sv}(\omega) | | \vec{k} \vec{p} \rangle \vec{I} \cdot \vec{\tau} + \\
 &\quad \langle \vec{k} - \vec{p} - \vec{q} | | t^{vv}(\omega) | | \vec{k} \vec{p} \rangle \vec{\sigma} \cdot \vec{n} \vec{I} \cdot \vec{\tau} = \\
 &\quad \sum_{\xi} \langle \vec{k} - \vec{p} - \vec{q} | | t^{\xi}(\omega) | | \vec{k} \vec{p} \rangle O_{\xi} , \tag{IV-29}
 \end{aligned}$$

where $\vec{\sigma}$, \vec{n} , \vec{I} , and $\vec{\tau}$ are defined in Chap. I. Eq. (IV-28) may then be rewritten as

$$\langle \vec{k} - | v_{op} | \vec{k} \rangle = A \sum_{\xi} \int \frac{d^3 p}{(2\pi)^3} \langle \vec{k} - \vec{p} - \vec{q} | | t^{\xi}(\omega) | | \vec{k} \vec{p} \rangle \rho_{\xi}(\vec{p} - \vec{q}, \vec{p}) , \tag{IV-30a}$$

with

$$\begin{aligned}
 \rho_{\xi}(\vec{p} - \vec{q}, \vec{p}) &= \int \frac{d^3 p_2}{(2\pi)^3} \cdots \frac{d^3 p_A}{(2\pi)^3} \delta(\vec{p} + \sum_{j=2}^A \vec{p}_j + \vec{k}_0) O_{\xi} \times \\
 &\quad \Phi_0^*(\vec{p} - \vec{q} \vec{p}_2 \cdots \vec{p}_A) \Phi_0(\vec{p} \vec{p}_2 \cdots \vec{p}_A) . \tag{IV-30b}
 \end{aligned}$$

The ρ_{ξ} 's are the nuclear ground state spin/isospin scalar and vector densities. Compared to $\langle \vec{k} - \vec{p} - \vec{q} | | t^{\xi}(\omega) | | \vec{k} \vec{p} \rangle$, $\rho_{\xi}(\vec{p} - \vec{q}, \vec{p})$ is a sharply peaked

function of the nucleon momentum \vec{p} . This is a result of the nuclear size being much larger than the range of the πN interaction. Thus, one may use the factorization approximation and remove $\langle \vec{k} - \vec{p} - \vec{q} | | t^E(\omega) | | \vec{k} \vec{p} \rangle$ from the integral in Eq. (IV-30a), after evaluating at some average nucleon momentum \vec{p}_0 . Eq. (IV-30) becomes

$$\langle \vec{k} - | v_{op} | \vec{k} \rangle = A \sum_{\vec{p}} \langle \vec{k} - \vec{p}_0 - \vec{q} | | t^E(\omega_0) | | \vec{k} \vec{p}_0 \rangle \rho_{\vec{p}}(\vec{q}) , \quad (\text{IV-31a})$$

where

$$\rho_{\vec{p}}(\vec{q}) = \int \frac{d^3 p}{(2\pi)^3} \rho_{\vec{p}}(\vec{p} - \vec{q}, \vec{p}) . \quad (\text{IV-31b})$$

The value of \vec{p}_0 and ω_0 should be chosen so as to make the impulse approximation valid (see Eq. (IV-13)) and so as to optimally factorize the pion momentum space representation of the lowest-order optical potential. The final expression obtained for the optical potential is simply a product of the πN T matrix and the nuclear form factor.

The πN T matrix involved in Eq. (IV-31a) is not the free πN T matrix in the πN center-of-mass system. Denoting $\langle \vec{k} - | t(\bar{\omega}_0) | \vec{k} \rangle$ as the free πN T matrix in the πN center-of-mass system, $\langle \vec{k} - | t(\bar{\omega}_0) | \vec{k} \rangle$ is defined only for the on-energy-shell values $|\vec{k} -| = |\vec{k}|$ and $\bar{\omega}_0 = \bar{\omega}_0(k)$, where \vec{k} is the pion-nucleon relative momentum. However, $\langle \vec{k} - \vec{p}_0 - \vec{q} | | t(\omega_0) | | \vec{k} \vec{p}_0 \rangle$ involves both on-energy-shell ($|\vec{k} -| = |\vec{k}| = |\vec{k}_0|$, $(\omega_0(k_0))$) and off-energy-shell ($|\vec{k} -| \neq |\vec{k}| \neq |\vec{k}_0|$) matrix elements. Furthermore, this T matrix describes πN scattering in the πA center-of-mass system. One needs to relate $\langle \vec{k} - \vec{p}_0 - \vec{q} | | t(\omega_0) | | \vec{k} \vec{p}_0 \rangle$ to $\langle \vec{k} - | t(\bar{\omega}_0) | \vec{k} \rangle$, since $\langle \vec{k} - | t(\bar{\omega}_0) | \vec{k} \rangle$

is the T matrix given by the experimentally determined πN scattering phase shifts. The transformation is ambiguous and one method is explained in detail in [Co-84]. Briefly, one employs a frozen-target approximation ($\vec{p}_0 = -\vec{k}_0/A$) and assumes effective on-energy-shell kinematics. $\langle \vec{k} - \vec{p}_0 - \vec{q} | | t(\omega_0) | | \vec{k} \vec{p}_0 \rangle$ is approximated as

$$\begin{aligned} \langle \vec{k} - \vec{p}_0 - \vec{q} | | t(\omega_0) | | \vec{k} \vec{p}_0 \rangle &= \langle \underline{\vec{k}}' | | t(\underline{\omega}_0) | | \underline{\vec{k}} \rangle \\ &= \gamma \langle \vec{k}' | t(\bar{\omega}_0) | \vec{k} \rangle, \end{aligned} \quad (\text{IV-32a})$$

where $\underline{\vec{k}}$ is an effective on-energy-shell momentum [Co-84] associated with the πN collision energy in the πA center-of-mass system and

$$\gamma = \left[\frac{E_\pi(\kappa) E_\pi(\kappa') E_N(\kappa) E_N(\kappa')}{E_\pi(\underline{\kappa}) E_\pi(\underline{\kappa}') E_N(\underline{\kappa}/A) E_N(\underline{\kappa}'/A)} \right]^{1/2}. \quad (\text{IV-32b})$$

$E_\pi(\kappa) = (\kappa^2 + m_\pi^2)^{1/2}$, $E_N(\kappa) = (\kappa^2 + m^2)^{1/2}$, etc. $\underline{\omega}_0$ is given by

$$\underline{\omega}_0 = E_\pi(\underline{\kappa}) + E_N(\underline{\kappa}/A). \quad (\text{IV-33})$$

Since one is assuming effective on-energy-shell kinematics, all kinematic variables (\vec{k} , \vec{k}' , $\underline{\vec{k}}$, $\underline{\vec{k}}'$, $\underline{\omega}_0$, and $\bar{\omega}_0$) are related through use of the invariance of the four-vector product $s = (p_\pi^\mu + p_N^\mu)(p_{\pi\mu} + p_{N\mu})$. The effective on-energy-shell kinematics are phenomenologically determined by incorporating an energy shift parameter in $E_\pi(\underline{\kappa})$ [Co-84], i.e.,

$$E_\pi(\underline{\kappa}) = E_\pi(k) + \Delta. \quad (\text{IV-34})$$

Δ is a free parameter which adjusts the kinematics so that the approximations (impulse, factorization, frozen-target) made in deriving the lowest-order optical potential are most correct [Co-84]. The final result for the pion momentum space representation of the lowest-order optical potential is

$$\langle \vec{k}' | V_{op} | \vec{k} \rangle = A \gamma \langle \vec{k}' | \epsilon(\bar{\omega}_0) | \vec{k} \rangle \rho(\vec{q}) . \quad (\text{IV-35})$$

The connection between the optical potential and the πN phase shifts is made in the usual way for on-energy-shell kinematics [Ei-80]--

$$\langle \vec{k}' | \epsilon(\bar{\omega}_0) | \vec{k} \rangle = \frac{-2\pi}{\mu} F(\vec{k}' + \vec{k}) , \quad (\text{IV-36})$$

where μ is the reduced energy for the pion and nucleon, $\mu = [E_\pi(\kappa)^{-1} + E_N(\kappa)^{-1}]^{-1}$, and $F(\vec{k}' + \vec{k})$ is the scattering amplitude matrix discussed in Chap. I. With Eq. (I-7) and neglecting the spin-dependent term, the optical potential is

$$\langle \vec{k}' | V_{op} | \vec{k} \rangle = \frac{-2\pi}{\mu} A \gamma [a(\bar{\omega}_0) + b(\bar{\omega}_0) \vec{k}' \cdot \vec{k}] \rho(\vec{q}) , \quad (\text{IV-37})$$

which is known as the Kisslinger optical potential [Ki-55]. Transforming to the coordinate space representation,

$$V_{op}(\vec{r}) = \frac{2\pi}{\mu} A \gamma [-a(\bar{\omega}_0) \rho(\vec{r}) + b(\bar{\omega}_0) \vec{\nabla} \cdot \rho(\vec{r}) \vec{\nabla}] . \quad (\text{IV-38})$$

In Eq. (IV-38), $\rho(\vec{r})$ is the ground state nuclear density normalized to unity, $\int \rho(\vec{r}) d^3r = 1$. The ground state nuclear density may be expressed in terms of the neutron and proton densities as

$$\rho(\vec{r}) = \rho_N(\vec{r}) + \rho_Z(\vec{r}) , \quad \rho_N(\vec{r}) = \frac{N}{A}\rho(\vec{r}) , \quad \rho_Z(\vec{r}) = \frac{Z}{A}\rho(\vec{r}) , \quad (\text{IV-39})$$

where N is the number of neutrons in the nucleus and Z the number of protons. Substituting Eq. (IV-39) into Eq. (IV-38), the Kisslinger optical potential becomes

$$V_{op}(\vec{r}) = \frac{2\pi A}{\mu} \gamma \left[-a(\tilde{\omega}_0) \rho_N(\vec{r}) - a(\tilde{\omega}_0) \rho_Z(\vec{r}) + \right. \\ \left. b(\tilde{\omega}_0) \vec{\nabla} \cdot \rho_N(\vec{r}) \vec{\nabla} + b(\tilde{\omega}_0) \vec{\nabla} \cdot \rho_Z(\vec{r}) \vec{\nabla} \right] . \quad (\text{IV-40})$$

For π^+ elastic scattering from a nucleus, Eq. (IV-40) is (see Eq. (I-7))

$$V_{op}(\vec{r}) = \gamma \frac{2\pi A}{\mu \kappa^2} \left[-\frac{\kappa^2}{3} (2\alpha_{1,1}^0(\tilde{\omega}_0) + \alpha_{3,1}^0(\tilde{\omega}_0)) \rho_N(\vec{r}) - \right. \\ \left. \kappa^2 \alpha_{3,1}^0(\tilde{\omega}_0) \rho_Z(\vec{r}) + \right. \\ \left. \frac{1}{3} (2\alpha_{1,1}^1(\tilde{\omega}_0) + \alpha_{3,1}^1(\tilde{\omega}_0) + 4\alpha_{1,3}^1(\tilde{\omega}_0) + 2\alpha_{3,3}^1(\tilde{\omega}_0)) \vec{\nabla} \cdot \rho_N(\vec{r}) \vec{\nabla} + \right. \\ \left. (\alpha_{3,1}^1(\tilde{\omega}_0) + 2\alpha_{3,3}^1(\tilde{\omega}_0)) \vec{\nabla} \cdot \rho_Z(\vec{r}) \vec{\nabla} \right] . \quad (\text{IV-41})$$

A similar expression holds for π^- elastic scattering from a nucleus, which is obtained from Eq. (IV-41) by replacing $\rho_N(\vec{r})$ with $\rho_Z(\vec{r})$ and vice versa. For self-conjugate nuclei ($N = Z$) such as ${}^6\text{Li}$, the Kisslinger

AD-A147 568

PION INELASTIC SCATTERING TO THE FIRST THREE EXCITED
STATES OF LITHIUM-6(U) AIR FORCE INST OF TECH
WRIGHT-PATTERSON AFB OH R R KIZIAH DEC 84

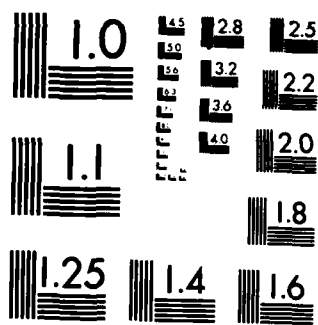
2/2

UNCLASSIFIED

AFIT/CI/NR-84-85D

F/G 20/8

NL



optical potentials for π^+ and π^- elastic scattering are identical as seen from Eqs. (IV-39) and (IV-41).

Differential cross sections for πA elastic scattering are obtained by numerically solving a Klein-Gordon equation containing the Kisslinger optical potential and the Coulomb potential, V_c . The radial piece of the Klein-Gordon equation is

$$\left(\frac{d^2}{dr^2} + \frac{l(l+1)}{r^2}\right)u_l(r) = \left(\frac{k^2}{\hbar^2} + U_c^2 - 2\xi U_{op} - 2\xi U_c\right)u_l(r), \quad (\text{IV-42})$$

where $U_c = V_c(r)/\hbar c$, $U_{op} = V_{op}(r)/\hbar c$, $\xi = E/\hbar c$, k is the incident momentum of the pion in the πA center-of-mass system, and E is the total energy of the incident pion in the πA center-of-mass system. For the elastic calculations presented in this dissertation, a modified version [Co-80] of the computer code PIRK [Ei-74] was used to solve Eq. (IV-42) for the phase shifts needed to compute the elastic differential cross sections. The modifications to the code include the transformation of the πN T matrix in the πA center-of-mass system to the πN center-of-mass system according to Eq. (IV-32) and linking PIRK to the MINUIT optimizer package [Ja-75a] in order to search on the energy shift parameter incorporated in the effective on-energy-shell kinematics, Eq. (IV-34) [Co-80]. The MINUIT optimizer package also allows searching on the shapes and magnitudes of the neutron and proton density distributions which enter into the Kisslinger optical potential. However, for the ${}^6\text{Li}$ elastic calculations, the proton density distribution was taken directly from electron scattering measurements with no variation in the shape and

magnitude, but corrected for the finite size of the proton charge. The same density distribution was used for the neutrons. Lastly, the πN partial-wave amplitudes in Eq. (IV-41) were constructed from the πN phase shifts of Rowe, Salomon, and Landau [Ro-78].

C. Inelastic scattering

The theory for πA inelastic scattering is more complicated than for πA elastic scattering. As for elastic scattering, one uses the non-relativistic multiple-scattering formalism. However, πA inelastic scattering involves a "hard" interaction which induces the nuclear transition, an interaction not present in πA elastic scattering [Ei-80]. To derive the transition amplitude for πA inelastic scattering, the main assumption is that the reaction mechanism consists of two parts: (1) many scattering steps which serve only to distort the pion wave function and in which the nucleus remains in the ground state and (2) a one-step "hard" interaction which causes the nuclear excitation [Ei-80]. Derivation of the transition amplitude involves the same approximations as the derivation of the lowest-order elastic optical potential in Sec. IV-B, although the approximations may be less well founded.

Beginning with Eq. (IV-14) and using the large nucleus approximation,

$$T = T + TG_0 T, \quad T = \sum_{i=1}^A t_i. \quad (\text{IV-43})$$

Since one is interested in inelastic scattering, matrix elements of Eq.

(IV-43) must be taken between a nuclear excited state, $|\beta\rangle$, and the nuclear ground state, $|0\rangle$ --

$$\langle\beta|T|0\rangle = \langle\beta|T|0\rangle + \langle\beta|T G_0 T|0\rangle . \quad (\text{IV-44})$$

Separating out successively higher orders of diagonal matrix elements, Eq. (IV-44) is

$$\begin{aligned} \langle\beta|T|0\rangle &= \langle\beta|T|0\rangle + \langle\beta|T|0\rangle G_0(0) \langle 0|T|0\rangle \\ &+ \langle\beta|T|\beta\rangle G_0(\beta) \langle\beta|T|0\rangle + \\ &\sum_{\epsilon \neq 0, \beta} \langle\beta|T|\epsilon\rangle G_0(\epsilon) \langle\epsilon|T|0\rangle , \end{aligned} \quad (\text{IV-45a})$$

where

$$G_0(0) = \frac{1}{E - K_\pi + i\eta} , \quad G_0(\beta) = \frac{1}{E - E_\beta^{\text{nuc}} - K_\pi + i\eta} \quad \eta \rightarrow 0^+ . \quad (\text{IV-45b})$$

Just as in the elastic scattering case, the last term of Eq. (IV-45) is ignored since it contains more nondiagonal nuclear matrix elements than the first three terms. Therefore,

$$\begin{aligned} \langle\beta|T|0\rangle &= \langle\beta|T|0\rangle + \langle\beta|T|0\rangle G_0(0) \langle 0|T|0\rangle \\ &+ \langle\beta|T|\beta\rangle G_0(\beta) \langle\beta|T|0\rangle . \end{aligned} \quad (\text{IV-46})$$

Rewriting,

$$\begin{aligned} \langle \beta | T | 0 \rangle &= [1 - \langle \beta | T | \beta \rangle G_0(\beta)]^{-1} \langle \beta | T | 0 \rangle \times \\ &[1 + G_0(0) \langle 0 | T | 0 \rangle] . \end{aligned} \quad (\text{IV-47})$$

In order to obtain a final expression for the transition amplitude, one needs to calculate the matrix elements of $\langle \beta | T | 0 \rangle$ in the momentum space of the pion. Letting $|\phi_{k_0}^+\rangle$ and $|\phi_{k_0}^-\rangle$ denote the pion initial and final plane wave states, $(E - K_\pi) |\phi_{k_0}^+\rangle = 0$,

$$\begin{aligned} \langle \phi_{k_0}^- | \beta | T | \phi_{k_0}^+ \rangle &= \langle \phi_{k_0}^- | [1 - \langle \beta | T | \beta \rangle G_0(\beta)]^{-1} \langle \beta | T | 0 \rangle \times \\ &[1 + G_0(0) \langle 0 | T | 0 \rangle] | \phi_{k_0}^+ \rangle . \end{aligned} \quad (\text{IV-48})$$

$|\phi_{k_0}^+\rangle + G_0(0) \langle 0 | T | 0 \rangle |\phi_{k_0}^+\rangle$ is the equation for the pion scattering state in which the complete optical potential, $\langle 0 | T | 0 \rangle$, is involved, i.e.,

$$|\psi_{k_0}^+\rangle = |\phi_{k_0}^+\rangle + G_0(0) \langle 0 | T | 0 \rangle |\phi_{k_0}^+\rangle , \quad (\text{IV-49a})$$

where

$$(E - K_\pi - \langle 0 | T | 0 \rangle) |\psi_{k_0}^+\rangle = 0 . \quad (\text{IV-49b})$$

Likewise, $\langle \phi_{k_0}^- | [1 - \langle \beta | T | \beta \rangle G_0(\beta)]^{-1}$ is the equation for the pion scattering state in which the lowest-order optical potential is involved, i.e.,

$$\langle \chi_{k_0}^- | = \langle \phi_{k_0}^- | + \langle \chi_{k_0}^- | \langle \beta | T | \beta \rangle G_0(\beta) , \quad (\text{IV-50a})$$

where

$$(E - K_{\pi} - \langle \beta | T | \beta \rangle) | \chi_{k_0}^+ \rangle = 0 . \quad (\text{IV-50b})$$

Using Eqs. (IV-49) and (IV-50) in Eq. (IV-48), the final result for the transition amplitude, which describes πA inelastic scattering, is

$$\langle \phi_{k_0}^+ \beta | T | \phi_{k_0}^+ 0 \rangle = \langle \chi_{k_0}^+ \beta | T | \psi_{k_0}^+ 0 \rangle . \quad (\text{IV-51})$$

This expression is referred to as the distorted-wave impulse approximation (DWIA) description of πA inelastic scattering. In practice, $\psi_{k_0}^+$ is replaced by $\chi_{k_0}^+$ and $|\beta\rangle$ in Eq. (IV-50) by $|0\rangle$, so that

$$\langle \phi_{k_0}^+ \beta | T | \phi_{k_0}^+ 0 \rangle = \langle \chi_{k_0}^+ \beta | \langle \beta | T | 0 \rangle | \chi_{k_0}^+ \rangle . \quad (\text{IV-52})$$

Thus, the DWIA expression for the transition amplitude involves the initial and final pion distorted waves, in which the distorting potential is the lowest-order elastic optical potential, $\langle 0 | T | 0 \rangle$, and an inelastic interaction, $\langle \beta | T | 0 \rangle$, which induces the nuclear transition.

Inserting

$$1 = \int \frac{d^3 k}{(2\pi)^3} |\vec{k}\rangle \langle \vec{k}| = \int \frac{d^3 k}{(2\pi)^3} |\vec{k}\rangle \langle \vec{k}| , \quad (\text{IV-53})$$

where $|\vec{k}\rangle$ represents the pion state with initial momentum \vec{k} in the πA center-of-mass system, Eq. (IV-52) becomes

$$\langle \vec{k}_0 - \beta | T | \vec{k}_0 0 \rangle \equiv T_{\beta 0} =$$

$$\int \frac{d^3 k^-}{(2\pi)^3} \frac{d^3 k}{(2\pi)^3} \chi_{\vec{k}_0}^-(\vec{k}^-) \sum_{i=1}^A \langle \vec{k}^- \beta | t_i(\omega) | \vec{k} 0 \rangle \chi_{\vec{k}_0}^+(\vec{k}) . \quad (\text{IV-54})$$

$\chi_{\vec{k}_0}^+(\vec{k}) = \langle \vec{k} | \chi_{\vec{k}_0}^+ \rangle$ and ω is an appropriate πN collision energy in the πA center-of-mass system. The spin and isospin dependences for both the nucleus and pion are not shown explicitly in Eq. (IV-54). Denoting $U_{\beta 0}(\vec{k}^-, \vec{k})$ as $\sum_{i=1}^A \langle \vec{k}^- \beta | t_i(\omega) | \vec{k} 0 \rangle$, $U_{\beta 0}(\vec{k}^-, \vec{k})$ is analogous to the pion momentum space representation of V_{op} (see Eq. (IV-24)). Therefore, after the same manipulations as performed for $\langle \vec{k}^- | V_{op} | \vec{k} \rangle$,

$$U_{\beta 0}(\vec{k}^-, \vec{k}) = A \sum_{\xi} \langle \vec{k}^- \vec{p}_0 - \vec{q} | | t^{\xi}(\omega_0) | | \vec{k} \vec{p}_0 \rangle \rho_{\xi}(\vec{q}) , \quad (\text{IV-55a})$$

where

$$\rho_{\xi}(\vec{q}) = \int \frac{d^3 p}{(2\pi)^3} \rho_{\xi}(\vec{p} - \vec{q}, \vec{p}) , \quad (\text{IV-55b})$$

$$\begin{aligned} \rho_{\xi}(\vec{p} - \vec{q}, \vec{p}) &= \int \frac{d^3 p_2}{(2\pi)^3} \cdots \frac{d^3 p_A}{(2\pi)^3} \delta(\vec{p} + \sum_{j=2}^A \vec{p}_j + \vec{k}_0) O_{\xi} \times \\ &\quad \Phi_{\beta}^*(\vec{p} - \vec{q} \vec{p}_2 \cdots \vec{p}_A) \Phi_0(\vec{p} \vec{p}_2 \cdots \vec{p}_A) . \end{aligned} \quad (\text{IV-55c})$$

The ρ_{ξ} 's are the nuclear spin/isospin scalar and vector transition densities and measure the ability of a nucleon in the state $|\vec{p}\rangle$ to be scattered into the state $|\vec{p} - \vec{q}\rangle$, while the nucleus is excited from the ground state, $|0\rangle$, to the excited state, $|\beta\rangle$, during a particular spin/isospin transition [La-73, Le-74].

As for the elastic scattering case, the πN T matrix involved in the inelastic interaction involves both on-energy-shell and off-energy-shell matrix elements and is not the free πN T matrix in the πN center-of-mass system. The transformation is explained in detail in [Co-84] and, as for the elastic case, employs a frozen-target approximation and effective on-energy-shell kinematics. Following the development of Eqs. (IV-32) through (IV-33), the effective on-energy-shell kinematics are phenomenologically determined by

$$E_{\pi}(\underline{\kappa}) = E_{\pi}(k) - E_X/2 + \Delta, \quad (\text{IV-56})$$

where E_X is the excitation energy for the nuclear state $|\beta\rangle$, and Δ is taken from elastic scattering [Co-84]. Also, the collision energies for the initial and final pion distorted waves are $E_{\pi}^X(\underline{\kappa}) = E_{\pi}(k) + \Delta$ and $E_{\pi}^X(\underline{\kappa}') = E_{\pi}(k) - E_X + \Delta$, respectively.

Following the development for the elastic scattering case but including both the spin-dependent and spin-independent terms of Eq. (I-7), the coordinate space representation of the DWIA expression for the transition amplitude is

$$T_{\beta 0} = \int d^3r \chi^{-*}(E_{\pi}^X(\underline{\kappa}'), \vec{r}) U_{\beta 0}(\vec{r}) \chi^+(E_{\pi}^X(\underline{\kappa}), \vec{r}), \quad (\text{IV-57a})$$

with

$$U_{\beta 0}(\vec{r}) = \frac{2\pi}{\mu} A \gamma [-a^{ss}(\tilde{\omega}_0) \rho_{ss}(\vec{r}) - a^{sv}(\tilde{\omega}_0) \rho_{sv}(\vec{r}) +$$

$$b^{ss}(\vec{\omega}_0)\vec{\nabla}\cdot\rho_{ss}(\vec{r})\vec{\nabla} + b^{sv}(\vec{\omega}_0)\vec{\nabla}\cdot\rho_{sv}(\vec{r})\vec{\nabla} + \\ i c^{vs}(\vec{\omega}_0)\vec{\nabla}\times\rho_{vs}(\vec{r})\vec{\nabla}\cdot\hat{n} + i c^{vv}(\vec{\omega}_0)\vec{\nabla}\times\rho_{vv}(\vec{r})\vec{\nabla}\cdot\hat{n}] . \quad (\text{IV-57b})$$

The nuclear transition densities are given by

$$\rho_{\xi}(\vec{r}) = \frac{1}{A!} \sum_{A_1=1}^A \int d^3r_1 \cdots d^3r_A \phi_{\beta}^*(\vec{r}_1 \cdots \vec{r}_A) \delta(\vec{r}-\vec{r}_1) O_{\xi 1} \phi_0(\vec{r}_1 \cdots \vec{r}_A) \\ = \frac{1}{A!} \sum_{A_1=1}^A \langle \beta | \delta(\vec{r}-\vec{r}_1) O_{\xi 1} | 0 \rangle . \quad (\text{IV-58})$$

The nuclear transition densities contain the nuclear structure input to πA inelastic calculations, and when possible, are taken from other projectile-nucleus scattering measurements such as electron scattering.

As mentioned in Chap. I, the above DWIA formalism is the most prevalent theoretical description of πA inelastic scattering, and calculations using the DWIA and well-known nuclear transition densities are adequate for describing the pion-induced excitation of nuclear states which are strongly excited. A few examples of the success of the DWIA were given in Chap. I. In many of the successful applications of the DWIA to the description of πA inelastic scattering, the nuclear structure input is fixed from electron-nucleus inelastic scattering (e, e') data. Since the essential parts of the inelastic interaction are the πN T matrix and the nuclear transition densities (see Eq. (IV-55)), uncertainties in the inelastic interaction are a result of uncertainties in the πN T matrix. In other words, within the framework of the DWIA, if the transition densities determined from fits to (e, e') data do not give

agreement between theory and data for πA inelastic scattering data, the most reasonable part of the DWIA calculation to question is the πN interaction, especially if the expressions for (e, e') and πA inelastic scattering involve the transition densities in the same manner. The examples of Chap. I, which were selective of the spin-dependent piece of the πN interaction, suggest the correctness of the parameterization of the spin-dependent piece of the πN interaction [Ca-83]. Furthermore, Morris, et al. [Mo-81] and Boyer, et al. [Bo-81] obtain good agreement between angular distributions and DWIA calculations, which use transition densities determined from (e, e') data, for inelastic scattering to low-lying collective states in ^{12}C , ^{40}Ca , ^{42}Ca , ^{44}Ca , and ^{48}Ca . The good agreement suggests the correctness of the parameterization of the spin-independent piece of the πN interaction. Since the DWIA calculations for pion inelastic scattering to the 2.185- and 3.563-MeV states of ^6Li presented in Chap. V use transition densities determined from fits to (e, e') data, the following paragraphs, taken from [Pe-79, Pe-81], briefly outline the relationship between electron-nucleus and πA inelastic scattering differential cross sections.

In order to obtain clear and simple relations, the plane-wave Born approximation and plane-wave impulse approximation (PWIA) are used in deriving the differential cross sections for electron-nucleus and πA inelastic scattering, respectively. For πA inelastic scattering, the PWIA expression for the transition amplitude is given by Eq. (IV-57) with the initial and final pion distorted waves replaced by plane waves. The expressions for the differential cross sections will be given for transitions in which only one value of J , the total angular momentum

transfer, is involved. (Although the ground state of ${}^6\text{Li}$ has spin and parity $J^\pi = 1^+$, there is only one dominant J transfer for the transitions to the 3^+ , 2.185-MeV and 2^+ , 4.25-MeV states.) For natural-parity transitions ($\Delta\pi = (-1)^J$, where $\Delta\pi$ is the parity change), the differential cross sections for electron-nucleus and πA inelastic scattering are

$$\frac{d\sigma^e}{d\Omega} = |F_L(q)|^2 = \frac{2J_f+1}{2J_i+1} |\rho_p^J(q)|^2, \quad (\text{IV-59a})$$

$$\begin{aligned} \frac{d\sigma^\pi}{d\Omega} = & \left| \sum_{\alpha} \{ t_{\alpha}^C(q) \rho_{\alpha}^J(q) + \epsilon_{\pi} t_{\alpha}^{LS}(q) \rho_{J\alpha}^{LS}(q) \} \right|^2 \\ & + \frac{1}{2} f(\theta) \left| \sum_{\alpha} t_{\alpha}^{LS}(q) \rho_{JJ}^{S\alpha}(q) \right|^2. \end{aligned} \quad (\text{IV-59b})$$

In Eq. (IV-59a), $|F_L(q)|^2$ is the longitudinal form factor and the equation is valid only for transitions which are dominantly longitudinal. $\rho_p^J(q)$ is the Fourier-Bessel transform of the proton transition density. This transition density includes the finite size of the proton charge in the electron-nucleus result but not in the πA result. In Eq. (IV-59b), ϵ_{π} is a scaling factor, $f(\theta)$ is an angle factor, α is an isospin index, $t^C(q)$ and $t^{LS}(q)$ are the Fourier-Bessel transforms of the spin-independent and spin-dependent pieces of the πN interaction, and $\rho_{J\alpha}^{LS}(q)$ and $\rho_{JJ}^{S\alpha}(q)$ are Fourier-Bessel transforms of the spin-orbit and spin transition densities. If $\rho_{JJ}^{S\alpha} \approx \rho_J^{LS} \approx 0$ and $\rho_p^J = \rho_n^J$ as in $N=Z$ nuclei, the differential cross sections for electron-nucleus and πA inelastic scattering involve only a single density and are directly related. This

is the basis for fixing the transition densities needed in πA inelastic scattering calculations from (e, e') measurements.

For unnatural-parity transitions ($\Delta\pi = (-1)^{J+1}$), the differential cross sections for electron-nucleus and πA inelastic scattering are

$$\frac{d\sigma^e}{d\Omega} = |F_T(q)|^2 = \frac{2J_f+1}{2J_i+1} \left| \frac{q\hbar}{2Mc\alpha} \left\{ \frac{1}{2} g_s^\alpha \rho_J^{s\alpha}(q) - 2g_l^\alpha \rho_{JJ}^{l\alpha}(q) \right\} \right|^2, \quad (\text{IV-60a})$$

$$\frac{d\sigma^\pi}{d\Omega} = \frac{1}{2} f(\theta) \left| \sum_{\alpha} t_{\alpha}^{LS}(q) \rho_J^{s\alpha}(q) \right|^2. \quad (\text{IV-60b})$$

$|F_T(q)|^2$ is the transverse magnetic form factor and the transition densities for the electron-nucleus expression include the finite size of the proton charge. g_s and g_l are the spin and orbital g-factors, $\rho_{JJ}^l(q)$ is the Fourier-Bessel transform of the orbital current transition density, and $\rho_J^s(q)$ is the transverse linear combination of spin transition densities,

$$\rho_J^s(q) = -\left(\frac{J}{2J+1}\right)^{1/2} \rho_{JJ+1}^s(q) + \left(\frac{J+1}{2J+1}\right)^{1/2} \rho_{JJ-1}^s(q). \quad (\text{IV-61})$$

Since Eq. (IV-60a) involves both the orbital current and transverse spin transition densities, there is not a direct connection between the electron-nucleus and πA inelastic scattering differential cross sections as for the natural-parity transitions. Use of (e, e') measurements requires the separation of the orbital current and transverse spin transition densities from the transverse magnetic form factor and depends upon the ground state and excited state wave functions. However, as for

the above natural-parity case, the theoretical expression for pion-induced unnatural-parity transitions is particularly simple, involving only a single piece of the πN interaction and a single transition density.

V. COMPARISON OF THEORY AND DATA

A. Elastic scattering

As explained in Sec. IV-B, the first-order, zero-range, impulse-approximation elastic calculations were performed with a modified version [Co-80] of the coordinate-space computer program PIRK [E1-74]. The same density distribution was used for both the point proton and point neutron density distributions which enter into the Kisslinger optical potential (see Eq. (IV-41)). This density distribution was taken from elastic electron scattering measurements [Li-71] and is a three-parameter phenomenological distribution of the form

$$\rho(r) = \frac{Z}{8\pi^{3/2}} \left[\frac{1}{a^3} \exp\left(\frac{-r^2}{4a^2}\right) - \frac{c^2(6b^2-r^2)}{4b^7} \exp\left(\frac{-r^2}{4b^2}\right) \right], \quad (V-1)$$

with $a = 0.928$ fm, $b = 1.26$ fm, and $c = 0.48$ fm [Li-71]. The elastic electron scattering parameters in Eq. (V-1) were corrected for the finite size of the proton charge according to

$$\langle r^2 \rangle_{pp} = \langle r^2 \rangle_{ch} - (0.8)^2, \quad (V-2)$$

where $\langle r^2 \rangle_{pp}$ is the mean-square radius of the point proton density, $\langle r^2 \rangle_{ch}$ is the mean-square radius of the charge density as determined from electron scattering measurements ($\langle r^2 \rangle_{ch}^{1/2} = 2.56 \pm 0.05$ fm) [Li-71], and 0.8 fm is the root-mean-square radius of the charge distribution for a

single proton [El-61].

The measured differential cross sections for π^+ elastic scattering from ${}^6\text{Li}$ at $T_\pi = 120$ and 180 MeV and the differential cross sections for π^- elastic scattering from ${}^6\text{Li}$ at $T_\pi = 164$ MeV taken from Zichy's work at SIN [Zi-80], along with the elastic calculations, are presented in Fig. V-1. Fig. V-2 shows the elastic calculations and π^+ elastic scattering differential cross sections for $100 < T_\pi < 260$ MeV and $q \approx 109$ MeV/c. For the elastic calculations, the partial-wave amplitudes in the Kisslinger optical potential (see Eq. (IV-41)) were evaluated at an energy of 30.0 MeV below the incident pion beam energy, i.e., in Eq. (IV-34), $\Delta = -30.0$ MeV. This value of Δ was chosen from the work of Cottingham and Holtkamp [Co-80]. They found that a value of $\Delta \approx -30$ MeV gave better agreement between pion elastic scattering data and calculations for nuclei ranging from ${}^9\text{Be}$ to ${}^{208}\text{Pb}$. Elastic calculations were also performed for the π^+ 120- and 180-MeV and π^- 164-MeV data sets with a one-parameter search on the shift in the collision energy. The result of the search was $\Delta \approx -20$ MeV. However, the elastic calculations with $\Delta \approx -20$ MeV differ only slightly from those with $\Delta \approx -30$ MeV.

As seen from Figs. V-1 and V-2, there is good agreement between the elastic calculations and the measured elastic differential cross sections. Since the lowest-order elastic optical potential is the distorting potential used for the generation of the initial and final pion distorted waves for inelastic calculations (see Eq. (IV-52)), the good agreement indicates adequate handling of the distortions.

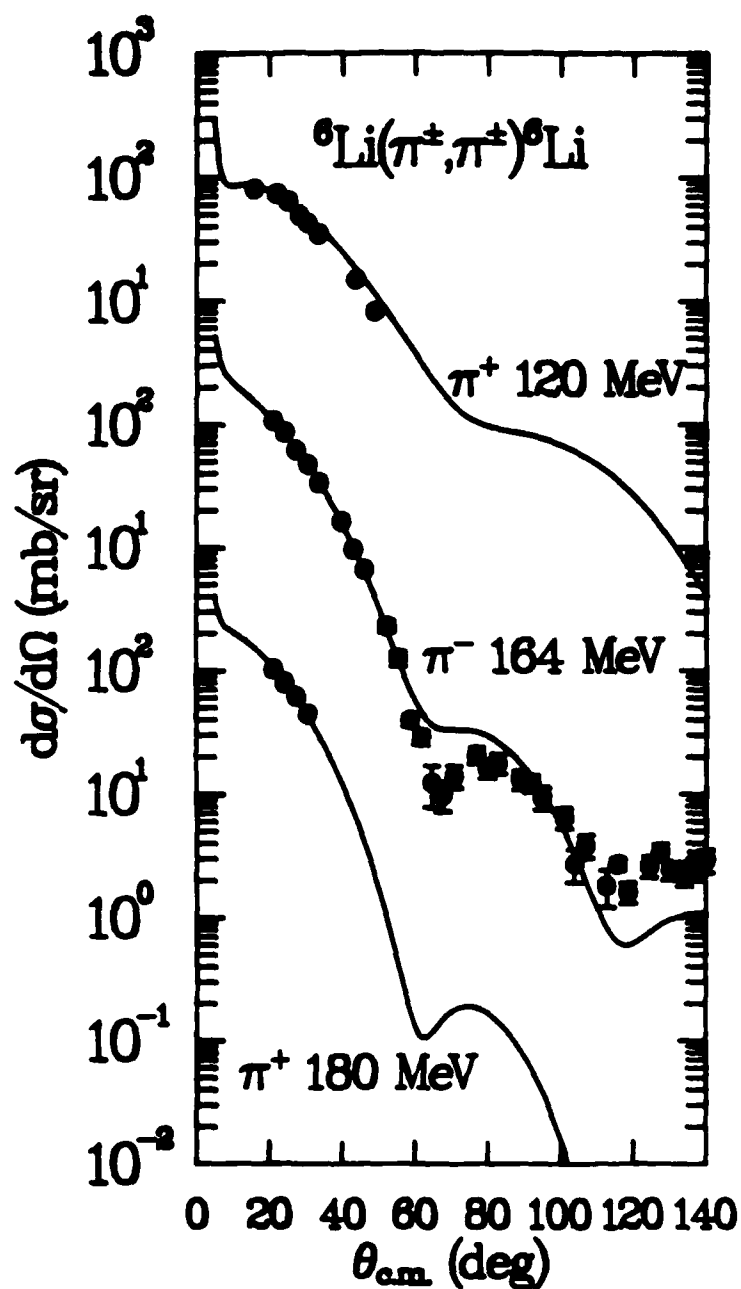


Fig. V-1: Differential cross sections for π^+ and π^- elastic scattering for ${}^6\text{Li}$ for $T_\pi = 120, 164$, and 180 MeV. The calculations include a ~ 30 MeV shift in the energy at which the optical model parameters are calculated. The 164-MeV data are from [Zi-80].

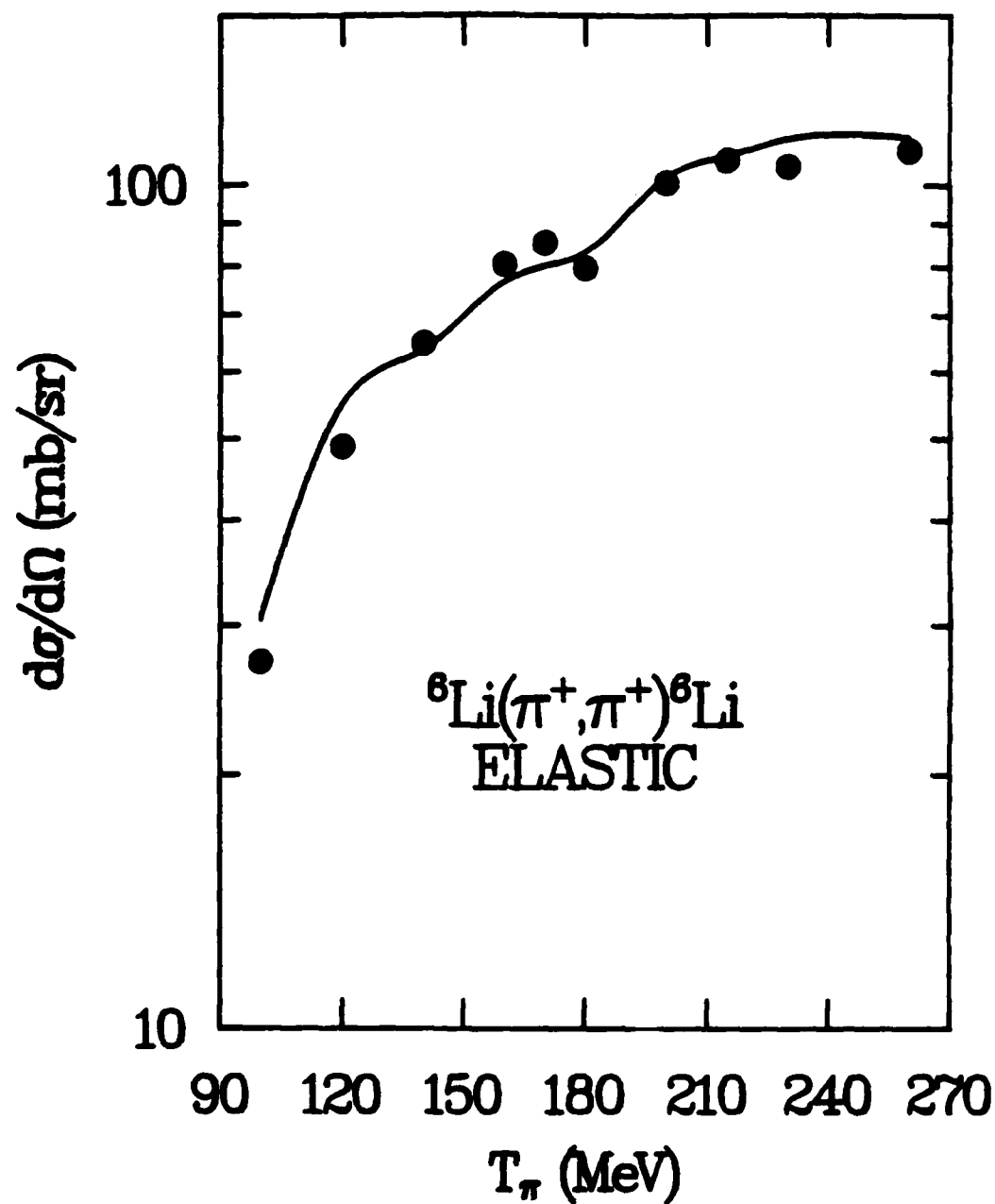


Fig. V-2: Differential cross sections for π^+ elastic scattering for ${}^6\text{Li}$ at a constant $q = 109$ MeV/c. The calculation includes a -30 MeV shift in the energy at which the optical model parameters are calculated.

B. Inelastic scattering

The inelastic calculations presented in the following sections use the DWIA expression for the transition amplitude (see Eq. (IV-57)). The initial and final pion distorted waves are calculated from the lowest-order elastic optical potential employed in the elastic calculations using the coordinate-space computer program UTDWPI [Bo-n.d.]. Calculation of the inelastic interaction, $U_{\beta 0}$, uses the frozen-target approximation and effective on-energy-shell kinematics and a collision energy obtained from the elastic calculations (see Eq. (IV-56)). For the inelastic calculations using Cohen-Kurath intermediate coupling p-shell wave functions [Co-65] and pure LS-coupling p-shell wave functions, a modification of the generalized inelastic scattering potential code ALLWRLD [Ca-84] is used to generate the nuclear transition densities from harmonic oscillator wave functions and subsequently calculate the inelastic interaction. The harmonic oscillator parameters and renormalization constants (shape and strength parameters for the transition densities) include the standard center-of-mass correction needed when using shell-model wave functions. The differential cross sections are then generated from the code UTDWPI. For all other inelastic calculations, only the code UTDWPI is used and no center-of-mass correction is included in the harmonic oscillator parameters and renormalization constants. However, these inelastic calculations use center-of-mass corrected transition densities with the correction being applied in momentum space in the usual way.

1. 3^+ , $T=0$, 2.185-MeV state

Electron-nucleus inelastic scattering measurements indicate that the natural-parity transition to the 2.185-MeV level of ${}^6\text{Li}$ is almost completely longitudinal, with measurements in the region of $q = 0.7$ to 1.8 fm^{-1} yielding a transverse form factor which is less than 2% of the longitudinal form factor [Ne-71]. Since the spin-orbit and spin transition densities are approximately zero [Ca-84a], the πA inelastic interaction, $U_{\beta 0}$, involves only the spin-independent central component of the πN interaction and the isoscalar matter transition density (see Eq. (IV-59b) and discussion). Inelastic calculations for this natural-parity transition were performed using two different transition densities derived from pure LS-coupling and Cohen-Kurath intermediate coupling p-shell wave functions. Each calculation employed equal transition densities for the protons and neutrons. The harmonic oscillator parameter, α ($\alpha = (M\omega/\hbar)^{1/2}$, where M is the nucleon mass and $\hbar\omega$ is the energy quantum of the harmonic oscillator), and renormalization constant for the transition density derived from the pure LS-coupling p-shell wave functions are 0.534 fm^{-1} and 2.03. These values were taken from [Pe-82] and were deduced in [Br-72] from a fit to the (e,e') data of [Be-63, Ne-69]. Using these values, Petrovich, *et al.* obtained good agreement between theory and experiment for the ${}^6\text{Li}(p,p'){}^6\text{Li}^*(2.185 \text{ MeV})$ differential cross sections at $E_p = 25$ and 45 MeV [Pe-82]. The transition density derived from the intermediate coupling p-shell wave functions uses $\alpha = 0.558 \text{ fm}^{-1}$ and a renormalization constant of 1.93, again determined from (e,e') data [Ca-84a].

Electron scattering longitudinal form factors [Be-76, Be-79] are shown in Fig. V-3. The solid (dashed) curves correspond to the transition densities computed from the pure LS- (intermediate) coupling p-shell wave functions. Both theoretical form factors are similar, with the intermediate coupling form factor in better agreement with the (e, e') measurements. The differential cross sections for π^+ inelastic scattering to the 2.185-MeV state and DWIA calculations for $T_\pi = 120$ and 180 MeV are presented in Fig. V-4. Fig. V-5 shows the data and calculations for $T_\pi = 100$ to 260 MeV with the differential cross sections corresponding to a constant momentum transfer $q \approx 109$ MeV/c. From the data and calculations, the first maxima of the angular distributions for the 2.185-MeV state are expected to be at $q \approx 164$ MeV/c. The intermediate coupling calculation is in good agreement with both the 120- and 180-MeV experimental angular distributions. Furthermore, this calculation reproduces well the constant- q experimental differential cross sections, considering that the theoretical values plotted in Fig. V-5 are taken from the steep forward slope of the various angular distributions where errors would produce the greatest variations. The pure LS-coupling calculation yields similar shapes for the 120- and 180-MeV angular distributions and the constant- q differential cross sections as does the intermediate coupling calculation but overestimates the magnitudes. Such disagreement suggests that the renormalization constant is too large.

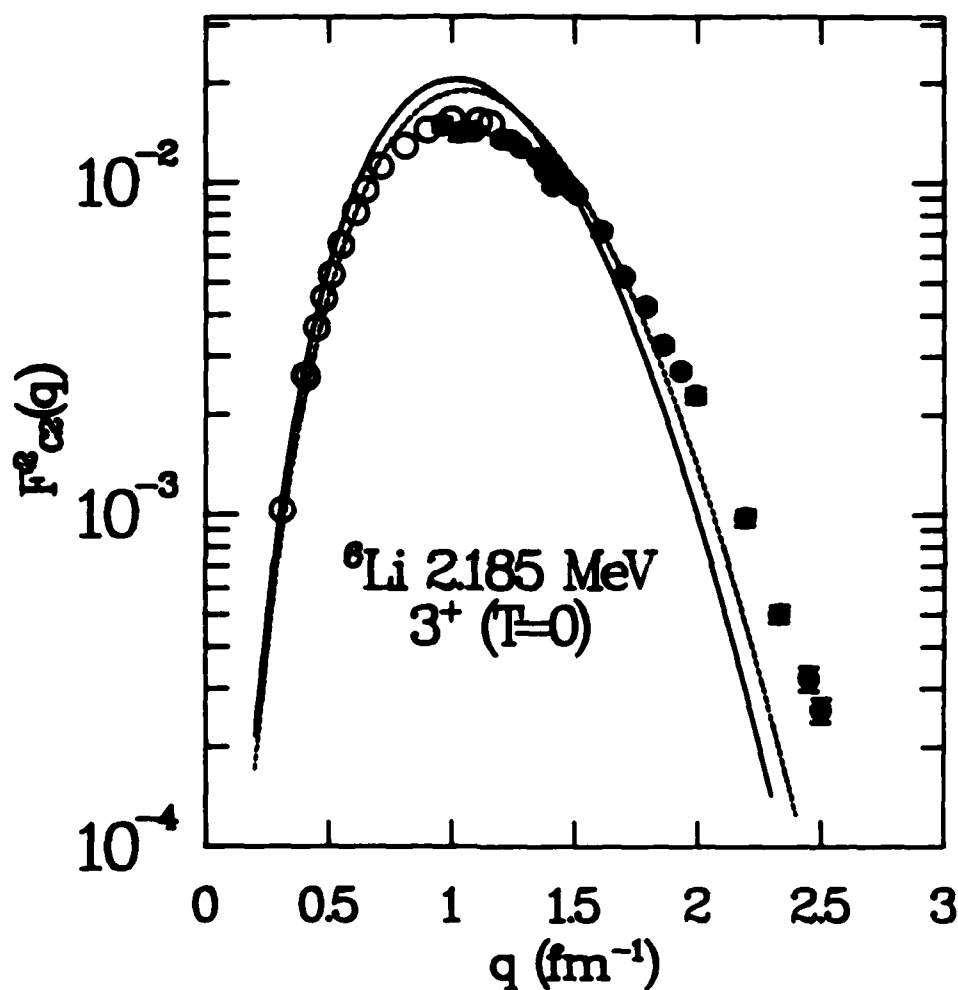


Fig. V-3: $|F_L(q)|^2$ for the 3^+ , $T=0$, 2.185-MeV state of ${}^6\text{Li}$. The calculations used isoscalar matter transition densities derived from pure LS-coupling (solid curve) and Cohen-Kurath intermediate coupling (dashed curve) p-shell wave functions with $\alpha = 0.534 \text{ fm}^{-1}$ and a renormalization constant of 2.03 and $\alpha = 0.558 \text{ fm}^{-1}$ and a renormalization constant of 1.93, respectively. The data are from [Be-76] (open circles) and [Be-79] (solid circles).

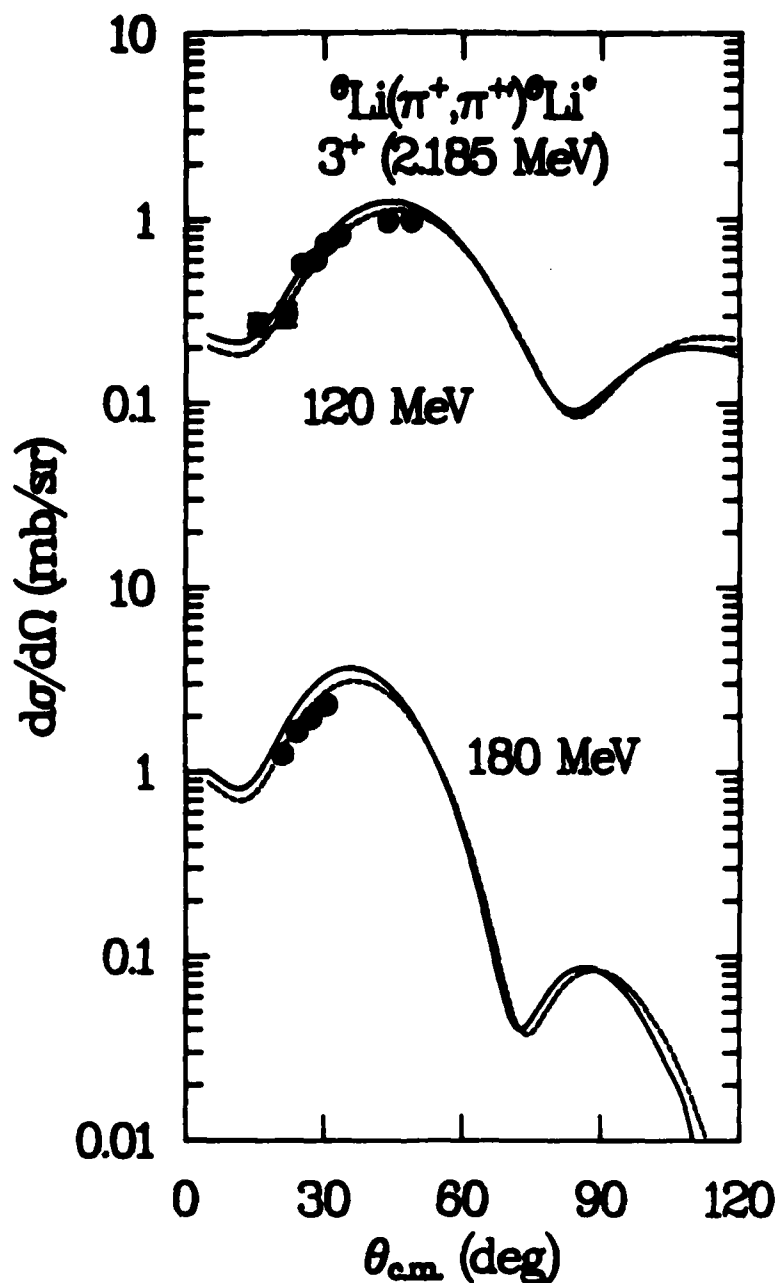


Fig. V-4: Angular distributions for π^+ inelastic scattering to the 3^+ , $T=0$, 2.185-MeV state of ${}^6\text{Li}$ for $T_\pi = 120$ and 180 MeV. The calculations used isoscalar matter transition densities derived from pure LS-coupling (solid curve) and Cohen-Kurath intermediate coupling (dashed curve) p-shell wave functions with $\alpha = 0.534 \text{ fm}^{-1}$ and a renormalization constant of 2.03 and $\alpha = 0.558 \text{ fm}^{-1}$ and a renormalization constant of 1.93, respectively.

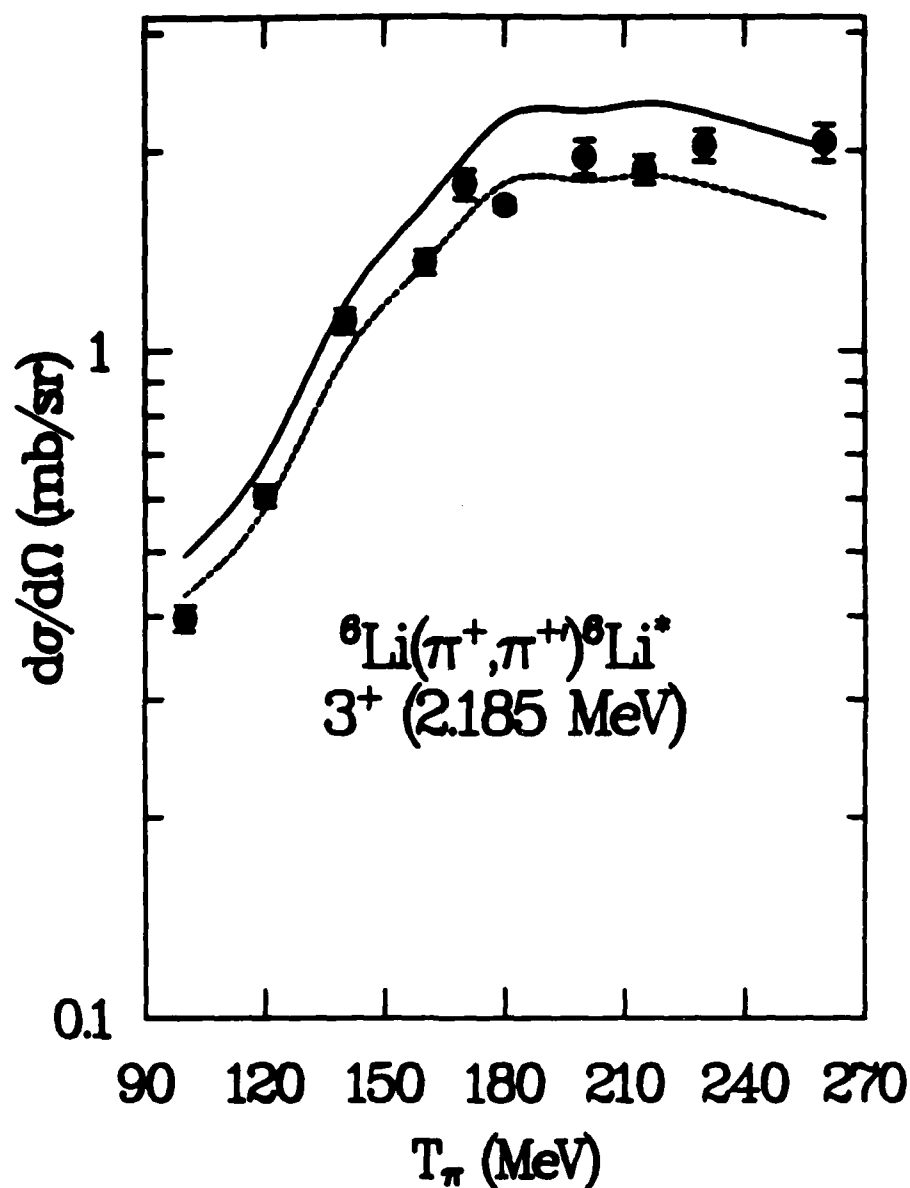


Fig. V-5: Differential cross sections for π^+ inelastic scattering to the 3^+ , $T=0$, 2.185-MeV state of ${}^6\text{Li}$ at a constant $q = 109 \text{ MeV/c}$. The calculations used isoscalar matter transition densities derived from pure LS-coupling (solid curve) and Cohen-Kurath intermediate coupling (dashed curve) p-shell wave functions with $\alpha = 0.534 \text{ fm}^{-1}$ and a renormalization constant of 2.03 and $\alpha = 0.558 \text{ fm}^{-1}$ and a renormalization constant of 1.93, respectively.

2. 2^+ , $T=0$, 4.25-MeV state

The electron scattering form factors for both natural-parity transitions to the 2.185- and 4.25-MeV levels have the same dependences on the momentum transfer [Be-63]. Therefore, the transition to the 4.25-MeV state is principally longitudinal, and this transition was treated as completely analogous to the excitation of the 2.185-MeV level. However, even though the 4.25-MeV state is observed in (e, e') spectra, a detailed form factor has not been measured because of this state's large natural width, the overlapping 5.37-MeV state, and the large continuum background [Be-82]. As a result, a transition density cannot be deduced from (e, e') data as was the case for the transition to the 2.185-MeV level. Thus, a transition density was derived from Cohen-Kurath intermediate coupling p-shell wave functions with $\alpha = 0.52 \text{ fm}^{-1}$ and a renormalization constant of 0.82 determined from fitting the (π^+, π^{+-}) data at $T_\pi = 120$ and 180 MeV. This transition density yields a radiative width, $\Gamma_0^{(E2)}$, of 3.02 eV in agreement with the experimental value of $5.4 \pm 2.8 \text{ eV}$ [Ei-69]. The 4.25-MeV experimental and theoretical 120- and 180-MeV angular distributions and the constant- q differential cross sections are shown in Figs. V-6 and V-7, respectively. The agreement is not as good as for the 2.185-MeV state but is very reasonable considering the difficulties in extracting the cross sections and possible uncertainties in the transition density.

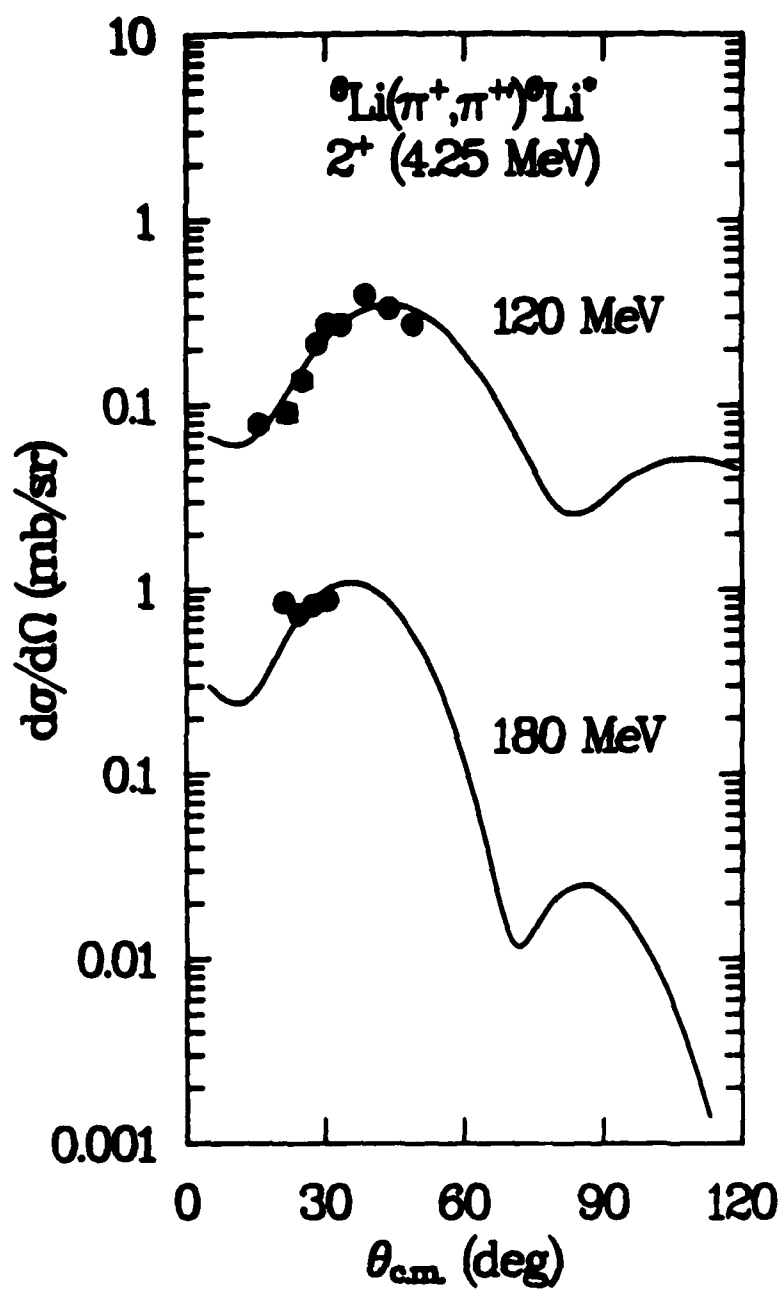


Fig. V-6: Angular distributions for π^+ inelastic scattering to the 2^+ , $T=0$, 4.25-MeV state of ${}^6\text{Li}$ for $T_\pi = 120$ and 180 MeV. The calculation used an isoscalar matter transition density derived from Cohen-Kurath intermediate coupling p-shell wave functions with $\alpha = 0.52 \text{ fm}^{-1}$ and a renormalization constant of 0.82.

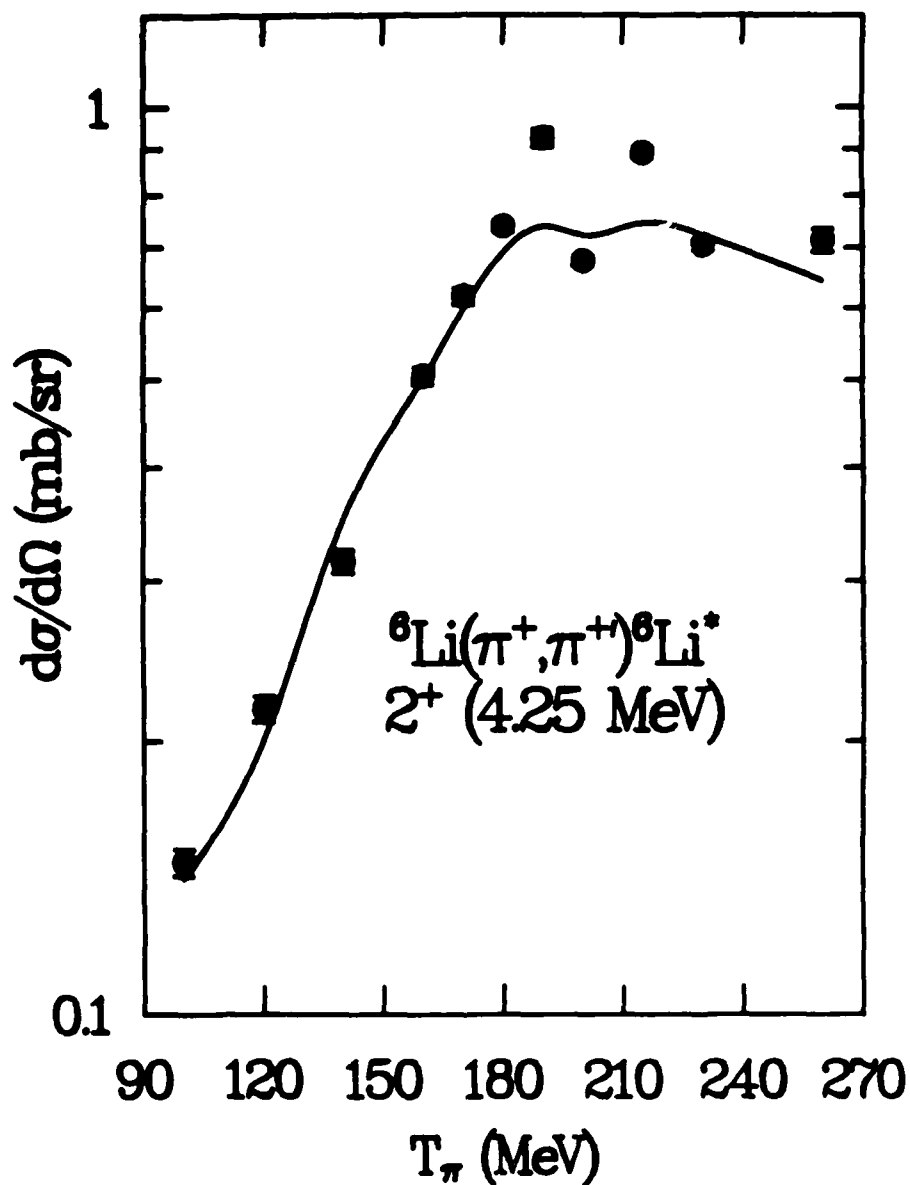


Fig. V-7: Differential cross sections for π^+ inelastic scattering to the 2^+ , $T=0$, 4.25-MeV state of ${}^6\text{Li}$ at $q \approx 109 \text{ MeV/c}$. The calculation used an isoscalar matter transition density derived from Cohen-Kurath intermediate coupling p-shell wave functions with $\alpha = 0.52 \text{ fm}^{-1}$ and a renormalization constant of 0.82.

3. 0^+ , $T=1$, 3.563-MeV state

As is the case for the natural-parity transitions to the 2.185- and 4.25-MeV levels of ${}^6\text{Li}$, the DWIA description of the pion-induced unnatural-parity transition to the 3.563-MeV state is straightforward, involving only a single component of the πN interaction and a single nuclear transition density (see Eq. (IV-60b)). The spin-dependent piece of the πN interaction is represented by the zero-range spin-orbit operator [Ca-83] which Carr, *et al.* used for their successful analysis of the stretched 4^- and 6^- states in ${}^{16}\text{O}$ and ${}^{28}\text{Si}$, and the transition density is the transverse spin transition density. For the following DWIA calculations, three different transverse spin transition densities were used, each transition density determined from fits to various (e,e') measurements but compared to the most recent sets of (e,e') data [Be-75, Be-79]. The proton and neutron transition densities were taken to be equal. The reasons for using three transition densities are: (1) The p-shell harmonic oscillator basis is known to result in a poor description of the 3.563-MeV (e,e') transverse magnetic form factor over the entire second lobe, $q > 1.4 \text{ fm}^{-1}$ [Be-75]. Therefore, one transition density which reproduces both the first and second lobes of the form factor is used. (2) Since there is no antianalog to the 3.563-MeV state as is the situation for the 12.71-/15.11-MeV antianalog-analog pair of ${}^{12}\text{C}$, any anomalies in the 3.563-MeV excitation function depend upon comparison of theory with data and not data for analogs as for the 15.11-MeV level. Thus, accurate spin transition densities are imperative.

The first analysis for the spin-flip transition to the 3.563-MeV state used a transverse spin transition density derived from Cohen-Kurath intermediate coupling p-shell wave functions. The harmonic oscillator parameter was chosen to be $\alpha = 0.518 \text{ fm}^{-1}$ from the work of Petrovich, et al. [Pe-82], who fitted the (e, e') data of [Ne-71, Be-75, Be-79] using pure LS-coupling p-shell wave functions. In the fitting procedure, the lower q data were given the most weight. The renormalization constant was determined to be 0.97 from a fit to the most recent sets of (e, e') data for the form factor. Petrovich, et al. conclude that both sets of wave functions provide an adequate description of the experimental static moments and transition probabilities of ${}^6\text{Li}$ with the exception of the quadrupole moment [Pe-82]. However, the Cohen-Kurath intermediate coupling p-shell wave functions were chosen because they give a slightly better fit to the most recent sets of (e, e') data [Be-75, Be-79] for the inelastic M1 form factor. Fig. V-8 shows the calculated transverse magnetic form factor (solid curve) and the (e, e') data for the transition to the 3.563-MeV state.

The second DWIA calculation employed a transverse spin transition density obtained from the empirical shell-model wave functions of Donnelly and Walecka [Do-73]. These wave functions are almost identical to the pure LS-coupling p-shell wave functions. Using p-shell harmonic oscillator radial wave functions for the valence nucleons, Donnelly and Walecka determined the one body density matrix elements from normalization conditions and from fits to the ground state magnetic dipole and electric quadrupole moments and the M1 form factors for electron elastic and inelastic scattering for $q < 1.01 \text{ fm}^{-1}$ [Do-73]. A harmonic

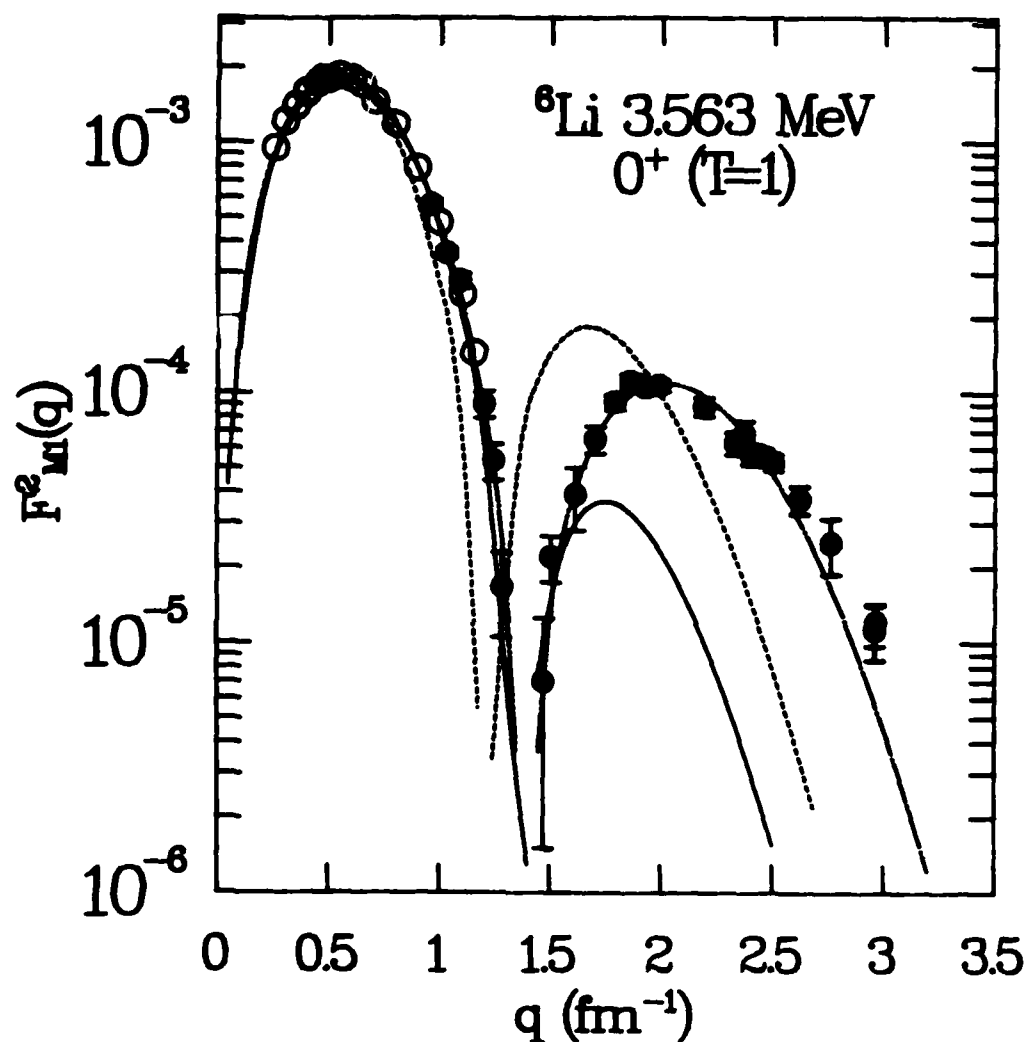


Fig. V-8: $|F_T(q)|^2$ for the 0^+ , $T=1$, 3.563-MeV state of ${}^6\text{Li}$. The calculations used transition densities derived from Cohen-Kurath intermediate coupling p-shell wave functions (solid curve) with $\alpha = 0.518 \text{ fm}^{-1}$ and a renormalization constant of 0.97, transition densities derived from the empirical shell-model wave functions of Donnelly and Walecka (dashed curve) with $\alpha = 0.493 \text{ fm}^{-1}$ and a renormalization constant of 0.96, and phenomenological transition densities based on the work of Bergstrom, *et al.* (chain-dot curve). The data are from [Be-75] (open circles) and [Be-79] (solid circles).

oscillator parameter [Do-73] $\alpha = 0.493 \text{ fm}^{-1}$ and a renormalization constant of 0.96 (determined from a fit to the most recent sets of (e, e') data) were used in this second set of calculations. The resultant inelastic M1 form factor (dashed curve) is compared to the (e, e') data in Fig. V-8.

The third analysis used a phenomenological transverse spin transition density based on the work of Bergstrom, et al. [Be-79]. This transition density was derived in the same manner as the transition density of Donnelly and Walecka except that the (e, e') data of [Be-75, Be-79], which extend to $q = 2.96 \text{ fm}^{-1}$, were fitted with a polynomial form for the p-shell radial transition density. The wave functions for the ${}^6\text{Li}$ ground state and 3.563-MeV state were taken to be described by the SASK-A amplitudes of Bergstrom, et al. [Be-79]. The radial transition density has a phenomenological form

$$R^2(r) = \exp(-r^2/b^2)(a_2 r^2 + a_4 r^4 + a_6 r^6), \quad (\text{V-3})$$

with $b = 2.02 \text{ fm}$, $a_2 = 6.625 \times 10^{-2} \text{ fm}^{-5}$, $a_4 = -5.036 \times 10^{-3} \text{ fm}^{-7}$, $a_6 = 1.967 \times 10^{-4} \text{ fm}^{-9}$, yielding a reduced χ^2 of 1.32 from a fit to the inelastic M1 form factor, which is presented in Fig. V-8 (chain-dot curve).

The π^+ inelastic scattering measurements and DWIA calculations at $T_\pi = 120$ and 180 MeV for the spin-flip transition to the 3.563-MeV state are shown in Fig. V-9. At 120 MeV the three transverse spin transition densities give equivalent shapes for the angular distribution in the range of the (π^+, π^{+-}) data, $15.7^\circ < \theta_{\text{c.m.}} < 48.9^\circ$. All calculations

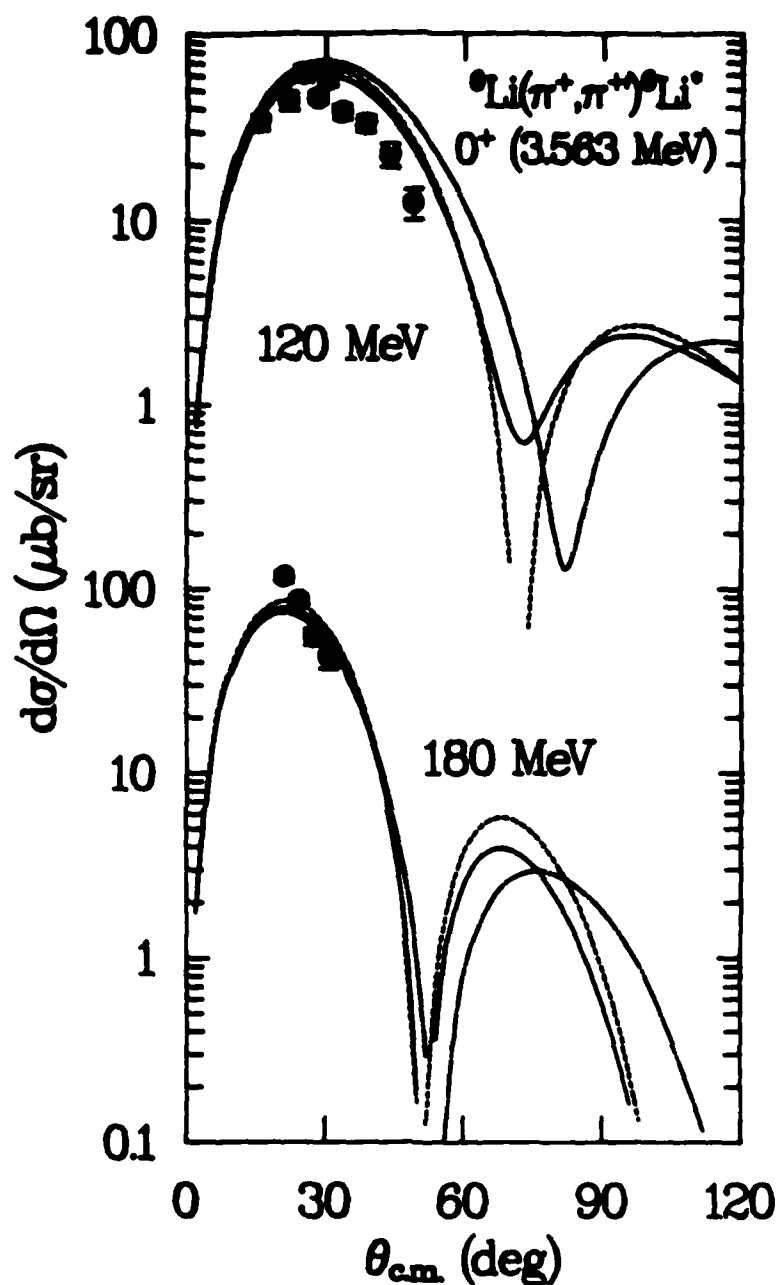


Fig. V-9: Angular distributions for π^+ inelastic scattering to the 0^+ , $T=1$, 3.563-MeV state of ${}^6\text{Li}$ for $T_\pi = 120$ and 180 MeV. The calculations used a transverse spin transition density derived from Cohen-Kurath intermediate coupling p-shell wave functions (solid curve) with $\alpha = 0.518 \text{ fm}^{-1}$ and a renormalization constant of 0.97, a transverse spin transition density derived from the empirical shell-model wave functions of Donnelly and Walecka (dashed curve) with $\alpha = 0.493 \text{ fm}^{-1}$ and a renormalization constant of 0.96, and a phenomenological transverse spin transition density based on the work of Bergstrom, *et al.* (chain-dot curve).

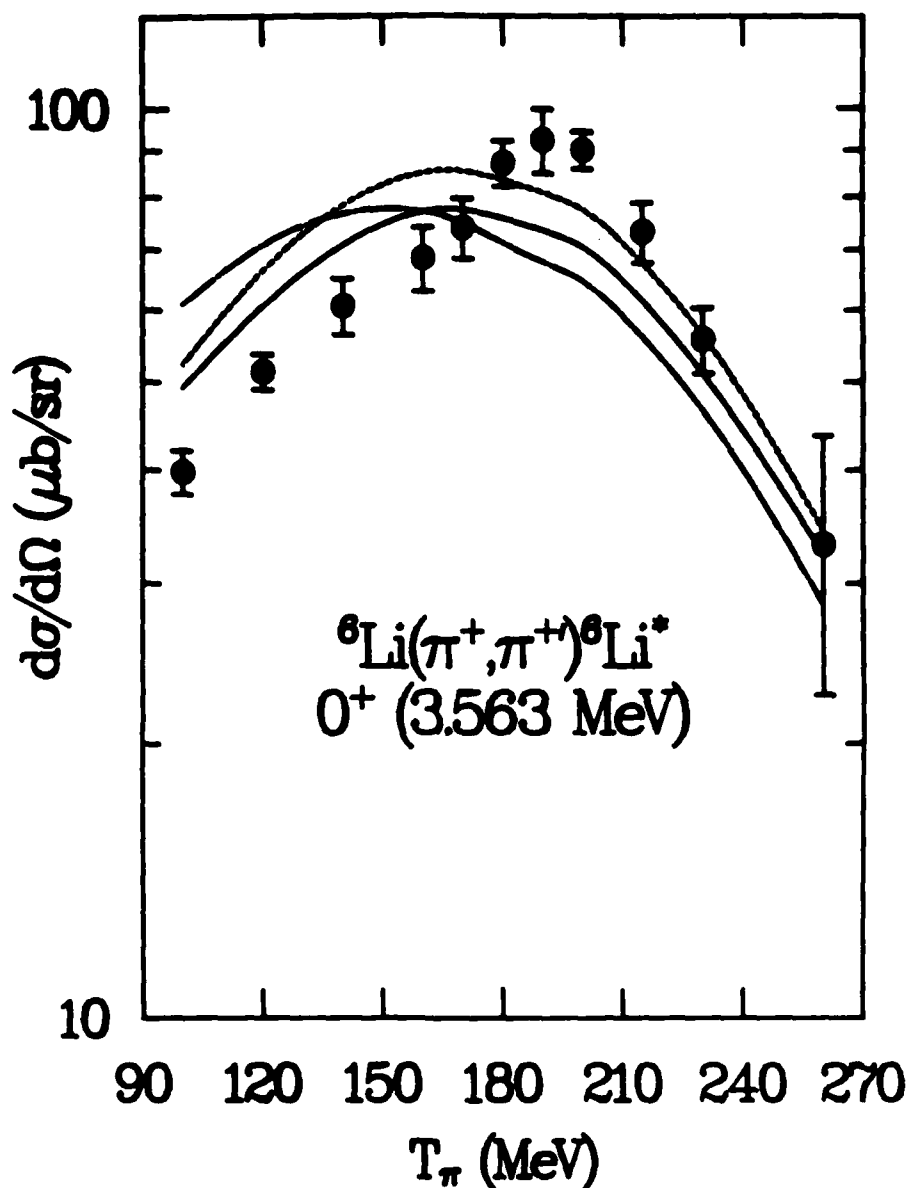


Fig. V-10: Excitation function at a constant $q \approx 109 \text{ MeV}/c$ for π^+ inelastic scattering to the 0^+ , $T=1$, 3.563-MeV state of ${}^6\text{Li}$. The calculations used a transverse spin transition density derived from Cohen-Kurath intermediate coupling p-shell wave functions (solid curve) with $\alpha = 0.518 \text{ fm}^{-1}$ and a renormalization constant of 0.97, a transverse spin transition density derived from the empirical shell-model wave functions of Donnelly and Walecka (dashed curve) with $\alpha = 0.493 \text{ fm}^{-1}$ and a renormalization constant of 0.96, and a phenomenological transverse spin transition density based on the work of Bergstrom, et al. (chain-dot curve).

predict the correct location for the first maximum of $\theta_{c.m.} = 28^\circ$. However, the Cohen-Kurath intermediate coupling (solid curve), Donnelly and Walecka (dashed curve), and phenomenological (chain-dot curve) calculations overestimate the magnitude of the first maximum by 18%, 29%, and 38%, respectively. The three transverse spin transition densities yield similar results for the shape of the 180-MeV angular distribution through the first minimum but differ through the second maximum and minimum. Each calculation underestimates the magnitude of the first maximum by at least 26%. Fig. V-10 shows the π^+ 3.563-MeV excitation function data at $q \approx 109$ MeV/c and DWIA analyses. None of the transverse spin transition densities predict the measured shape and magnitude of the excitation function. The three DWIA calculations disagree with the data by at least $\approx 20\%$ at both the low and high incident pion energies.

C. Discussion and results

The disagreement between theory and data for the 120- and 180-MeV angular distributions and excitation function for the unnatural-parity transition to the 3.563-MeV state is difficult to understand, as is the disagreement observed for the unnatural-parity transition to the 15.11-MeV state of ^{12}C . For comparison, the 12.71- and 15.11-MeV excitation functions along with DWIA calculations as described in [Mo-82] are shown in Fig. V-11. As noted in Chap. I, a simple DWIA description of πA inelastic scattering, which uses a single piece of the πN interaction and a single nuclear transition density, has been successful in describing unnatural-parity transitions in many nuclei. Using the

zero-range spin-orbit operator and a transverse spin transition density derived from Cohen-Kurath p-shell wave functions, Morris, et al. [Mo-82] adequately reproduced the measured 12.71-MeV excitation function. Furthermore, Cottingham, et al. [Co-84] adequately describe the 12.71-MeV angular distributions for $T_{\pi} = 100$ to 260 MeV. Even though there is an energy-dependent enhancement near $T_{\pi} = 180$ MeV in the 15.11-MeV excitation function, the low-energy ($T_{\pi} = 100$ and 116 MeV) angular distributions for this state are reproduced by simple DWIA calculations [Co-84]. Using the same zero-range spin-orbit operator for the representation of the spin-dependent piece of the πN interaction and three different transverse spin transition densities, DWIA calculations do not adequately reproduce either the 120-MeV and 180-MeV angular distributions or the excitation function for the transition to the 3.563-MeV state. However, the measured angular distributions and constant- q differential cross sections at energies from $T_{\pi} = 100$ to 260 MeV for the natural-parity transitions to the 2.185- and 4.25-MeV levels of ${}^6\text{Li}$ are reproduced using only the spin-independent central piece of the πN interaction and transition densities derived from Cohen-Kurath intermediate coupling p-shell wave functions.

The configuration-space, zero-range form of the spin-dependent component of the πN interaction of Carr, et al. [Ca-83] is most likely not in error. Furthermore, the transverse spin transition densities used for the transition to the 3.563-MeV level yield inelastic M1 form factors which agree with the (e, e') data for $q < 1.4 \text{ fm}^{-1}$ (see Fig. V-8), a range of q that sufficiently covers the $q = 0.55 \text{ fm}^{-1}$ at which the excitation function was measured. However, this does not eliminate uncertainties in

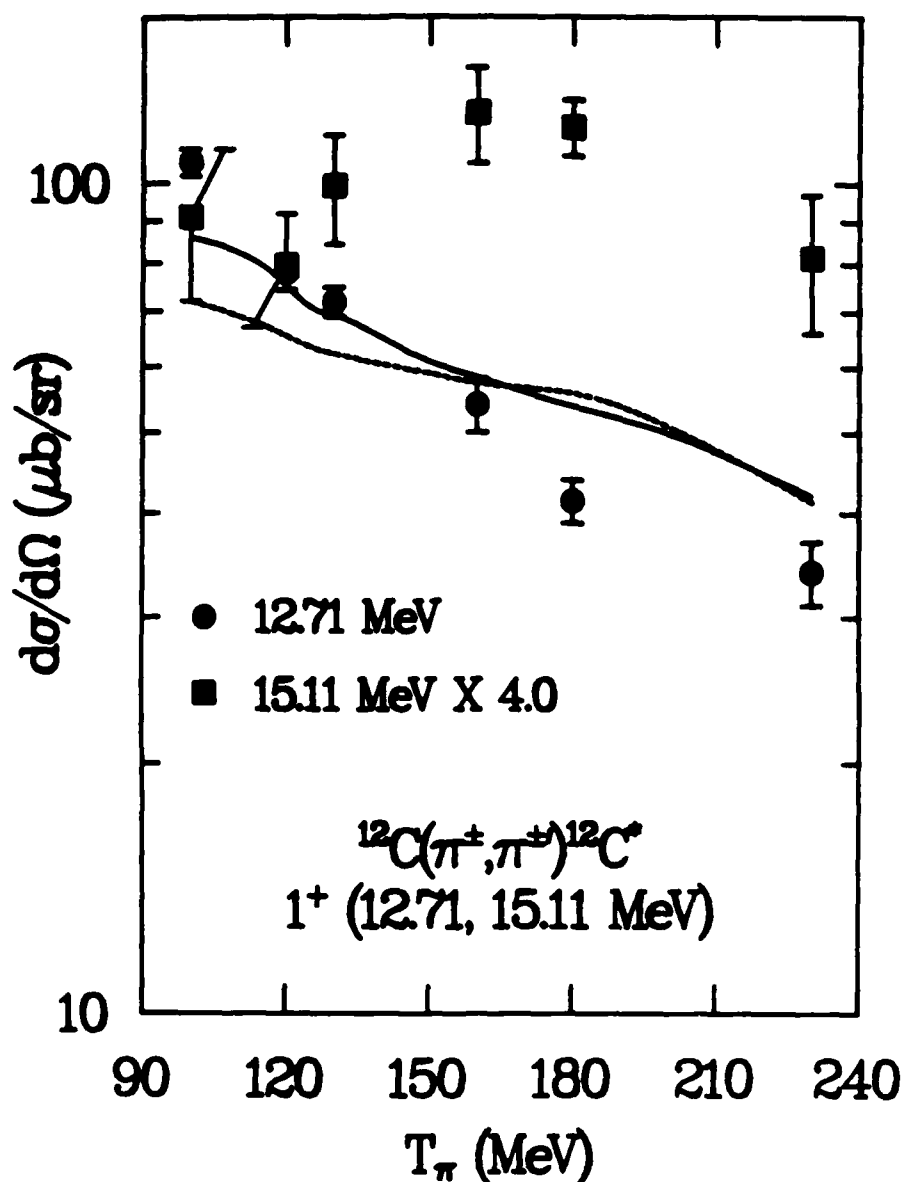


Fig. V-11: Excitation functions (averaged π^+ and π^- cross sections to remove isospin mixing) at a constant $q = 124 \text{ MeV/c}$ for pion inelastic scattering to the 1^+ , $T=0$, 12.71-MeV (solid circles) and 1^+ , $T=1$, 15.11-MeV (solid squares) states of ^{12}C . The calculations used transverse spin transition densities derived from Cohen-Kurath p-shell wave functions [Mo-82]. The solid curve is for the 12.71-MeV state. The dashed curve is for the 15.11-MeV state and has been multiplied by four.

the transverse spin transition densities since the electron scattering inelastic M1 form factor depends upon both the orbital current and spin transition densities (see Eq. (IV-60a)). Petrovich, et al. [Pe-82] noted that the monopole spin transition densities derived from both the pure LS-coupling and the Cohen-Kurath intermediate coupling p-shell wave functions produced Gamow-Teller matrix elements $\approx 18\%$ and $\approx 8\%$ larger than the experimental values. Also, Petrovich, et al. [Pe-82] did not obtain agreement between theory and their ${}^6\text{Li}(p,p'){}^6\text{Li}^*(3.563 \text{ MeV})$ data at $E_p \approx 25 \text{ MeV}$, with the theory failing to reproduce either the shape or magnitude of the angular distribution. This disagreement, however, was not attributed to uncertainties in the spin transition density, but Petrovich, et al. suggested that other reaction processes in addition to the direct, one-step reaction process were contributing to the transition. Furthermore, Cammarata and Donnelly [Ca-76], in their study of the reaction ${}^6\text{Li}(\gamma, \pi^+){}^6\text{He}$ near threshold, conclude that the ratio of the orbital current and spin transition densities derived from the Donnelly and Walecka wave functions is probably correct. Thus, as is the case for the 15.11-MeV state of ${}^{12}\text{C}$ [Mo-82], the disagreement between the simple DWIA analyses and the 3.563-MeV angular distributions and excitation function is difficult to explain as due to uncertainties in the transverse spin transition density or the spin-dependent piece of the πN interaction.

As explained above and in Chap. I, simple DWIA calculations using a well-tested spin-dependent component of the πN interaction and transverse spin transition densities obtained from fits to (e,e') data fail to reproduce both the shapes and magnitudes of the 3.563- and

15.11-MeV excitation functions. Furthermore, the energy-dependent anomalous shapes of both excitation functions are similar. Fig. V-12 shows the ratio of the experimental differential cross sections to the calculated differential cross sections for the excitation functions of the two unnatural-parity transitions. (The calculation employing the phenomenological transverse spin transition density is used for the ${}^6\text{Li}$ ratio). As mentioned in Chap. III, one cannot directly compare the 3.563-MeV excitation function to the 15.11-MeV excitation function, which is clearly evident from Figs. V-10 and V-11. From Eq. (IV-57a), the DWIA expression for πA inelastic scattering differential cross sections for the excitation functions for unnatural-parity transitions can be written as the product of two energy-dependent factors, the spin-dependent piece of the πN coupling and the distorted nuclear form factor at a fixed momentum transfer, and $\sin^2(\theta)$ [Si-81]. For the transition to the 15.11-MeV state of ${}^{12}\text{C}$, the strong energy dependence of the spin-dependent piece of the πN coupling is cancelled by the energy dependence of the distorted nuclear form factor [Si-81]. Thus, within the framework of the DWIA, the energy dependence of the 15.11-MeV excitation function follows $\sin^2(\theta)$. However, for the transition to the 3.563-MeV state of ${}^6\text{Li}$, the distortions are not as great, and the energy dependence of the spin-dependent piece of the πN coupling dominates. Therefore, using the DWIA, instead of having a gradually decreasing energy dependence, the 3.563-MeV excitation function is rounded and peaked. Taking the ratio of the experimental to theoretical excitation functions eliminates the difference of the effects of the distortions and allows direct comparison of the shapes of the 3.563- and 15.11-MeV excitation functions. From

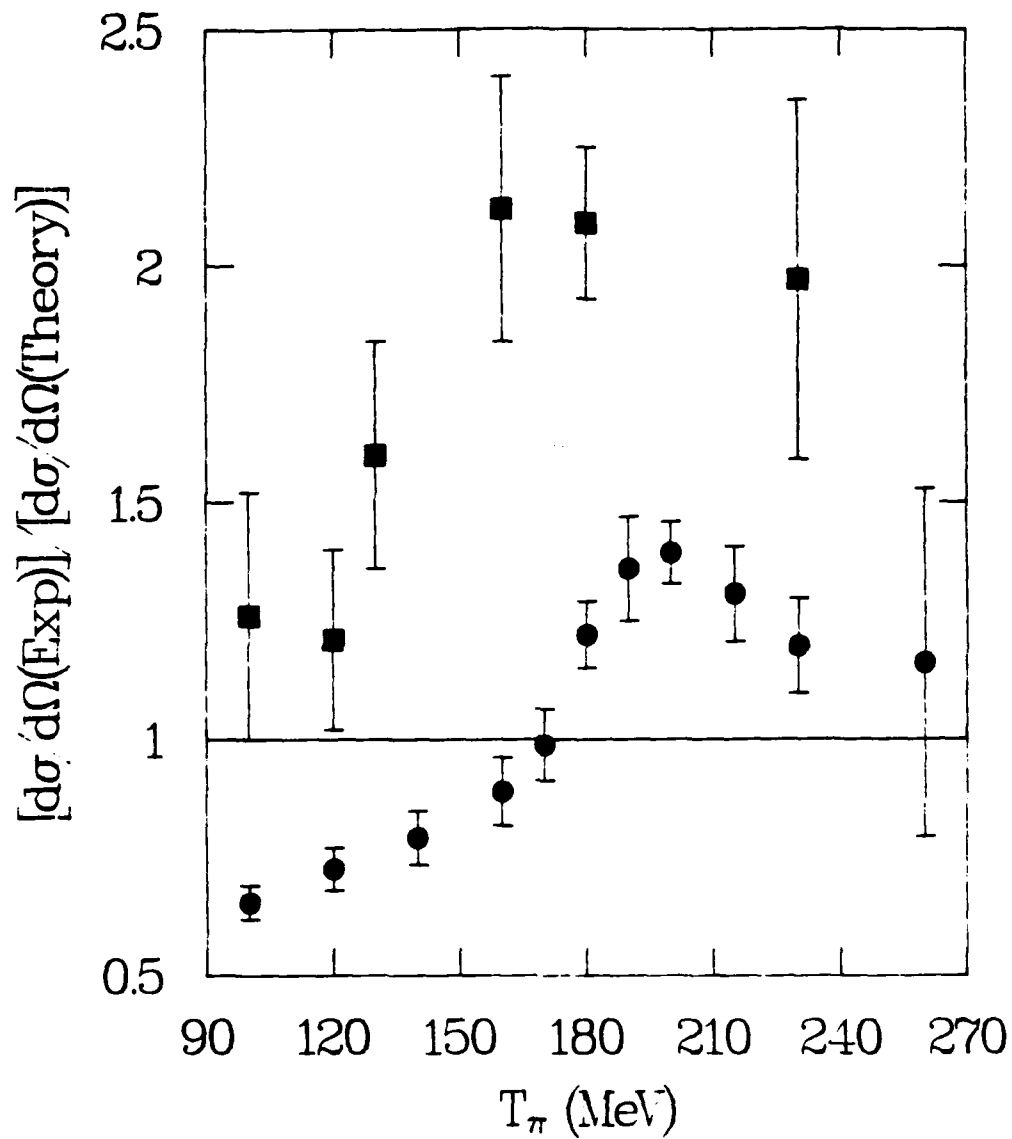


Fig. V-12: Ratio of the experimental differential cross sections to the calculated differential cross sections for the excitation functions of the two $\Delta S = \Delta T = 1$ transitions to the 3.563-MeV state of ${}^6\text{Li}$ (solid circles) and the 15.11-MeV state of ${}^{12}\text{C}$ (solid squares).

Fig. V-12, the ratios for the 3.563-MeV state of ${}^6\text{Li}$ and the 15.11-MeV state of ${}^{12}\text{C}$ are very similar in shape with the 3.563-MeV ratio approximately one-half the 15.11-MeV ratio at each incident pion energy. Both ratios deviate significantly from one and possess an energy dependence resembling the basic πN interaction.

Since the measured excitation functions for the unnatural-parity transitions to the 3.563-MeV state of ${}^6\text{Li}$ and the 15.11-MeV state of ${}^{12}\text{C}$ disagree in the same manner with the excitation functions predicted using the DWIA, and uncertainties in the transverse spin transition densities or the spin-dependent piece of the πN interaction are not likely explanations for the disagreement, perhaps another process, in addition to a one-step, impulse-approximation mechanism, contributes to both isovector transitions. A possible mechanism is the direct excitation of Δ -h components of the excited state wave functions, as proposed in [Mo-82], and a schematic diagram of the process is shown in Fig. V-13 [Mo-84a]. The diagram represents the process in which the incident pion excites a nucleon to a Δ particle; the Δ particle decays into a Δ particle plus a pion, leaving the nucleus in an excited Δ -h configuration. Since this mechanism involves the intermediate formation of a Δ particle, its contribution to the πA inelastic scattering differential cross sections should be resonant [Mo-84a]. Furthermore, the isospin of the Δ particle ($T=3/2$) and the isospin of the nucleon hole ($T=1/2$) couple only to a total $T=1$ or $T=2$; thus, resonant Δ -h production cannot contribute to excitation of the $T=0$, 12.71-MeV state of ${}^{12}\text{C}$.

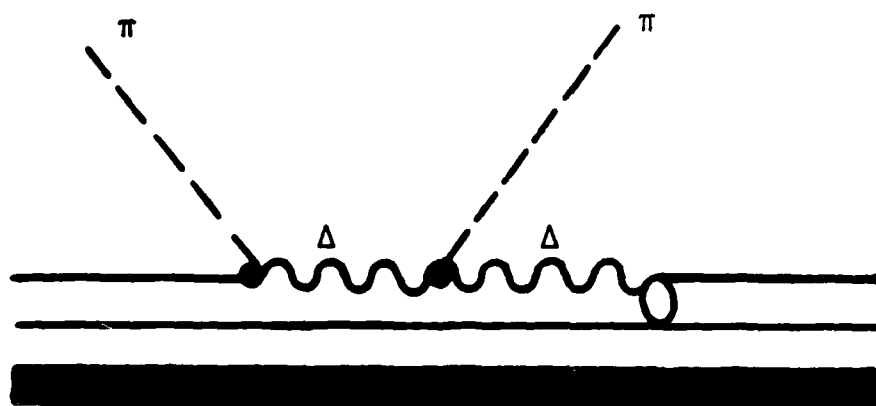


Fig. V-13: A schematic representation of the direct excitation of Δ -h components of the excited nuclear state wave function.

Within the Δ -h model interpretation, one can roughly estimate the amount of Δ -h admixture in the 3.563-MeV wave function. Using the peak of the 3.563-MeV excitation function ($T_{\pi} = 190$ MeV), the DWIA calculation which used the phenomenological transverse spin transition density, and the procedure of [Mo-82,Mo-84a] (see Appendix B), the estimated range of β (assumed to be real), the probability amplitude for the Δ -h component of the 3.563-MeV state, is $0.01 < \beta < 0.13$. This range of values of β is similar to that estimated for the 15.11-MeV state of ^{12}C , $0.026 < \beta < 0.096$ [Mo-84a]. However, if the direct excitation of Δ -h components is applicable to both $\Delta S=\Delta T=1$ transitions, comparison of the two excitation functions and DWIA calculations (see Fig. V-12) indicates that the resonant Δ -h scattering amplitude may interfere differently with the p-h scattering amplitude for the two transitions.

VI. SUMMARY

Using the EPICS system at the Clinton P. Anderson Meson Physics Facility, π^+ inelastic scattering data have been obtained for the transitions to the 3^+ , $T=0$, 2.185-MeV, 0^+ , $T=1$, 3.563-MeV, and 2^+ , $T=0$, 4.25-MeV states of ${}^6\text{Li}$. Simple DWIA calculations, involving only the spin-independent central component of the πN interaction and an isoscalar matter transition density derived from Cohen-Kurath intermediate coupling p-shell wave functions with the shape and strength parameters fixed from (e,e') data (transition to the 2.185-MeV state only), reproduce well both the 120- and 180-MeV (π^+, π^{+-}) angular distributions and the constant- q ($q \approx 109$ MeV/c) differential cross sections at $T_\pi = 100$ to 260 MeV for the natural-parity transitions to the 2.185- and 4.25-MeV levels. The agreement between the DWIA predictions and the (π^+, π^{+-}) data for these two transitions is continuing confirmation of the adequacy of the DWIA description for pion-induced transitions to nuclear states which are strongly excited.

DWIA calculations using a well-tested spin-independent component of the πN interaction and three different transverse spin transition densities obtained from fits to (e,e') data fail to reproduce the (π^+, π^{+-}) 120- and 180-MeV angular distributions and the (π^+, π^{+-}) excitation function at $q \approx 109$ MeV/c for the unnatural-parity transition to the weakly excited 3.563-MeV state. The measured excitation function exhibits an energy-dependent enhancement near incident pion energies of $T_\pi \approx 190$ MeV, with the difference between the data and DWIA calculations

very similar to the difference observed for the excitation function of the unnatural-parity transition to the 15.11-MeV state of ^{12}C .

As for the 15.11-MeV excitation function [Mo-82], uncertainties in the transverse spin transition density or inadequacies in the spin-dependent piece of the πN interaction are an unlikely explanation for the disagreement between the simple DWIA analyses and (π^+, π^{+-}) data for the transition to the 3.563-MeV level. Rather, a more likely explanation is that an additional process other than a one-step, impulse-approximation mechanism contributes to the $\Delta S = \Delta T = 1$ transition. A possible mechanism is resonant Δ -h production as was proposed in [Mo-82] to explain the anomalous excitation function for the transition to the 15.11-MeV state of ^{12}C . Within the Δ -h model interpretation, the peak of the 3.563-MeV excitation function is reproduced with an estimated probability amplitude for the Δ -h component of the 3.563-MeV state of $0.01 < \beta < 0.13$, a range of values of β consistent with the estimation of β needed to account for the peak of the 15.11-MeV excitation function, $0.026 < \beta < 0.096$ [Mo-84a]. However, the Δ -h and p-h scattering amplitudes may interfere differently for the two transitions. Whether or not the Δ -h model is the correct explanation for the anomalous 3.563-MeV excitation function, the (π^+, π^{+-}) measurements for the transition to the 3.563-MeV state of ^6Li provide another example of the failure of a simple DWIA description of transitions to weakly excited nuclear levels.

APPENDIX A

Data Tabulation

TABLE III-1: Differential cross sections for π^+ elastic scattering, ${}^6\text{Li}(\pi^+, \pi^+)$.

T_π (MeV)	θ_{lab} (deg)	$\theta_{\text{c.m.}}$ (deg)	q (fm $^{-1}$)	$d\sigma/d\Omega_{\text{c.m.}}$ (mb/sr)
100	33.0	34.3	0.559	27.2 ± 0.1
120	15.0	15.7	0.289	80.5 ± 0.4
120	21.0	21.9	0.404	74.1 ± 0.4
120	24.0	25.1	0.460	64.0 ± 0.3
120	27.0	28.2	0.517	49.1 ± 0.2
120	27.0	28.2	0.517	48.8 ± 0.2
120	29.0	30.3	0.554	43.0 ± 0.3
120	32.0	33.4	0.609	34.9 ± 0.2
120	32.0	33.4	0.609	35.1 ± 0.2
120	42.0	43.7	0.790	15.0 ± 0.1
120	47.0	48.9	0.878	8.2 ± 0.1
140	26.0	27.2	0.551	64.9 ± 0.3
160	24.0	25.2	0.557	80.5 ± 0.3
170	23.5	24.7	0.569	85.4 ± 0.5
180	20.0	21.1	0.505	103.4 ± 0.4
180	23.0	24.3	0.580	79.4 ± 0.3
180	23.0	24.3	0.580	79.5 ± 0.5
180	23.0	24.3	0.580	79.3 ± 0.4
180	23.0	24.3	0.580	80.9 ± 0.5
180	26.0	27.4	0.654	61.3 ± 0.3
180	29.0	30.6	0.727	44.7 ± 0.2
200	20.5	21.7	0.557	100.7 ± 0.7
215	19.5	20.7	0.558	107.1 ± 0.5
230	18.5	19.7	0.557	105.7 ± 0.7
230	18.5	19.7	0.557	103.4 ± 1.5
260	17.0	18.2	0.560	109.8 ± 0.8

TABLE III-2: Differential cross sections for π^+ inelastic scattering to the 3^+ , $T=0$, 2.185-MeV state of ${}^6\text{Li}$.

T_π (MeV)	θ_{lab} (deg)	$\theta_{\text{c.m.}}$ (deg)	q (fm^{-1})	$d\sigma/d\Omega_{\text{c.m.}}$ (mb/sr)
100	33.0	34.3	0.555	0.40 ± 0.02
120	15.0	15.7	0.288	0.27 ± 0.03
120	21.0	21.9	0.401	0.31 ± 0.04
120	24.0	25.1	0.458	0.57 ± 0.03
120	27.0	28.2	0.514	0.63 ± 0.03
120	27.0	28.2	0.514	0.59 ± 0.03
120	29.0	30.3	0.551	0.74 ± 0.04
120	32.0	33.4	0.606	0.80 ± 0.03
120	32.0	33.4	0.606	0.85 ± 0.04
120	42.0	43.7	0.786	0.97 ± 0.03
120	47.0	48.9	0.873	0.98 ± 0.03
140	26.0	27.2	0.548	1.11 ± 0.05
160	24.0	25.2	0.555	1.36 ± 0.06
170	23.5	24.7	0.567	1.78 ± 0.09
180	20.0	21.1	0.503	1.25 ± 0.07
180	23.0	24.2	0.577	1.74 ± 0.06
180	23.0	24.2	0.577	1.62 ± 0.08
180	23.0	24.2	0.577	1.59 ± 0.06
180	23.0	24.2	0.577	1.68 ± 0.09
180	26.0	27.4	0.651	1.97 ± 0.06
180	29.0	30.5	0.724	2.32 ± 0.06
200	20.5	21.7	0.555	1.96 ± 0.12
215	19.5	20.7	0.557	1.88 ± 0.09
230	18.5	19.7	0.555	2.03 ± 0.12
230	18.5	19.7	0.555	2.09 ± 0.25
260	17.0	18.2	0.558	2.06 ± 0.13

TABLE III-3: Differential cross sections for π^+ inelastic scattering to the 0^+ , $T=1$, 3.563-MeV state of ${}^6\text{Li}$.

T_π (MeV)	θ_{lab} (deg)	$\theta_{\text{c.m.}}$ (deg)	q (fm^{-1})	$d\sigma/d\Omega_{\text{c.m.}}$ ($\mu\text{b/sr}$)
100	33.0	34.3	0.553	39.8 ± 2.2
120	15.0	15.7	0.287	33.9 ± 3.0
120	21.0	21.9	0.400	43.6 ± 4.6
120	24.0	25.1	0.456	61.5 ± 5.6
120	27.0	28.2	0.512	41.3 ± 4.7
120	27.0	28.2	0.512	48.4 ± 4.1
120	29.0	30.3	0.549	57.0 ± 4.3
120	32.0	33.4	0.604	38.0 ± 3.3
120	37.0	38.6	0.694	32.8 ± 3.2
120	42.0	43.8	0.783	22.3 ± 3.2
120	47.0	48.9	0.870	12.3 ± 2.3
140	26.0	27.2	0.547	60.7 ± 4.4
160	24.0	25.2	0.553	68.5 ± 5.5
170	23.5	24.7	0.565	70.2 ± 7.0
170	23.5	24.7	0.565	80.7 ± 9.4
180	20.0	21.1	0.502	117.0 ± 7.6
180	23.0	24.3	0.576	100.0 ± 7.7
180	23.0	24.3	0.576	95.0 ± 9.4
180	23.0	24.3	0.576	62.0 ± 9.1
180	26.0	27.4	0.649	55.0 ± 5.6
180	29.0	30.6	0.722	43.1 ± 6.3
190	22.0	23.2	0.573	97.0 ± 12.0
190	22.0	23.2	0.573	89.5 ± 9.5
200	20.5	21.7	0.554	81.7 ± 6.4
200	20.5	21.7	0.554	97.0 ± 5.7
215	19.5	20.7	0.556	73.3 ± 5.6
230	18.5	19.7	0.554	55.9 ± 7.3
230	18.5	19.7	0.554	55.6 ± 6.0
260	17.0	18.2	0.558	33.1 ± 10.5

TABLE III-4: Differential cross sections for π^+ inelastic scattering to the 2^+ , $T=0$, 4.25-MeV state of ${}^6\text{Li}$.

T_π (MeV)	θ_{lab} (deg)	$\theta_{\text{c.m.}}$ (deg)	q (fm^{-1})	$d\sigma/d\Omega_{\text{c.m.}}$ (mb/sr)
100	33.0	34.3	0.552	0.15 ± 0.01
120	15.0	15.7	0.287	0.08 ± 0.01
120	21.0	21.9	0.400	0.09 ± 0.01
120	24.0	25.1	0.456	0.14 ± 0.01
120	27.0	28.2	0.511	0.26 ± 0.01
120	27.0	28.2	0.511	0.20 ± 0.01
120	29.0	30.3	0.548	0.28 ± 0.01
120	32.0	33.4	0.603	0.27 ± 0.01
120	37.0	38.6	0.693	0.10 ± 0.01
120	42.0	43.8	0.782	0.34 ± 0.01
120	47.0	48.9	0.868	0.27 ± 0.01
140	26.0	27.2	0.546	0.32 ± 0.01
160	24.0	25.2	0.553	0.51 ± 0.01
170	23.5	24.7	0.565	0.61 ± 0.02
170	23.5	24.7	0.565	0.64 ± 0.02
180	20.0	21.1	0.502	0.86 ± 0.02
180	23.0	24.3	0.575	0.69 ± 0.02
180	23.0	24.3	0.575	0.80 ± 0.02
180	23.0	24.3	0.575	0.76 ± 0.02
180	26.0	27.4	0.649	0.83 ± 0.01
180	29.0	30.6	0.721	0.88 ± 0.01
190	22.0	23.2	0.572	0.87 ± 0.03
190	22.0	23.2	0.572	0.98 ± 0.03
200	20.5	21.7	0.554	0.61 ± 0.01
200	20.5	21.7	0.554	0.74 ± 0.01
215	19.5	20.7	0.555	0.89 ± 0.01
230	18.5	19.7	0.554	0.71 ± 0.02
230	18.5	19.7	0.554	0.70 ± 0.01
260	17.0	18.2	0.557	0.71 ± 0.02

APPENDIX B

Estimation of β

Within the Δ -h model interpretation, the peak of the excitation function measured for the $\Delta S = \Delta T = 1$ transition to the 3.563-MeV state of ${}^6\text{Li}$ is reproduced with an estimated probability amplitude of the Δ -h component of the 3.563-MeV state of $0.01 < \beta < 0.13$. β is estimated in the following manner. The inelastic scattering differential cross section is written as [Mo-82, Mo-84a]

$$\frac{d\sigma}{d\Omega}(E, \theta) = |A(E, \theta) + \beta B(E, \theta)|^2, \quad (\text{B-1})$$

where $|A(E, \theta)|$ is the p-h scattering amplitude, $|B(E, \theta)|$ is the Δ -h scattering amplitude, and β is the probability amplitude for the Δ -h component of the 3.563-MeV state with respect to the ground state. The 3.563-MeV excitation function peaks at $T_\pi = 190$ MeV and $\theta_{\text{lab}} = 22^\circ$. Using this energy and angle and the DWIA analysis employing the phenomenological transverse spin transition density,

$$|A(E, \theta)| = 8.2 \sqrt{\mu\text{b/sr}}. \quad (\text{B-2})$$

$|B(E, \theta)|$ may be roughly estimated by examining the isospin dependence of cross sections for $(T_i, T_{zi}) \rightarrow (T_f, T_{zf})$ transitions involving only p-h configurations or Δ -h configurations of the final state with respect to the initial state, and by assuming a simple Δ -h

model for the 3.563-MeV level. The relative isospin dependence is determined using Lee and Lawson's [Le-80a] extraction of the isospin dependence of the πA scattering amplitude in the DWIA formalism, and modifying their result to include a Δ in the final state. Using $P_{3,3}$ dominance, which simplifies Lee and Lawson's result, the ratio of cross sections for a $(T_i=0, T_{zi}=0) \rightarrow (T_f=1, T_{zf}=0)$ transition for the final state being a Δ -h configuration to the final state being a p-h configuration is 0.625/0.25. To determine the possible Δ -h configurations of the 3.563-MeV state with respect to the ground state, an extremely simple model is used. In this model, the 3.563-MeV state is a $(1p_{1/2} \times 1p_{3/2}^{-1})_{J=0, T=1}$ nucleon-hole configuration with respect to the ground state. (This configuration was chosen from the dominant one body density matrix element predicted from Cohen-Kurath intermediate coupling p-shell wave functions.) One could expect the following Δ -h configurations to mix with the above p-h configuration: $(1p_{1/2} \times 1p_{3/2}^{-1})_{J=0, T=1}$, $(1p_{3/2} \times 1p_{3/2}^{-1})_{J=0, T=1}$, and $(1p_{5/2} \times 1p_{3/2}^{-1})_{J=0, T=1}$. With Cohen-Kurath intermediate coupling p-shell wave functions, the inelastic scattering differential cross section is quenched by a factor of 2.25 from the differential cross section computed with the above simple p-h configuration. Assuming that this quenching is not present for the Δ -h configurations and that the three transitions involving a Δ , $p_{3/2} \rightarrow p_{5/2}$, $p_{3/2} \rightarrow p_{3/2}$, $p_{3/2} \rightarrow p_{1/2}$, contribute coherently to the differential cross section and are weighted as $\sqrt{2j_{\Delta} + 1}$,

$$|B(E, \theta)| \propto \frac{\sqrt{6} + \sqrt{4} + \sqrt{2}}{\sqrt{2}} \times \frac{\sqrt{0.625}}{\sqrt{0.25}} \times \sqrt{2.25} |A(E, \theta)|^2. \quad (B-3a)$$

The only other factor which needs to be considered is the ratio of coupling constants $f_{\Delta\Delta\pi}/f_{\Delta N\pi}$. This ratio can be obtained from the quark model and is $f_{\Delta\Delta\pi}/f_{\Delta N\pi} = \sqrt{25/8}$ [Mo-84a]. Thus,

$$|B(E, \theta)| = \frac{\sqrt{6} + \sqrt{4} + \sqrt{2}}{\sqrt{2}} \times \frac{\sqrt{0.625}}{\sqrt{0.25}} \times \frac{\sqrt{25}}{\sqrt{8}} \times \sqrt{2.25 |A(E, \theta)|^2} . \quad (B-3b)$$

Substituting in the value of $|A(E, \theta)|$ from Eq. (B-2),

$$|B(E, \theta)| = 143 \sqrt{\mu b / sr} . \quad (B-3c)$$

With Eqs. (B-1) through (B-3) and assuming that the two scattering amplitudes, p-h and Δ -h, are completely in phase or are completely out of phase, $0.01 < \beta < 0.13$, where β is assumed to be real.

APPENDIX C

Dissertation Paper

Pion Inelastic Scattering to the Low-Lying Excited States of ${}^6\text{Li}$

R. R. Kisiah, M. D. Brown^a, C. J. Harvey^b, D. S. Oakley,
D. P. Saunders^c, P. A. Seidl, and C. F. Moore
University of Texas at Austin, Austin, TX 78712

W. B. Cottingham, R. W. Garnett, Steven J. Greene^d,
G. A. Luna^a, and G. R. Burleson
New Mexico State University, Las Cruces, NM 88003

D. B. Holckamp^d
University of Minnesota, Minneapolis, MN 55455

ABSTRACT

The excitation function for π^+ inelastic scattering to the 0^+ , $T=1$, 3.563-MeV level of ${}^6\text{Li}$ has been measured at a constant momentum transfer $q = 109 \text{ MeV}/c$ for incident pion energies from 100 to 260 MeV. Although the differential cross sections extracted for the natural-parity transitions to the 3^+ , $T=0$, 2.185-MeV and 2^+ , $T=0$, 4.25-MeV levels are well reproduced within the framework of the distorted-wave impulse approximation (DWIA), DWIA calculations fail to reproduce the anomalous excitation function observed for the transition to the 3.563-MeV level. The shape of the 3.563-MeV excitation function is similar to that previously observed for π^\pm inelastic scattering to the 1^+ , $T=1$, 15.11-MeV state of ${}^{12}\text{C}$ [C. L. Morris, et al., Phys. Lett. 108B, 172 (1982)]. The same mechanism may be responsible for the observed excitation functions of both $\Delta S=\Delta T=1$ transitions. A possible mechanism is the previously proposed direct excitation of Δ particle-nucleon hole (Δ -h) components in the wave functions.

PACS numbers: 25.80.Dj, 25.80.Fm

[NUCLEAR REACTIONS: ${}^6\text{Li}(\pi^+, \pi^+)$; $100 < T_\pi < 260 \text{ MeV}$; measured $\sigma(\theta)$; DWIA analysis; deduced κ , the matrix element between Δ -h and p-h basis states for the 3.563-MeV state]

-2-

I. INTRODUCTION

Comparison of pion-inelastic-scattering data in the energy range of the (3,3) resonance with calculations using the distorted-wave impulse approximation (DWIA) and well-known transition densities, indicates that a single-step, impulse approximation is an adequate description for pion-induced transitions to nuclear states which are strongly excited. For example, Lee and Kurath¹ and Lee and Lawson,² using the DWIA and transition densities derived from shell-model wave functions, qualitatively reproduce angular distributions for pion inelastic scattering to excited states of various p- and sd-shell nuclei. Morris, *et al.*³ and Boyer, *et al.*⁴ obtain good agreement between angular distributions and DWIA calculations, which use empirical transition densities determined from electron-scattering data, for inelastic scattering to low-lying collective states in ^{12}C , ^{40}Ca , ^{42}Ca , ^{44}Ca , and ^{48}Ca . Furthermore, the excitation functions measured at a constant momentum transfer for the unnatural-parity transitions to the 4^- , 19.25-MeV state and 2^- structure at approximately 18.4 MeV in ^{12}C (Ref. 5) and the $9/2^+$, 9.5-MeV state in ^{13}C (Ref. 6) decrease with increasing incident pion energy as predicted by the DWIA.⁷ Within the framework of the DWIA, these unnatural-parity transitions are particularly simple, involving only the spin-dependent part of the effective pion-nucleus inelastic interaction and the transverse spin transition density.⁸ In particular, for the unnatural-parity transitions to states of stretched configuration in ^{16}O (4^- , 17.79-, 18.98-, and 19.80-MeV levels) and ^{28}Si (6^- , 11.58- and 14.36-MeV levels), Carr, *et al.*⁹ satisfactorily reproduce the measured angular distributions with DWIA calculations using spin transition densities fixed from (e,e') and (p,p') data.

-3-

For pion-induced excitation of nuclear states that are weakly excited by a one-step, impulse-approximation mechanism, nuclear medium effects and multistep processes may be important and there may not be good agreement between the pion-inelastic-scattering data and DWIA calculations, as for the above strongly excited examples. This is indeed the case for the $T=1$ member of the weakly excited 1^+ doublet, 12.71 MeV ($T=0$) and 15.11 MeV ($T=1$), of ^{12}C .¹⁰ Cohen-Kurath wave functions¹¹ describe the 15.11- and 12.71-MeV states as near analogs, and this description for the spin transition densities is supported by (e, e') data.¹² Calculations using a one-step, DWIA mechanism predict the ratio of cross sections for unnatural-parity transitions to members of an analog-antianalog pair to be four to one.^{8,10} Both the constant-momentum-transfer-excitation function and the angular distributions for the 12.71-MeV state are well reproduced by DWIA calculations. However, the measured ratio of four times the averaged π^+ and π^- differential cross sections for the 15.11-MeV state to the averaged π^+ and π^- differential cross sections for the 12.71-MeV state deviates significantly from one, especially at energies near 180 MeV (ratio is approximately three), and displays a rapidly varying energy dependence. (Averaging the π^+ and π^- differential cross sections removes the effect of isospin mixing between the two states on the ratio to better than 1%.¹⁰) Also, DWIA calculations do not agree with the 15.11-MeV angular distributions at energies near the (3,3) resonance.¹²

Uncertainties in the spin transition density or inadequacies in the spin-dependent piece of the effective pion-nucleus interaction are an unlikely explanation¹⁰ for the anomalous excitation function for the $\Delta S=\Delta T=1$ transition to the 15.11-MeV level of ^{12}C . Rather, a more likely explanation is that an additional process other than a one-step, impulse-approximation mechanism is contributing to the isovector transition. Therefore, to investigate further pion-induced excitation of weakly excited nuclear levels, we consider the

-4-

$\Delta S = \Delta T = 1$ transition from the 1^+ , $T=0$, ground state of ${}^6\text{Li}$ to the 0^+ , $T=1$, 3.563-MeV level. We have measured an excitation function for π^+ inelastic scattering to the 3.563-MeV state of ${}^6\text{Li}$ at incident pion energies from 100 to 260 MeV and partial angular distributions at 120 and 180 MeV. We also present in Table I the differential cross sections for elastic scattering and for inelastic scattering to the 2.185- and 4.25-MeV states. The 2.185- and 4.25-MeV differential cross sections are compared to microscopic DWIA calculations using transition densities derived from Cohen-Kurath wave functions.¹¹ The 3.563-MeV differential cross sections are compared to microscopic DWIA calculations using spin transition densities derived from Cohen-Kurath wave functions,¹¹ the empirical shell-model wave functions of Donnelly and Walecka,¹³ and the phenomenological wave functions of Bergstrom, *et al.*¹⁴

II. DATA ACQUISITION AND REDUCTION

The data were collected using the Energetic Pion Channel and Spectrometer (EPICS) system¹⁵ at the Clinton P. Anderson Meson Physics Facility (LAMPF). Four separate targets consisting of sheets of enriched lithium, $>98\%$ ${}^6\text{Li}$, fabricated by the Oak Ridge National Laboratory were used during the experiment. Two of the targets, with dimensions of 22.9 cm \times 15.2 cm and areal densities of 202 mg/cm² and 100 mg/cm², were used for approximately one-half of the total data acquisition and contained no discernible contamination. The remaining two targets, with dimensions of 20 cm \times 10 cm and areal densities of 205 mg/cm² and 95 mg/cm², were contaminated by exposure to the air during shipping. Hydrogen contamination was negligible in the thick 20 cm \times 10 cm target ($<1\%$) but appreciable in the thin 20 cm \times 10 cm target ($\approx 5\%$). Since we

-5-

clearly observed the 6.13- and 6.92-MeV states of ^{16}O in some π^+ Q-value spectra but never observed any inelastic peaks of ^{14}N , we assumed the heavy impurity to be ^{16}O . With this assumption, the total amounts of impurities for the thick and thin 20 cm \times 10 cm targets were 2.3% and 18%, respectively. A comparison of differential cross sections for the elastic scattering from ^6Li , extracted from the contaminated and uncontaminated targets at the same incident pion energy and scattering angle, indicate that the estimated amounts of impurities are accurate within $\pm 1\%$. ^7Li was not detected in any of the targets.

Fig. 1 shows the Q-value spectrum for $^6\text{Li}(\pi^+, \pi^+)$ using the 205 mg/cm 2 , 20 cm \times 10 cm target for $T_\pi = 140$ MeV and $\theta_{\text{LAB}} = 26^\circ$. This spectrum is representative of the spectra used for determination of cross sections for excitation of the 3.563- and 4.25-MeV levels. Although the experimental resolution was not the best for the 205 mg/cm 2 target (240 keV full width at half maximum (FWHM)), the 3.563-MeV level is clearly resolved from the large continuum background and the 4.25-MeV level. The discontinuity in the Q-value spectrum between the ground state and 2.185-MeV state is an artifact of the hardware veto of elastic counts used to limit data rates during data acquisition by rejecting the majority of events with a Q value below ≈ 1.2 MeV. The elastic and 2.185-MeV cross sections were determined without the use of this hardware veto (see the insert in Fig. 1).

Peak areas were extracted from the Q-value spectra using the computer program LOAF.¹⁷ The backgrounds under the elastic and 3^+ peaks were fitted with a first-order polynomial, while the backgrounds under the 0^+ and 2^+ peaks were fitted with a third-order polynomial. Line shapes for the elastic and 3^+ peaks were extracted from the spectra for each target at each incident pion energy because the resolution varied with energy from 200 keV (220 keV) FWHM at $T_\pi = 100$ MeV to 260 keV (260 keV) FWHM at $T_\pi = 260$ MeV for the thin (thick)

-6-

targets. The line shape of the 0^+ peak was taken to be the same as the 3^+ , while the line shape of the 2^+ was constructed by folding the line shape used for the 3^+ with a Lorentzian of 680 keV FWHM. The peak positions were constrained to be 0.0, 2.185,¹⁸ 3.563,¹⁸ and 4.25 MeV. Both the position and natural width of the 2^+ level, 4.25 ± 0.02 MeV and 680 ± 20 keV, were determined from fits to several spectra where this state was predominant. Previous determinations from other experiments are 4.27 ± 0.04 MeV and 690 ± 120 keV,¹⁹ 4.29 ± 0.02 MeV and 850 ± 50 keV,²⁰ and 4.30 ± 0.01 MeV and 480 ± 80 keV.²⁰ The 5.37- and 5.65-MeV states were not observed in the spectra, and thus no attempt was made to include them in the fits.

The consistency of the fits to the various Q-value spectra was checked by extracting areas for 100 keV wide segments of background centered about 3.563 and 4.25 MeV. Plots of the background yields for both the 3.563- and 4.25-MeV segments resulted in smooth and continuous angular distributions at 120 and 180 MeV. Also the background yields versus incident pion energy are smooth and continually increasing. We therefore have indication that our extraction of the peak areas from the large continuum background is consistent at different incident pion energies and scattering angles.

Experimental yields were measured for $\theta_{\text{LAB}} > 25^\circ$ by monitoring the EPICS channel beam flux with an ionization chamber located downstream from the scattering target. For $\theta_{\text{LAB}} < 25^\circ$ the ionization chamber was not used since it partially blocked the spectrometer entrance. For these angles, relative normalization was accomplished through an ionization chamber located within the pion production target cell and a charge integrating toroidal coil located upstream of the pion production target. Monitoring of the ratio of the ionization chamber current to the currents from these two monitors of the proton beam showed $< 2\%$ fluctuations for $\theta_{\text{LAB}} > 25^\circ$, establishing them as reliable beam flux monitors. Absolute cross sections were calculated by

-7-

normalizing to π^+ scattering on hydrogen (CH_2 targets of dimensions 22.9 cm \times 15.2 cm and 20 cm \times 10 cm corresponding to the two different sizes of ^6Li targets) using Coulomb-corrected phase-shift predictions from the computer code CROSS²¹ with the phase shifts of Rowe, Salomon, and Landau.²²

The data were corrected for computer live time, multiwire proportional drift chamber efficiency, pion survival fraction through the spectrometer, and the variation of the spectrometer's solid angle with pion momentum. The quoted error bars are statistical only. Total systematic errors are estimated to be $\pm 7\%$ due to uncertainties of $\pm 3\%$ in chamber efficiency, $\pm 3\%$ in pion survival fraction, $\pm 2\%$ in the spectrometer's solid angle variation with momentum in the spectrometer, $\pm 3\%$ in channel beam monitoring, and $\pm 3\%$ in normalization to π^+ scattering on hydrogen. Furthermore, the data for the 3.563- and 4.25-MeV states contain additional systematic errors of $\pm 15\%$ and $\pm 10\%$, respectively, due to the uncertainty in the fitting of the large continuum background and the uncertainty in the position and width of the 2^+ state. These systematic errors were inferred by varying the order of the polynomial fit to the background, and by varying the position and width of the 2^+ state from 4.23 to 4.27 MeV and 660 to 700 keV.

IV. DATA ANALYSIS

A. Elastic scattering analysis

The first-order, zero-range, impulse-approximation elastic calculations were performed with a variation²³ of the coordinate-space computer program PIRK,²⁴ which solves a Klein-Gordon equation, using only linear terms in the

-8-

optical-model potential. For all ${}^6\text{Li}$ elastic calculations, we used the Kisslinger form²⁵ of the optical-model potential given by

$$V(r) = -Ak_{\pi}^2 b_0 \rho(r) + Ab_1 \vec{\nabla} \rho(r) \cdot \vec{\nabla}, \quad (1)$$

where $\rho(r)$ is the nucleon density normalized to unity, k_{π} is the lab momentum of the incident pion, and A is the mass of the target. The complex b_0 and b_1 coefficients are constructed from the pion-nucleon phase shifts of Rowe, Salomon, and Landau²² evaluated at an energy of 30.0 MeV below the incident pion beam energy. This procedure has been demonstrated by Cottingham and Holtkamp²³ to give better agreement to pion-elastic-scattering data for nuclei ranging from ${}^9\text{Be}$ to ${}^{208}\text{Pb}$. This phenomenological shift in the collision energy is a method for adjusting the pion-nucleus kinematics so as optimally to factorize the optical-model potential (see Ref. 12 for a discussion of the above procedure). The proton matter density distribution was characterized by a three-parameter phenomenological distribution taken from elastic electron scattering²⁶ with the finite size of the proton charge removed. This distribution has the form

$$\rho(r) = Z/(8\pi^{3/2}) \left\{ (1/a^3) \exp(-r^2/4a^2) - (c^2(6b^2 - r^2)/4b^7) \exp(-r^2/4b^2) \right\}, \quad (2)$$

with $a = 0.928$ fm, $b = 1.26$ fm, and $c = 0.48$ fm.²⁶ This phenomenological distribution was also used for the neutron matter density distribution.

The present 120- and 180-MeV π^+ elastic data, the SIN 164-MeV π^- elastic data,²⁷ and elastic calculations are presented in Fig. 2. Since the elastic optical potential is used for the generation of the distorted waves for inelastic calculations, the good agreement indicates adequate handling of the distortions.

B. Inelastic scattering analysis

-9-

The inelastic calculations presented in this paper are Born approximation, DWIA calculations in which the pion-nucleus transition amplitude is a configuration-space, folded product of a distortion function and form factor. The distortion function, a product of initial and final pion distorted waves, is computed from the elastic optical-model potential employed in the elastic calculations. Calculation of the form factor, whose specific form depends upon the inelastic transition and is the folded product of the pion-nucleon interaction and the nuclear transition density, uses the frozen-target approximation assuming on-shell kinematics and a collision energy obtained from the elastic calculations. For inelastic calculations using pure LS-coupling and Cohen-Kurath intermediate coupling wave functions,¹¹ we use a modification of the generalized inelastic scattering potential code ALLWRLD²⁸ to calculate the form factor. The harmonic oscillator parameters and renormalization constants include the standard center-of-mass correction needed when using shell-model wave functions. The distortion function and differential cross sections are then generated from the code UTDWPI.²⁹ For all other inelastic calculations we use only the code UTDWPI and no center-of-mass correction is included in the harmonic oscillator parameters and renormalization constants. However, these inelastic calculations use center-of-mass corrected form factors with the correction being applied in momentum space.

1. 3^+ , T=0, 2.185-MeV state

Electron-scattering data indicate that the natural-parity transition to the 2.185-MeV level of ${}^6\text{Li}$ is almost completely longitudinal, with measurements in the region of $q = 0.7$ to 1.8 fm^{-1} yielding a transverse form factor which is less than 2% of the longitudinal form factor.³⁰ Since the spin-orbit transition density is approximately zero, the form factor involves only the central

-10-

component of the pion-nucleon interaction and the isoscalar matter transition density.³¹ Inelastic calculations for this natural-parity transition have been performed using two different transition densities derived from pure LS-coupling and Cohen-Kurath intermediate coupling p-shell wave functions. Each calculation employed equal transition densities for the protons and neutrons. The harmonic oscillator parameter, α , and renormalization constant for the transition density derived from the pure LS-coupling p-shell wave functions are 0.534 fm^{-1} and 2.03. These values were required to fit the inelastic-electron-scattering data considered in Ref. 32 and give good agreement between theory and experiment for the ${}^6\text{Li}(p,p'){}^6\text{Li}^*(2.185 \text{ MeV})$ differential cross sections at $E_p = 25$ and 45 MeV .³² The transition density derived from the intermediate coupling p-shell wave functions uses $\alpha = 0.558 \text{ fm}^{-1}$ and a renormalization constant of 1.93, again determined from (e,e') data.³³ Electron-scattering longitudinal form factors from Refs. 14 and 34 are shown in Fig. 3. The solid (dashed) curves correspond to the transition densities computed from the pure LS- (intermediate) coupling p-shell wave functions. Both theoretical form factors are similar, with the intermediate coupling form factor in better agreement with the electron-scattering data. The π^+ 2.185-MeV data and calculations for $T_\pi = 120$ and 180 MeV are presented in Fig. 4. Fig. 5 shows the data and calculations for $T_\pi = 100$ to 260 MeV with the differential cross sections corresponding to a constant momentum transfer $q = 109 \text{ MeV}/c$. From the data and calculations, the first maxima of the angular distributions for the 2.185-MeV state are expected to be at $q \approx 164 \text{ MeV}/c$. The intermediate coupling calculation is in good agreement with both the 120- and the 180-MeV experimental angular distributions. Furthermore, this calculation reproduces well the constant- q experimental differential cross sections, considering that the theoretical values plotted in Fig. 5 are taken from the steep forward slope of the various angular distributions where errors would produce the greatest

-11-

variations. The pure LS-coupling calculation yields similar shapes for the 120- and 180-MeV angular distributions and the constant- q differential cross sections as does the intermediate coupling calculation but overestimates the magnitudes. Such disagreement suggests that the renormalization constant is too large.

2. 2^+ , $T=0$, 4.25-MeV state

The electron-scattering form factors for both natural-parity transitions to the 2.185- and 4.25-MeV levels have the same dependences on the momentum transfer.³⁵ Therefore, the transition to the 4.25-MeV state is principally longitudinal, and we treat this transition as completely analogous to the excitation of the 2.185-MeV level. However, even though the 4.25-MeV state is observed in (e,e') spectra, a detailed form factor has not been measured because of this state's large natural width, the overlapping 5.37-MeV state, and the large continuum background.³⁶ We therefore cannot deduce a transition density from electron-scattering data as was the case for the 2.185-MeV transition. Thus, we simply used a transition density derived from Cohen-Kurath intermediate coupling p -shell wave functions with $\alpha = 0.52 \text{ fm}^{-1}$ and a renormalization constant of 0.82 determined from fitting only our (π^+, π^+') data at $T_\pi = 120$ and 180 MeV. This transition density yields a radiative width, $\Gamma_{\gamma 0}^{(E2)}$, of 3.02 eV in agreement with the experimental value of $5.4 \pm 2.8 \text{ eV}$.¹⁹ The 4.25-MeV experimental and theoretical 120- and 180-MeV angular distributions and the constant- q differential cross sections are shown in Figs. 6 and 7, respectively. The agreement is not as good as for the 2.185-MeV state but is very reasonable considering the difficulties in extracting the cross sections and possible uncertainties in the transition density.

-12-

3. 0^+ , $T=1$, 3.563-MeV state

As is the case for the natural-parity transitions to the 2.185- and 4.25-MeV levels of ${}^6\text{Li}$, the Born approximation DWIA description of the pion-induced unnatural-parity transition to the 3.563-MeV state is straightforward, involving only a single component of the pion-nucleon interaction and a single nuclear transition density. Using a single scattering model, the spin-dependent piece of the interaction is represented by the zero-range spin-orbit operator,⁹ and the transition density is the transverse spin transition density. We employed three different transverse spin transition densities determined from fits to various (e,e') measurements but compared to the most recent sets of (e,e') data (Refs. 14 and 37). The proton and neutron transition densities were taken to be equal. The reasons for using three transition densities are: (1) The p-shell harmonic oscillator basis is known to result in a poor description of the 3.563-MeV electron-scattering transverse form factor over the entire second lobe, $q > 1.4 \text{ fm}^{-1}$. We therefore employ one transition density which reproduces both the first and second lobes of the form factor. (2) Since there is no analog to the 3.563-MeV state as is the situation for the 12.71-/15.11-MeV analog-antianalog pair of ${}^{12}\text{C}$, any anomalies in the 3.563-MeV excitation function depend upon comparison of theory with data and not data for analogs as for the 15.11-MeV level. Thus, accurate spin transition densities are imperative.

The first analysis for the spin-flip transition to the 3.563-MeV state used a spin transition density derived from Cohen-Kurath intermediate coupling p-shell wave functions. The harmonic oscillator parameter was chosen to be 0.518 fm^{-1} from the work of Petrovich, *et al.*,³² who fitted low q electron-scattering data using pure LS-coupling p-shell wave functions. We used a renormalization constant of 0.97. Petrovich, *et al.* conclude that both sets

-13-

of theoretical wave functions provide an adequate description of the experimental static moments and transition probabilities of ${}^6\text{Li}$ with the exception of the quadrupole moment.³² However, we chose the intermediate coupling p-shell wave functions because they give a slightly better fit to the most recent sets of (e,e') data (Refs. 14 and 37) for the inelastic M1 form factor. Fig. 8 shows the calculated transverse form factor (solid curve) and (e,e') data for the transition to the 3.563-MeV state.

The second calculation employed a spin transition density obtained from the empirical shell-model wave functions of Donnelly and Walecka.¹³ These wave functions are almost identical to the pure LS-coupling p-shell wave functions. Using p-shell harmonic oscillator radial wave functions for the valence nucleons, Donnelly and Walecka determined the one body density matrix elements from normalization conditions and from fits to the ground state magnetic dipole and electric quadrupole moments and the M1 form factors for electron elastic and inelastic scattering for $q < 1.01 \text{ fm}^{-1}$.¹³ A harmonic oscillator parameter¹³ $\alpha = 0.493 \text{ fm}^{-1}$ and a renormalization constant of 0.96 were used in our calculations. The resultant inelastic M1 form factor (dashed curve) is compared to the (e,e') data in Fig. 8.

The third analysis used a phenomenological spin transition density based on the work of Bergstrom, et al.¹⁴ This transition density was derived in the same manner as the transition density of Donnelly and Walecka except that we fitted the (e,e') data of Refs. 14 and 37, which extend to $q = 2.96 \text{ fm}^{-1}$, and assumed a polynomial form for the p-shell radial transition density. The wave functions for the ${}^6\text{Li}$ ground state and 3.563-MeV state were taken to be described by the SASK-A amplitudes of Bergstrom, et al.¹⁴ The radial transition density has a phenomenological form

$$R^2(r) = e^{-r^2/b^2}(a_2 r^2 + a_4 r^4 + a_6 r^6) \quad , \quad (3)$$

with $b = 2.02 \text{ fm}$, $a_2 = 6.625 \times 10^{-2} \text{ fm}^{-5}$, $a_4 = -5.036 \times 10^{-3} \text{ fm}^{-7}$,

-14-

$a_6 = 1.967 \times 10^{-4} \text{ fm}^{-3}$, yielding a reduced χ^2 of 1.32 from a fit to the inelastic M1 form factor, which is presented in Fig. 8 (chain-dot curve).

The π^+ data and DWIA calculations at $T_\pi = 120$ and 180 MeV for the spin-flip transition to the 3.563-MeV state are shown in Fig. 9. At 120 MeV the three spin transition densities give equivalent shapes for the angular distributions in the range of our data, $15.7^\circ < \theta_{\text{c.m.}} < 48.9^\circ$. All calculations predict the correct location for the first maximum of $\theta_{\text{c.m.}} = 28^\circ$. However, the Cohen-Kurath intermediate coupling (solid curve), Donnelly and Walecka (dashed curve), and phenomenological (chain-dot curve) calculations overestimate the magnitude of the first maximum by 18%, 29%, and 38%, respectively. The three spin transition densities yield similar results for the shape of the 180-MeV angular distribution through the first minimum but differ through the second maximum and minimum. Each calculation underestimates the magnitude of the first maximum by at least 26%.

The π^+ 3.563-MeV excitation function data and DWIA analyses are presented in Fig. 10. The momentum transfer for the excitation function was determined to be $q = 109 \text{ MeV}/c$ from the first maximum of the 120-MeV angular distribution. All other data points for the various energies are within $\pm 4\%$ of this q . None of the spin transition densities predict the measured shape and magnitude of the 3.563-MeV excitation function. The Cohen-Kurath intermediate coupling, Donnelly and Walecka, and phenomenological calculations disagree with the data by at least $\pm 20\%$ at both the low and high incident pion energies.

V. DISCUSSION AND RESULTS

-15-

The disagreement between theory and data for the 120- and 180-MeV angular distributions and excitation function for the unnatural-parity transition to the 3.563-MeV state is difficult to understand, as is the disagreement observed for the unnatural-parity transition to the 15.11-MeV state of ^{12}C . For comparison, the 12.71- and 15.11-MeV excitation functions along with DWIA calculations as described in Ref. 10 are shown in Fig. 11. As noted in the introduction, a simple DWIA description of pion-nucleus inelastic scattering, which uses a single component of the pion-nucleon interaction and a single transition density, has been successful in describing unnatural-parity transitions in many nuclei. Using the zero-range spin-orbit operator and a spin transition density derived from Cohen-Kurath p-shell wave functions, Morris, *et al.*¹⁰ adequately reproduced the experimental 12.71-MeV excitation function. Furthermore, Cottingham, *et al.*¹² adequately describe the 12.71-MeV angular distributions for $T_\pi = 100$ to 260 MeV. Even though there is an energy-dependent enhancement near $T_\pi = 180$ MeV in the 15.11-MeV excitation function,¹⁰ the low-energy ($T_\pi = 100$ and 116 MeV) angular distributions for this state are reproduced by simple DWIA calculations.¹² Using the same zero-range spin-orbit operator and three different spin transition densities, we cannot adequately describe either the 120-MeV and 180-MeV angular distributions or the excitation function of the transition to the 3.563-MeV state. However, we are able to reproduce the angular distributions and constant- q differential cross sections at energies from $T_\pi = 100$ to 260 MeV for the natural-parity transitions to the 2.185- and 4.25-MeV levels of ^6Li using only the central component of the pion-nucleon interaction and transition densities derived from Cohen-Kurath p-shell wave functions. The configuration-space, zero-range form of the spin-dependent component of the pion-nucleon interaction of Carr, *et al.*⁹ is most likely not in error. Furthermore, the transition densities we used for the transition to the 3.563-MeV level yield inelastic M1 form factors which agree with the (e, e')

-16-

data for $q < 1.4 \text{ fm}^{-1}$ (see Fig. 8), which is a range of q that adequately covers the $q = 0.55 \text{ fm}^{-1}$ at which the excitation function was measured. However, this does not eliminate uncertainties in the spin transition densities since the electron-scattering inelastic M1 form factor depends upon both the orbital and spin transition densities. Petrovich, *et al.*³² noted that the monopole spin transition densities derived from both the pure LS-coupling and the Cohen-Kurath intermediate coupling p-shell wave functions produced Gamow-Teller matrix elements 17.9% and 8.4% larger than the experimental values. Also, Petrovich, *et al.*³² did not obtain agreement between theory and their ${}^6\text{Li}(p,p'){}^6\text{Li}^*(3.563 \text{ MeV})$ data at $E_p = 25 \text{ MeV}$, with the theory failing to reproduce either the shape or magnitude of the angular distribution. This disagreement, however, was not attributed to uncertainties in the spin transition density, but Petrovich, *et al.* suggested that other reaction processes in addition to the direct, one-step reaction process were contributing to the transition. Furthermore, Cammarata and Donnelly,³⁸ in their study of the reaction ${}^6\text{Li}(\gamma,\pi^+){}^6\text{He}$ near threshold, conclude that the ratio of the orbital and spin transition densities derived from the Donnelly and Walecka wave functions¹³ is probably correct. Thus, as is the case for the 15.11-MeV state of ${}^{12}\text{C}$,¹⁰ the disagreement between our simple DWIA analyses and the 3.563-MeV angular distributions and excitation function is difficult to explain as due to uncertainties in the spin transition density or the spin-dependent piece of the pion-nucleus inelastic interaction.

Since simple DWIA calculations using a well-tested spin-dependent component of the pion-nucleus inelastic interaction and spin transition densities obtained from fits to (e,e') data fail to reproduce both the shapes and magnitudes of the 3.563- and 15.11-MeV excitation functions, we suggest that the same mechanism may be responsible for the observed energy-dependent anomalous shapes in both ${}^6\text{Li}$ and ${}^{12}\text{C}$. A possible mechanism is the direct

-17-

excitation of Δ -h components of the excited state wave functions, as proposed in Ref. 10. Within this Δ -h model interpretation, we can estimate the amount of Δ -h admixture in the 3.563-MeV wave function. Using the peak of the 3.563-MeV excitation function ($T_{\pi} = 190$ MeV), the DWIA calculation which used the phenomenological spin transition density, and the procedure of Refs. 10 and 39, we estimate a mixing matrix element of $3 < \kappa < 37$ MeV. This range of values of κ is similar to that estimated for the 15.11-MeV state of ^{12}C ($7.4 < \kappa < 27.3$ MeV).³⁹ However, if the direct excitation of Δ -h components is applicable to both transitions, comparison of the two excitation functions and DWIA calculations (see Figs. 10 and 11) indicates that the resonant Δ -h scattering amplitude may interfere differently with the p-h scattering amplitude for the two transitions.

VI. CONCLUSIONS

Describing pion-nucleus inelastic scattering with the Born approximation and DWIA, we obtain predictions which agree with the π^+ -inelastic-scattering measurements for the 3^+ , 2.185-MeV and 2^+ , 4.25-MeV states of ^6Li . Our predictions fail to reproduce both the 120- and 180-MeV angular distributions and the excitation function for the unnatural-parity transition to the 3.563-MeV state. The measured excitation function exhibits an anomalous energy-dependent shape similar to that observed for the 1^+ , 15.11-MeV state of ^{12}C . Similar mechanisms may be responsible for the anomalous excitation functions for these isovector transitions. If this mechanism is the direct excitation of Δ -h components in the final state wave functions, the peak of the 3.563-MeV excitation function is reproduced with an estimated mixing matrix element of $3 < \kappa < 37$ MeV, a range of values consistent with the estimated

-18-

mixing matrix element of $7.4 < \kappa < 27.3$ MeV³⁹ for the 15.11-MeV excitation function.

VII. ACKNOWLEDGEMENTS

The authors thank F. Petrovich and J. A. Carr for their assistance in incorporation of the spin-dependent component of the pion-nucleon interaction into the computer code UTDWPI. This work was supported in part by the U. S. Department of Energy, the Robert A. Welch Foundation, and the Natural Sciences and Engineering Research Council of Canada.

-19-

REFERENCES

- a) present address: Intel, Rio Rancho, NM 87124
 - b) present address: University of New Mexico, Albuquerque, NM 87131
 - c) present address: Kirtland Air Force Base, Albuquerque, NM 87117
 - d) present address: Los Alamos National Laboratory, Los Alamos, NM 87545
 - e) present address: International Center for Theoretical Physics, Miramare, Trieste, Italy
- ¹ T. -S. H. Lee and D. Kurath, Phys. Rev. C 21, 293 (1980).
 - ² T. -S. H. Lee and R. D. Lawson, Phys. Rev. C 21, 679 (1980).
 - ³ Christopher L. Morris, Kenneth G. Boyer, C. Fred Moore, Carol J. Harvey, K. J. Kallianpur, Ingrid B. Moore, Peter A. Seidl, Susan J. Seestrom-Morris, D. B. Holtkamp, Steven J. Greene, and William B. Cottingham, Phys. Rev. C 24, 231 (1981).
 - ⁴ Kenneth G. Boyer, William B. Cottingham, L. E. Smith, Steven J. Greene, C. Fred Moore, J. S. McCarthy, R. C. Minehart, J. F. Davis, G. R. Burleson, G. Blanpied, Chuck A. Goulding, Henry A. Thiessen, and Christopher L. Morris, Phys. Rev. C 24, 598 (1981).
 - ⁵ W. B. Cottingham, K. Albright, S. Greene, C. Harvey, D. B. Holtkamp, R. J. Joseph, I. B. Moore, C. F. Moore, J. Piffaretti, C. L. Morris, N. King, R. L. Boudrie, J. Kraushaar, R. J. Peterson, B. Ristinen, and G. R. Smith, Bull. Am. Phys. Soc. 24, 821 (1979).
 - ⁶ S. J. Seestrom-Morris, D. Dehnhard, D. B. Holtkamp, and C. L. Morris, Phys. Rev. Lett. 46, 1447 (1981).
 - ⁷ E. R. Siciliano and G. E. Walker, Phys. Rev. C 23, 2661 (1981).
 - ⁸ M. K. Gupta and G. E. Walker, Nucl. Phys. A256, 444 (1976).

-20-

- 9 J. A. Carr, F. Petrovich, D. Halderson, D. B. Holtkamp, and W. B. Cottingame, Phys. Rev. C 27, 1636 (1983).
- 10 C. L. Morris, W. B. Cottingame, S. J. Greene, C. J. Harvey, C. Fred Moore, D. B. Holtkamp, S. J. Seestrom-Morris, and H. T. Fortune, Phys. Lett. 108B, 172 (1982).
- 11 S. Cohen and D. Kurath, Nuc. Phys. 73, 1 (1965), as quoted in T. -S. H. Lee and D. Kurath, Phys. Rev. C 21, 293 (1980).
- 12 W. B. Cottingame, K. G. Boyer, W. J. Braithwaite, S. J. Greene, C. J. Harvey, R. J. Joseph, D. B. Holtkamp, C. Fred Moore, J. J. Kraushaar, R. J. Peterson, R. A. Ristinen, R. L. Boudrie, N. S. P. King, C. L. Morris, J. Piffaretti, and H. A. Thiessen, submitted to Phys. Rev. C.
- 13 T. W. Donnelly and J. D. Walecka, Phys. Lett. 44B, 330 (1973).
- 14 J. C. Bergstrom, U. Deutschmann, and R. Neuhausen, Nuc. Phys. A327, 439 (1979).
- 15 H. A. Thiessen and S. Sobottka, Los Alamos Scientific Laboratory Report No. LA-4534 MS, (1970).
- 16 D. F. Geesaman, D. Kurath, G. C. Morrison, C. Olmer, B. Zeidman, R. E. Anderson, R. L. Boudrie, H. A. Thiessen, G. S. Blanpied, G. R. Burleson, R. E. Segel, and L. W. Swenson, Phys. Rev. C 27, 1134 (1983).
- 17 Lester Eugene Smith, computer program LOAF, Physics Department, University of Texas at Austin, Austin, Texas 78712, (1978).
- 18 F. Ajzenberg-Selove, Nuc. Phys. A413, 28 (1984).
- 19 F. Eigenbrod, Z. Phys. 228, 337 (1969).
- 20 Th. Delbar, Ch. Grégoire, and G. Paic, Phys. Rev. C 27, 1887 (1983).
- 21 G. R. Burleson and J. F. Amann, computer program CROSS (unpublished).
- 22 C. Rowe, M. Salomon, and R. H. Landau, Phys. Rev. C 18, 584 (1978).

-21-

- 23 W. B. Cottingham and D. B. Holtkamp, Phys. Rev. Lett. 45, 1828 (1980).
- 24 R. A. Eisenstein and G. A. Miller, Comput. Phys. Commun. 8, 130 (1974).
- 25 L. S. Kisslinger, Phys. Rev. 98, 761 (1955).
- 26 G. C. Li, I. Sick, R. R. Whitney, and M. R. Yearian, Nuc. Phys. A162, 583 (1971).
- 27 Janos A. Zichy, "Inelastic Scattering of π^+ and π^- in the Energy Region of the (3,3) Resonance," ETH-6612, Ph. D. Dissertation, (1980).
- 28 J. A. Carr, F. Petrovich, D. Halderson, and J. Kelly, to be published (1984).
- 29 K. G. Boyer, W. B. Cottingham, and D. B. Holtkamp, distorted wave code UTDWPI (unpublished), adapted from the code DWPI by R. A. Eisenstein and G. A. Miller, Comp. Phys. Commun. 11, 95 (1976).
- 30 R. Neuhausen and R. M. Hutcheon, Nuc. Phys. A164, 497 (1971).
- 31 F. Petrovich and W. G. Love, Nuc. Phys. A354, 499c (1981).
- 32 F. Petrovich, R. H. Howell, C. H. Poppe, S. M. Austin, and G. M. Crawley, Nuc. Phys. A383, 355 (1982).
- 33 J. A. Carr, private communication.
- 34 J. C. Bergstrom and E. L. Tomusiak, Nuc. Phys. A262, 196 (1976).
- 35 M. Bernheim and G. R. Bishop, Phys. Lett. 5, 270 (1963).
- 36 J. C. Bergstrom, S. B. Kowalski, R. Neuhausen, Phys. Rev. C 25, 1156 (1982).
- 37 J. C. Bergstrom, I. P. Auer, and R. S. Hicks, Nuc. Phys. A251, 401 (1975).
- 38 J. B. Cammarata and T. W. Donnelly, Nuc. Phys. A267, 365 (1976).
- 39 C. L. Morris, in Spin Excitations in Nuclei, Ed. by Petrovich, Brown, Garvey, Goodman, Lindgren, and Love, pp. 161,ff (Plenum Publishing Corporation, 1984).

-22-

TABLE I: Differential cross sections for π^+ elastic scattering and inelastic scattering to the 3^+ , 2.185-MeV, 0^+ , 3.563-MeV, and 2^+ , 4.25-MeV levels of ${}^6\text{Li}$.

T_π (MeV)	$\theta_{\text{c.m.}}$ (deg)	q^a (fm $^{-1}$)	Elastic	3^+ , 2.185 MeV	0^+ , 3.563 MeV	2^+ , 4.25 MeV
			$d\sigma/d\Omega_{\text{c.m.}}$ (mb/sr)	$d\sigma/d\Omega_{\text{c.m.}}$ (mb/sr)	$d\sigma/d\Omega_{\text{c.m.}}$ ($\mu\text{b/sr}$)	$d\sigma/d\Omega_{\text{c.m.}}$ (mb/sr)
100	34.3	0.55	27.2 \pm 0.1	0.397 \pm 0.017	39.8 \pm 2.2	0.147 \pm 0.005
120	15.7	0.29	80.5 \pm 0.4	0.271 \pm 0.033	33.9 \pm 3.0	0.079 \pm 0.005
120	21.9	0.40	74.1 \pm 0.4	0.307 \pm 0.042	43.6 \pm 4.6	0.091 \pm 0.008
120	25.1	0.46	64.0 \pm 0.3	0.569 \pm 0.032	61.5 \pm 5.6	0.137 \pm 0.009
120	28.2	0.51	49.1 \pm 0.2	0.632 \pm 0.033	41.3 \pm 4.7	0.259 \pm 0.014
120	28.2	0.51	48.8 \pm 0.2	0.587 \pm 0.030	48.4 \pm 4.1	0.203 \pm 0.008
120	30.3	0.55	43.0 \pm 0.3	0.737 \pm 0.040	57.0 \pm 4.3	0.276 \pm 0.009
120	33.4	0.61	34.9 \pm 0.2	0.799 \pm 0.030
120	33.4	0.61	35.1 \pm 0.2	0.853 \pm 0.037	38.0 \pm 3.3	0.274 \pm 0.007
120	38.6	0.69	32.8 \pm 3.2	0.395 \pm 0.007
120	43.7	0.79	15.0 \pm 0.1	0.973 \pm 0.029	22.3 \pm 3.2	0.335 \pm 0.007
120	48.9	0.87	8.2 \pm 0.1	0.975 \pm 0.028	12.3 \pm 2.3	0.274 \pm 0.005
140	27.2	0.55	64.9 \pm 0.3	1.11 \pm 0.05	60.7 \pm 4.4	0.315 \pm 0.009
160	25.2	0.55	80.5 \pm 0.3	1.36 \pm 0.06	68.5 \pm 5.5	0.505 \pm 0.011
170	24.7	0.57	70.2 \pm 7.0	0.607 \pm 0.011
170	24.7	0.57	85.4 \pm 0.5	1.78 \pm 0.09	80.7 \pm 9.4	0.637 \pm 0.021
180	21.1	0.50	103.4 \pm 0.4	1.25 \pm 0.07	117.0 \pm 7.6	0.855 \pm 0.018
180	24.3	0.58	79.4 \pm 0.3	1.74 \pm 0.06	100.0 \pm 7.7	0.690 \pm 0.015
180	24.3	0.58	79.5 \pm 0.5	1.62 \pm 0.08	95.0 \pm 9.4	0.801 \pm 0.021
180	24.3	0.58	79.3 \pm 0.4	1.59 \pm 0.06
180	24.3	0.58	80.9 \pm 0.5	1.68 \pm 0.09	62.0 \pm 9.1	0.763 \pm 0.019
180	27.4	0.65	61.3 \pm 0.3	1.97 \pm 0.06	55.0 \pm 5.6	0.829 \pm 0.012
180	30.6	0.72	44.7 \pm 0.2	2.32 \pm 0.06	43.1 \pm 6.3	0.883 \pm 0.014
190	23.2	0.57	97.0 \pm 12.0	0.870 \pm 0.030
190	23.2	0.57	89.5 \pm 9.5	0.981 \pm 0.030
200	21.7	0.56	81.7 \pm 6.4	0.607 \pm 0.013
200	21.7	0.56	100.7 \pm 0.7	1.96 \pm 0.12	97.0 \pm 5.7	0.737 \pm 0.012
215	20.7	0.56	107.0 \pm 0.5	1.88 \pm 0.09	73.3 \pm 5.6	0.892 \pm 0.012
230	19.7	0.55	105.7 \pm 0.7	2.03 \pm 0.12	55.9 \pm 7.3	0.707 \pm 0.015
230	19.7	0.55	103.4 \pm 1.5	2.09 \pm 0.25	55.6 \pm 6.0	0.703 \pm 0.013
260	18.2	0.56	109.8 \pm 0.8	2.06 \pm 0.13	33.1 \pm 10.5	0.713 \pm 0.021

^aThe q values were calculated for an excitation energy of 2.185 MeV.

-23-

FIGURE CAPTIONS

- Fig. 1. A typical π^+ energy-loss spectrum taken at $T_\pi = 140$ MeV and $\theta_{\text{LAB}} = 26^\circ$ for which the hardware veto of elastic events was used. The insert is the π^+ energy-loss spectrum without the use of the hardware veto.
- Fig. 2. Differential cross sections for π^+ and π^- elastic scattering for ${}^6\text{Li}$ for $T_\pi = 120, 164$, and 180 MeV. The calculations include a -30 MeV shift in the energy at which the optical model parameters are calculated. The 164-MeV data are from Ref. 27.
- Fig. 3. $F_L^2(q)$ for the 3^+ , $T=0$, 2.185-MeV state of ${}^6\text{Li}$. The calculations used microscopic transition densities derived from pure LS-coupling (solid curve) and Cohen-Kurath intermediate coupling (dashed curve) p-shell wave functions with $\alpha = 0.534 \text{ fm}^{-1}$ and a renormalization constant of 2.03 and $\alpha = 0.558 \text{ fm}^{-1}$ and a renormalization constant of 1.93, respectively. The data are from Refs. 14 (solid circles) and 34 (open circles).
- Fig. 4. Angular distributions for π^+ inelastic scattering to the 3^+ , $T=0$, 2.185-MeV state of ${}^6\text{Li}$ for $T_\pi = 120$ and 180 MeV. The calculations used microscopic transition densities derived from pure LS-coupling (solid curve) and Cohen-Kurath intermediate coupling (dashed curve) p-shell wave functions with $\alpha = 0.534 \text{ fm}^{-1}$ and a renormalization constant of 2.03 and $\alpha = 0.558 \text{ fm}^{-1}$ and a renormalization constant of 1.93, respectively.
- Fig. 5. Differential cross sections for π^+ inelastic scattering to the 3^+ , $T=0$, 2.185-MeV state of ${}^6\text{Li}$ at a constant $q = 109 \text{ MeV/c}$. The calculations used microscopic transition densities derived from pure LS-coupling (solid curve) and Cohen-Kurath intermediate coupling (dashed curve) p-shell wave functions with $\alpha = 0.534 \text{ fm}^{-1}$ and a

-24-

renormalization constant of 2.03 and $\alpha = 0.558 \text{ fm}^{-1}$ and a renormalization constant of 1.93, respectively.

Fig. 6. Angular distributions for π^+ inelastic scattering to the 2^+ , $T=0$, 4.25-MeV state of ${}^6\text{Li}$ for $T_\pi = 120$ and 180 MeV. The calculation used a microscopic transition density derived from Cohen-Kurath intermediate coupling p-shell wave functions with $\alpha = 0.52 \text{ fm}^{-1}$ and a renormalization constant of 0.82.

Fig. 7. Differential cross sections for π^+ inelastic scattering to the 2^+ , $T=0$, 4.25-MeV state of ${}^6\text{Li}$ at $q = 109 \text{ MeV}/c$. The calculation used a microscopic transition density derived from Cohen-Kurath intermediate coupling p-shell wave functions with $\alpha = 0.52 \text{ fm}^{-1}$ and a renormalization constant of 0.82.

Fig. 8. $F_T^2(q)$ for the 0^+ , $T=1$, 3.563-MeV state of ${}^6\text{Li}$. The calculations used a microscopic transition density derived from Cohen-Kurath intermediate coupling p-shell wave functions (solid curve) with $\alpha = 0.518 \text{ fm}^{-1}$ and a renormalization constant of 0.97, a microscopic transition density derived from the empirical shell-model wave functions of Donnelly and Walecka (dashed curve) with $\alpha = 0.493 \text{ fm}^{-1}$ and a renormalization constant of 0.96, and a phenomenological transition density based on the work of Bergstrom, *et al.* (chain-dot curve). The data are from Refs. 14 (solid circles) and 37 (open circles).

Fig. 9. Angular distributions for π^+ inelastic scattering to the 0^+ , $T=1$, 3.563-MeV state of ${}^6\text{Li}$ for $T_\pi = 120$ and 180 MeV. The calculations used a microscopic transition density derived from Cohen-Kurath intermediate coupling p-shell wave functions (solid curve) with $\alpha = 0.518 \text{ fm}^{-1}$ and a renormalization constant of 0.97, a microscopic transition density derived from the empirical shell-model wave

-25-

functions of Donnelly and Walecka (dashed curve) with $\alpha = 0.493 \text{ fm}^{-1}$ and a renormalization constant of 0.96, and a phenomenological transition density based on the work of Bergstrom, et al. (chain-dot curve).

Fig. 10. Excitation function at a constant $q = 109 \text{ MeV/c}$ for π^+ inelastic scattering to the 0^+ , $T=1$, 3.563-MeV state of ${}^6\text{Li}$. The calculations used a microscopic transition density derived from Cohen-Kurath intermediate coupling p-shell wave functions (solid curve) with $\alpha = 0.518 \text{ fm}^{-1}$ and a renormalization constant of 0.97, a microscopic transition density derived from the empirical shell-model wave functions of Donnelly and Walecka (dashed curve) with $\alpha = 0.493 \text{ fm}^{-1}$ and a renormalization constant of 0.96, and a phenomenological transition density based on the work of Bergstrom, et al. (chain-dot curve).

Fig. 11. Excitation functions (averaged π^+ and π^- cross sections to remove isospin mixing) at a constant $q = 124 \text{ MeV/c}$ for pion inelastic scattering to the 1^+ , $T=0$, 12.71-MeV (circles) and 1^+ , $T=1$, 15.11-MeV (squares) states of ${}^{12}\text{C}$. The calculations used microscopic transition densities derived from Cohen-Kurath p-shell wave functions. The solid curve is for the 12.71-MeV state. The dashed curve is for the 15.11-MeV state and has been multiplied by four (see Ref. 10).

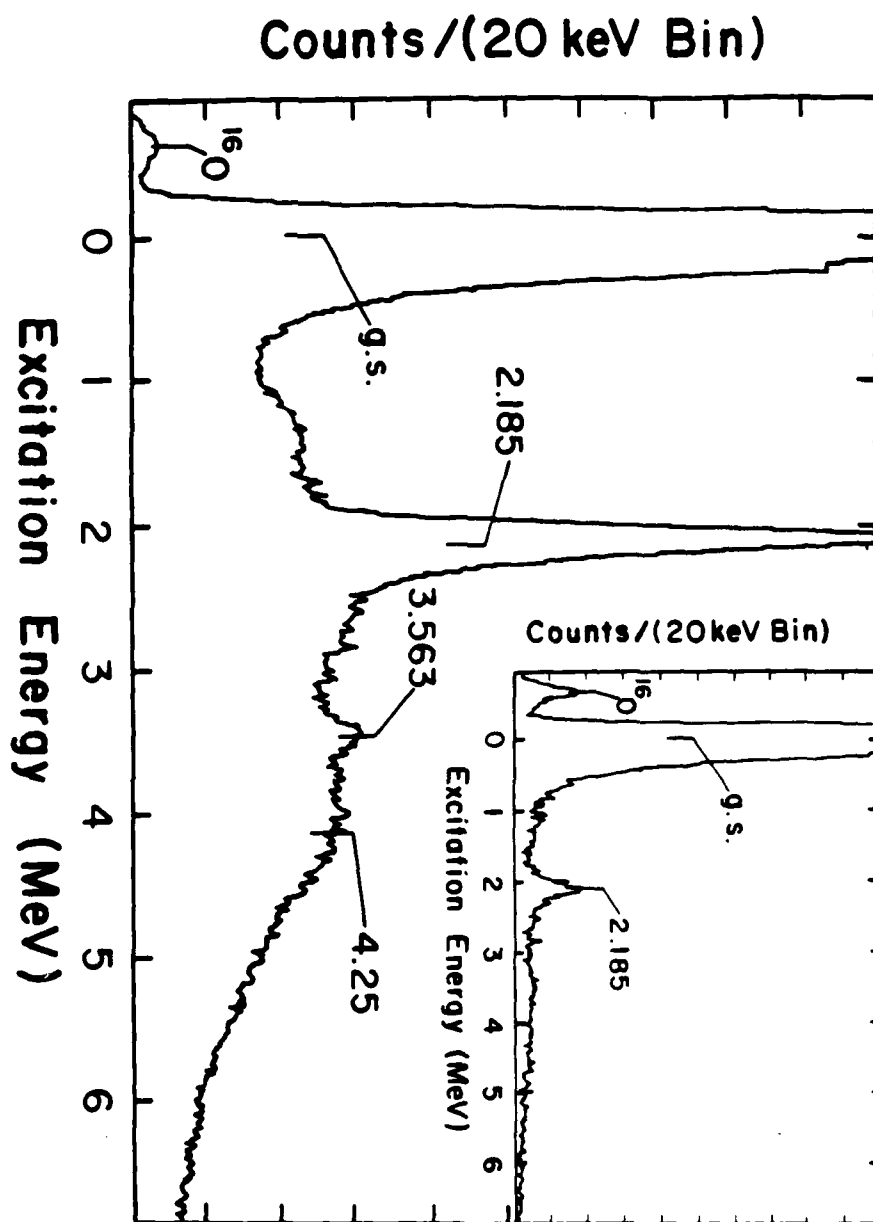


Fig. 1

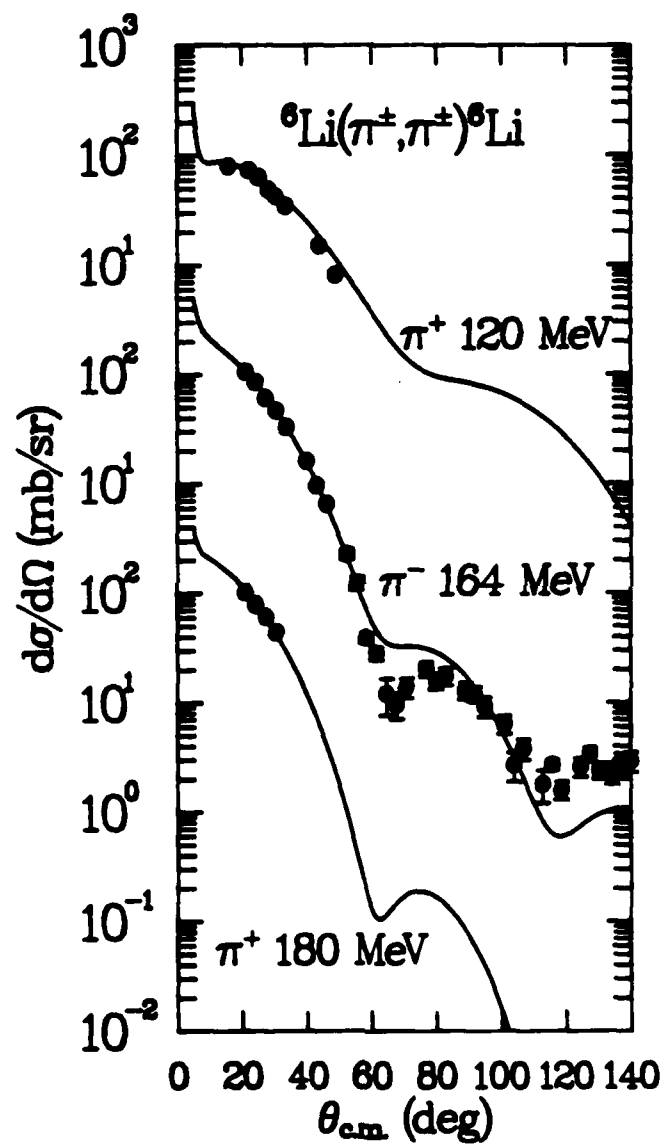


Fig. 2

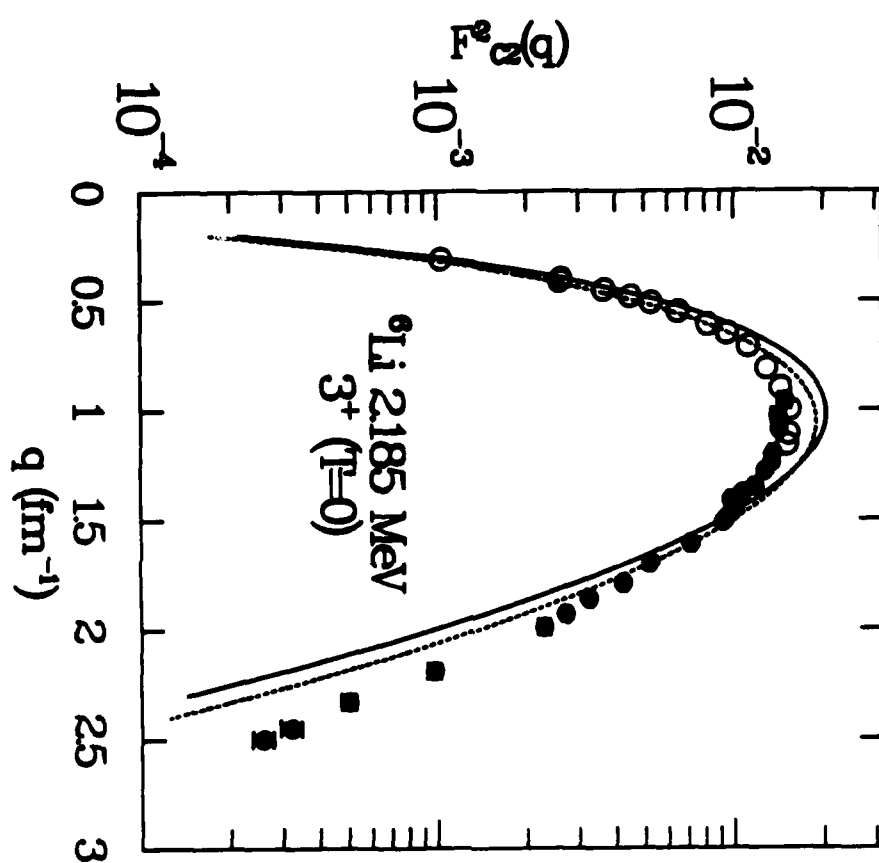


Fig. 3

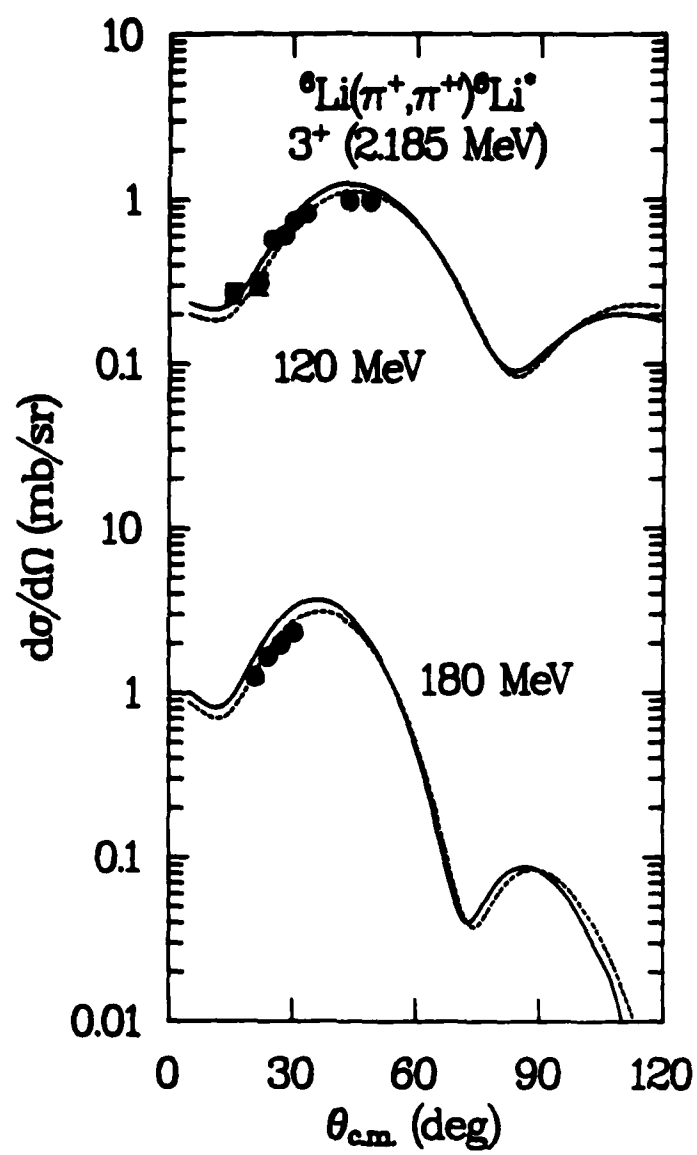


Fig. 4

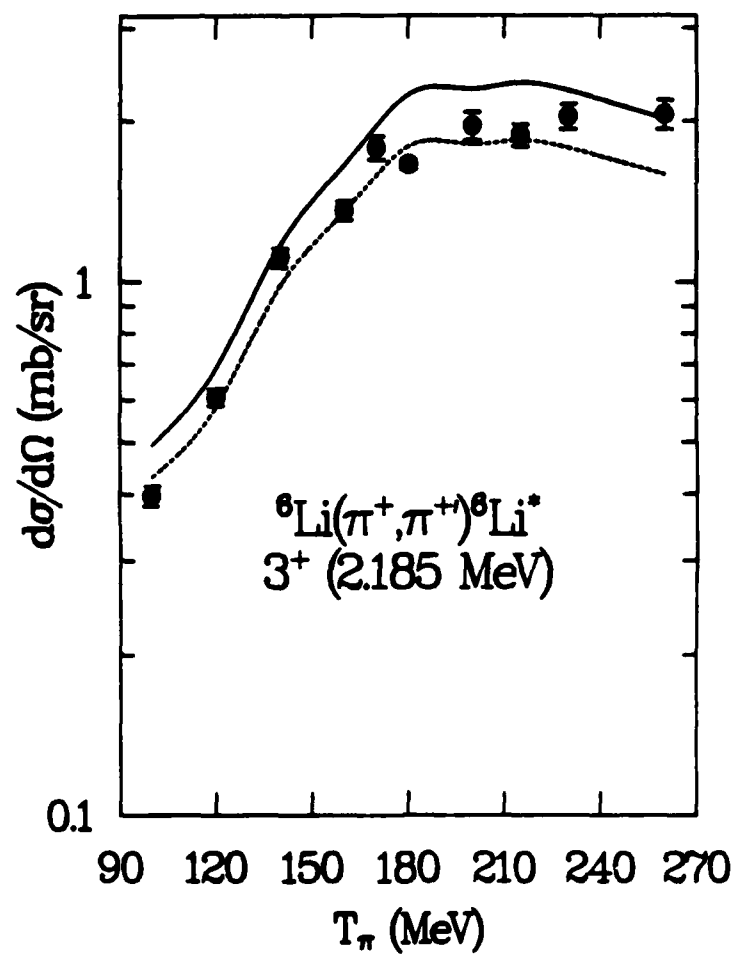


Fig. 5

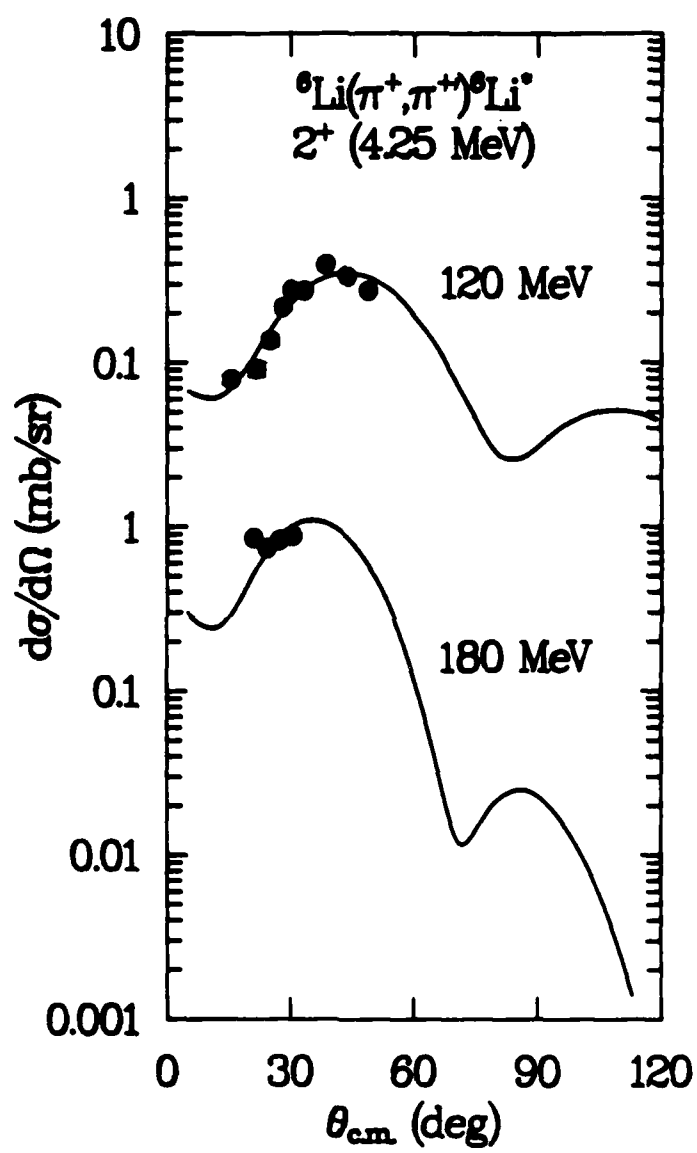


Fig. 6

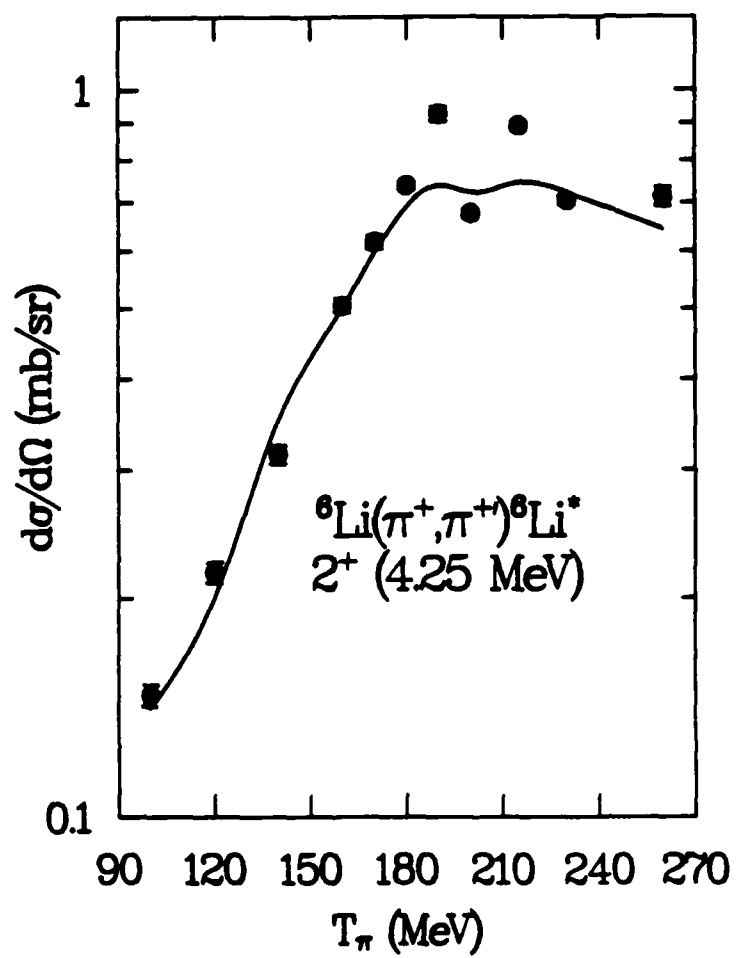


Fig. 7

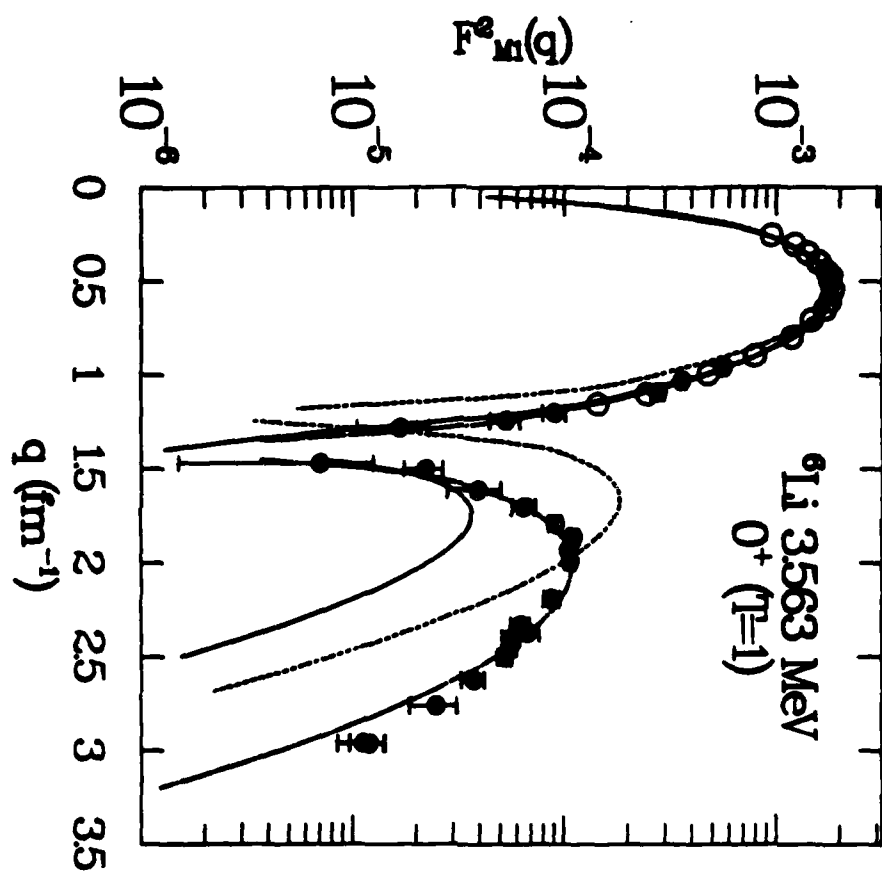


Fig. 8

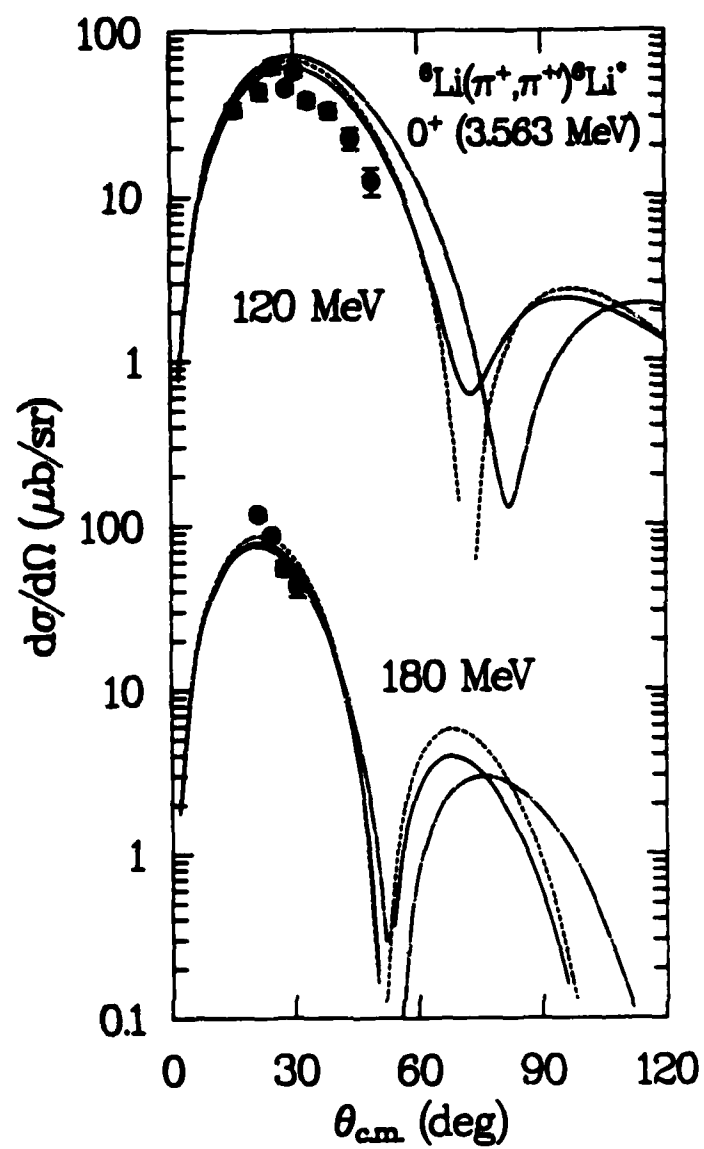


Fig. 9

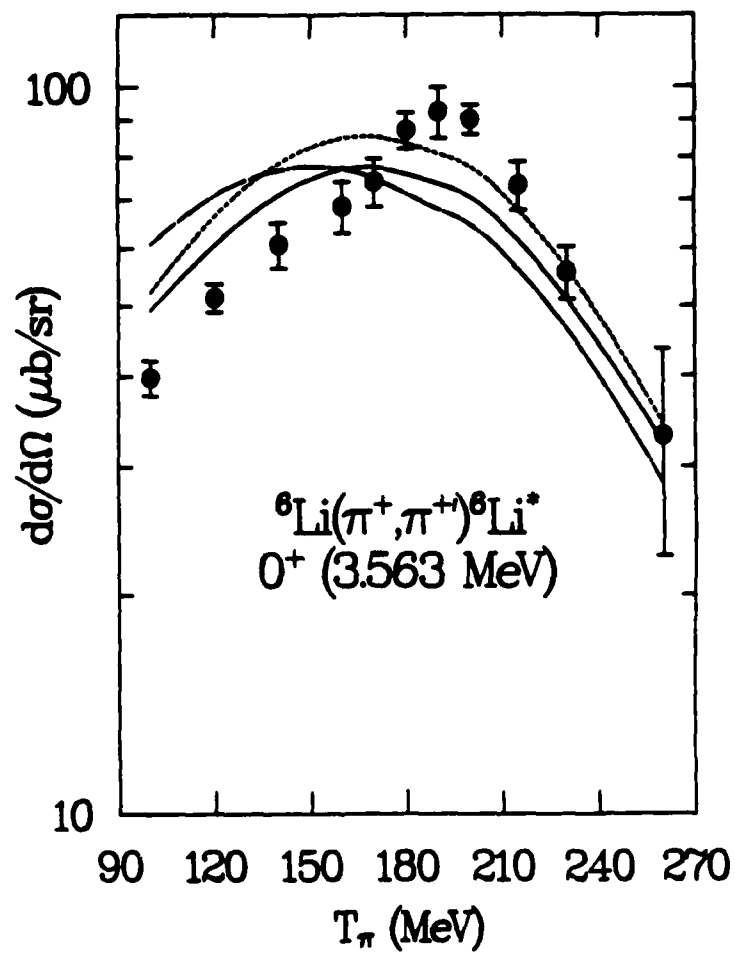


Fig. 10

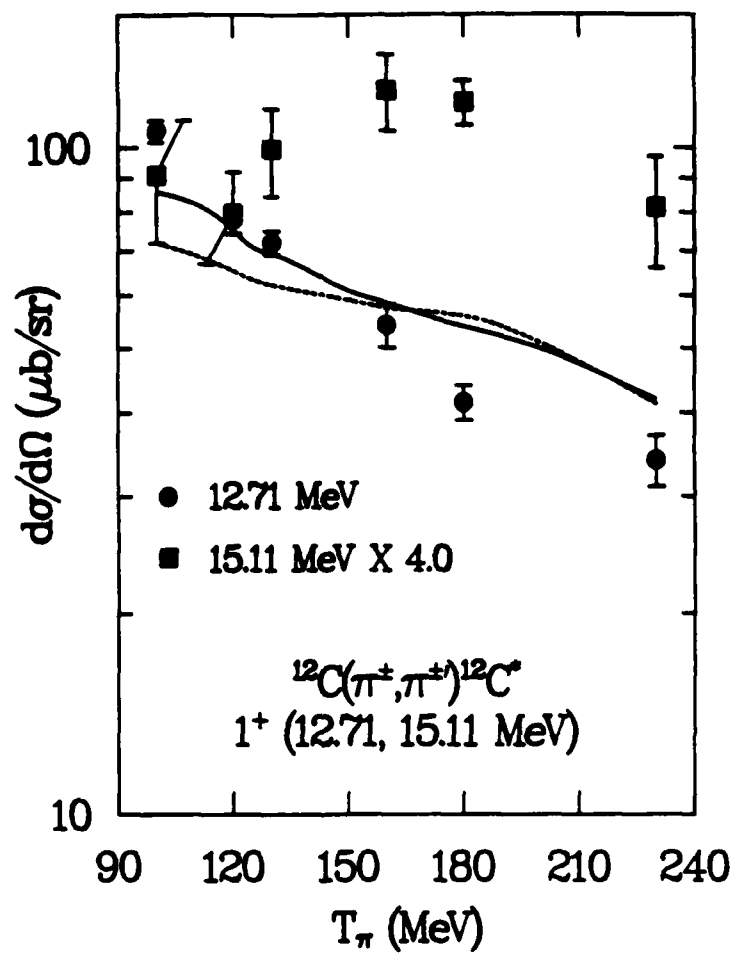


Fig. 11

REFERENCES

- [Aj-84] F. Ajzenberg-Selove, Nuc. Phys. A413, 28 (1984).
- [Al-77] John C. Allred, "LAMPF: The Meson Factory, A LASL Monograph," Los Alamos Scientific Laboratory Report LA-6878-MS, (1977).
- [Am-78] James F. Amann, "Alltst--A Data Testing Package," (1978).
- [Am-79] James F. Amann, Richard L. Boudrie, Henry A. Thiessen, Christopher L. Morris, and Lester E. Smith, IEEE Trans. Nucl. Sci. NS-26, 4389 (1979).
- [At-81] L. G. Atencio, J. F. Amann, R. L. Boudrie, and C. L. Morris, Nuc. Instr. Meth. 187, 381 (1981).
- [Be-63] M. Bernheim and G. R. Bishop, Phys. Lett. 5, 270 (1963).
- [Be-75] J. C. Bergstrom, I. P. Auer, and R. S. Hicks, Nuc. Phys. A251, 401 (1975).
- [Be-76] J. C. Bergstrom and E. L. Tomusiak, Nuc. Phys. A262, 196 (1976).
- [Be-79] J. C. Bergstrom, U. Deutschmann, and R. Neuhausen, Nuc. Phys. A327, 439 (1979).
- [Be-82] J. C. Bergstrom, S. B. Kowalski, R. Neuhausen, Phys. Rev. C 25, 1156 (1982).
- [Bl-66] J. S. Blair, in Lectures in Theoretical Physics, Ed. by P. D. Kunz, D. A. Lind, and W. E. Brittin, pp. 343,ff (University of Colorado Press, Boulder, 1966).
- [Bl-84] L. C. Bland, "Forward-Angle Pion Inelastic Scattering," Los Alamos National Laboratory Report LA-9960-T, (1984).

- [Bo-79] Richard L. Boudrie, James F. Amann, Christopher L. Morris, Henry A. Thiessen, and Lester E. Smith, IEEE Trans. Nucl. Sci. NS-26, 4588 (1979).
- [Bo-81] Kenneth G. Boyer, William B. Cottingame, L. E. Smith, Steven J. Greene, C. Fred Moore, J. S. McCarthy, R. C. Minehart, J. F. Davis, G. R. Burleson, G. Blanpied, Chuck A. Goulding, Henry A. Thiessen, and Christopher L. Morris, Phys. Rev. C 24, 598 (1981).
- [Bo-84] K. G. Boyer, "Pion Elastic and Inelastic Scattering from $^{40,42,44,48}\text{Ca}$ and ^{54}Fe ," Los Alamos National Laboratory Report LA-9974-T, (1984).
- [Bo-n.d.] K. G. Boyer, W. B. Cottingame, and D. B. Holtkamp, distorted wave code UTDWPI (unpublished), n.d., adapted from the code DWPI by R. A. Eisenstein and G. A. Miller, Compt. Phys. Commun. 11, 95 (1976).
- [Br-72] K. H. Bray, Mahavir Jain, K. S. Jayaraman, G. Lobianco, G. A. Moss, W. T. H. Van Oers, D. O. Wells, and F. Petrovich, Nuc. Phys. A189, 35 (1972).
- [Bu-n.d.] G. R. Burleson and J. F. Amann, computer program CROSS (unpublished), n.d.
- [Ca-76] J. B. Cammarata and T. W. Donnelly, Nuc. Phys. A267, 365 (1976).
- [Ca-83] J. A. Carr, F. Petrovich, D. Halderson, D. B. Holtkamp, and W. B. Cottingame, Phys. Rev. C 27, 1636 (1983).

- [Ca-84] J. A. Carr, F. Petrovich, D. Halderson, and J. Kelly, to be published (1984).
- [Ca-84a] J. A. Carr, private communication, (1984).
- [Co-65] S. Cohen and D. Kurath, Nuc. Phys. 73, 1 (1965), as quoted in T. -S. H. Lee and D. Kurath, Phys. Rev. C 21, 293 (1980).
- [Co-79] W. B. Cottingham, K. Allbright, S. Greene, C. Harvey, D. B. Holtkamp, R. J. Joseph, I. B. Moore, C. F. Moore, J. Piffaretti, C. L. Morris, N. King, R. L. Boudrie, J. Kraushaar, R. J. Peterson, B. Ristinen, and G. R. Smith, Bull. Am. Phys. Soc. 24, 821 (1979).
- [Co-80] W. B. Cottingham and D. B. Holtkamp, Phys. Rev. Lett. 45, 1828 (1980).
- [Co-84] W. B. Cottingham, K. G. Boyer, W. J. Braithwaite, S. J. Greene, C. J. Harvey, R. J. Joseph, D. B. Holtkamp, C. Fred Moore, J. J. Kraushaar, R. J. Peterson, R. A. Ristinen, R. L. Boudrie, N. S. P. King, C. L. Morris, J. Piffaretti, and H. A. Thiessen, submitted to Phys. Rev. C.
- [De-83] Th. Delbar, Gh. Grégoire, and G. Pačić, Phys. Rev. C 27, 1887 (1983).
- [Do-73] T. W. Donnelly and J. D. Walecka, Phys. Lett. 44B, 330 (1973).
- [Ei-69] F. Eigenbrod, Z. Phys. 228, 337 (1969).
- [Ei-74] R. A. Eisenstein and G. A. Miller, Comput. Phys. Commun. 8, 130 (1974).

- [Ei-80] J. Eisenberg and D. Koltun, Theory of Meson Interactions with Nuclei, (John Wiley and Sons, New York, 1980).
- [El-61] L. R. B. Elton, Nuclear Sizes, (Oxford University Press, London), Chapt. 2, 4-57 (1961).
- [Er-80] D. J. Ernst and Gerald A. Miller, Phys. Rev. C 21, 1472 (1980).
- [Fr-53] Norman C. Francis and Kenneth M. Watson, Am. J. Phys. 21, 659 (1953).
- [Fr-56] R. M. Frank, J. L. Gammel, and K. M. Watson, Phys. Rev. 101, 891 (1956).
- [Ge-83] D. F. Geesaman, D. Kurath, G. C. Morrison, C. Olmer, B. Zeidman, R. E. Anderson, R. L. Boudrie, H. A. Thiessen, G. S. Blanpied, G. R. Burleson, R. E. Segel, and L. W. Swenson, Phys. Rev. C 27, 1134 (1983).
- [Gu-76] M. K. Gupta and G. E. Walker, Nuc. Phys. A256, 444 (1976).
- [Ho-80] D. B. Holtkamp, "Elastic and Inelastic Scattering of Pions from Oxygen-16," Los Alamos Scientific Laboratory Report LA-8231-T, (1980).
- [Iv-79] S. G. Iversen, "Neutron-Proton Radius Differences and Isovector Deformations from π^+ and π^- Inelastic Scattering from ^{18}O ," Los Alamos Scientific Laboratory Report LA-7828-T, (1979).
- [Ja-75] John D. Jackson, Classical Electrodynamics, (John Wiley and Sons, New York), Chapt. 13, 618-653 (1975).
- [Ja-75a] F. James and M. Roos, Comput. Phys. Commun. 10, 343 (1975).

- [Ke-78] Martin Kellogg, Michael M. Minor, Sally Schlaer, Nancy Spencer, Richard F. Thomas, Jr., and Henri van der Beken, "Introduction to Q," Los Alamos Scientific Laboratory Report LA-7001-M, (1978).
- [Ki-55] L. S. Kisslinger, Phys. Rev. 98, 761 (1955).
- [La-73] R. H. Landau, S. C. Phatak, and F. Tabakin, Ann. Phys. 78, 299 (1973).
- [LA-80] LAMPF Users Handbook, Los Alamos Scientific Laboratory, MP-DO-1-UHB (Rev.), (1980).
- [Le-74] Tsung-Shung H. Lee and Frank Tabakin, Nuc. Phys. A226, 253 (1974).
- [Le-80] T. -S. H. Lee and D. Kurath, Phys. Rev C 21, 293 (1980).
- [Le-80a] T. -S. H. Lee and R. D. Lawson, Phys. Rev. C 21, 679 (1980).
- [Li-71] G. C. Li, I. Sick, R. R. Whitney, and M. R. Yearian, Nuc. Phys. A162, 583 (1971).
- [Li-72] M. Stanley Livingston, "Origins and History of the Los Alamos Meson Physics Facility," Los Alamos Scientific Laboratory Report LA-5000, (1972).
- [Li-77] M. Stanley Livingston, "LAMPF, A Nuclear Research Facility," Los Alamos Scientific Laboratory Report LA-6878-MS, (1977).
- [Me-66] Adrian C. Melissinos, Experiments in Modern Physics, (Academic Press, New York), Chapt. 5, 150-225 (1966).
- [Mo-74] P. J. Moffa and G. E. Walker, Nuc. Phys. A222, 140 (1974).
- [Mo-81] Christopher L. Morris, Kenneth G. Boyer, C. Fred Moore, Carol J. Harvey, K. J. Kallianpur, Ingrid B. Moore, Peter A. Seidl,

- Susan J. Seestrom-Morris, D. B. Holtkamp, Steven J. Greene, and William B. Cottingame, Phys. Rev. C 24, 231 (1981).
- [Mo-82] C. L. Morris, W. B. Cottingame, S. J. Greene, C. J. Harvey, C. Fred Moore, D. B. Holtkamp, S. J. Seestrom-Morris, and H. T. Fortune, Phys. Lett. 108B, 172 (1982).
- [Mo-82a] C. L. Morris, Nuc. Instr. Meth. 196, 263 (1982).
- [Mo-84] C. L. Morris, J. F. Amann, R. L. Boudrie, N. Tanaka, S. J. Seestrom-Morris, L. C. Bland, P. A. Seidl, and R. Kiziah, to be published (1984).
- [Mo-84a] C. L. Morris, in Spin Excitations in Nuclei, Ed. by Petrovich, Brown, Garvey, Goodman, Lindgren, and Love, pp. 161,ff (Plenum Publishing Corporation, 1984).
- [Ne-69] U. S. Neudatchim and Yu. I. Smirnoiv, in Progress in Nuclear Physics, Vol. 10, Ed. by D. M. Brink and J. H. Mulvey, pp. 273,ff (Pergamon, Oxford, 1969).
- [Ne-71] R. Neuhausen and R. M. Hutcheon, Nuc. Phys. A164, 497 (1971).
- [Pe-79] F. Petrovich and W. G. Love, Proc. LAMPF Workshop on Pion Single Charge Exchange, Los Alamos, 1979, Los Alamos Scientific Laboratory Report LA-7892-C, addendum.
- [Pe-81] F. Petrovich and W. G. Love, Nuc. Phys. A234, 499c (1981).
- [Pe-82] F. Petrovich, R. H. Howell, C. H. Poppe, S. M. Austin, and G. M. Crawley, Nuc. Phys. A383, 355 (1982).
- [Ro-78] C. Rowe, M. Salomon, and R. H. Landau, Phys. Rev. C 18, 584 (1978).

- [Sc-75] H. Schwartz and C. M. Fou, J. Phys. G. 7, 1975.
- [Se-81] S. J. Seestrom-Morris, D. Dehnhard, D. B. Holtkamp, and C. L. Morris, Phys. Rev. Lett. 46, 1447 (1981).
- [Se-81a] S. J. Seestrom-Morris, "The Structure of ^{13}C Studied by Pion Scattering Near the [3,3] Resonance," Los Alamos National Laboratory Report LA-8916-T, (1981).
- [Se-82] S. J. Seestrom-Morris, D. Dehnhard, M. A. Franey, G. S. Kyle, C. L. Morris, R. L. Boudrie, J. Piffaretti, and H. A. Thiessen, Phys. Rev. C 26, 594 (1982).
- [Si-81] E. R. Siciliano and G. E. Walker, Phys. Rev. C 23, 2661 (1981).
- [Sm-78] Lester Eugene Smith, computer program LOAF, Physics Department, University of Texas at Austin, Austin, Texas 78712, (1978).
- [St-74] M. M. Sternheim and R. R. Silbar, Ann. Rev. Nuc. Sci. 24, 249 (1974).
- [Ta-72] John R. Taylor, Scattering Theory: The Quantum Theory on Nonrelativistic Collisions, (John Wiley and Sons, New York, 1972).
- [Th-70] H. A. Thiessen and S. Sobottka, "A Proposal for EPICS: A High-Resolution Pion Beam and Spectrometer Facility for Nuclear Structure Research at LAMPF," Los Alamos Scientific Laboratory Report LA-4534-MS, (1970).
- [Th-77] H. A. Thiessen, J. C. Källne, J. F. Amann, R. J. Peterson, S. J. Greene, S. L. Verbeck, G. R. Burleson, S. G. Iversen, A. W. Obst, Kamal K. Seth, C. F. Moore, J. E. Bolger, W. J. Braithwaite, D. C. Slater, and C. L. Morris, "EPICS Pion

Channel Performance," Los Alamos Scientific Laboratory Report LA-6663-MS, (1977).

- [Wa-57] K. M. Watson, Phys. Rev. 105, 1388 (1957).
- [Wa-58] Kenneth M. Watson, Revs. Modern Phys. 30, 565 (1958).
- [Yu-35] H. Yukawa, Proceedings of the Mathematical Society of Japan 17, 48 (1935).
- [Zi-80] Janos A. Zichy, "Inelastic Scattering of π^+ and π^- in the Energy Region of the (3,3) Resonance," ETH-6612, Ph.D. thesis, (1980).

VITA

Rex Raymond Kiziah was born in Granite Falls, North Carolina, on July 17, 1959, the son of Ruth Daye Kiziah and Raymond Carroll Kiziah. After completing high school at Granite Falls High School, Granite Falls, North Carolina, in May 1977, he entered the United States Air Force Academy at Colorado Springs, Colorado. He received the degree of Bachelor of Science with a major in physics from the United States Air Force Academy in May 1981. In August 1981, he entered the Graduate School of The University of Texas at Austin. Since May 1981 he has served in the United States Air Force. In December 1981, he married Barbara Ann Cline of Granite Falls, North Carolina.

Permanent Address: 5600 Gibson, S.E. Apt # 323
Albuquerque, NM 87108

END

UNLIMED

DTIC